HAL
open science

Oxygen-excess related defects in SiO2-based materials : coupling theory and experiments

Blaz Winkler

To cite this version:

Blaz Winkler. Oxygen-excess related defects in SiO2-based materials : coupling theory and experiments. Optics [physics.optics]. Université de Lyon; Université de Nova Gorica (Nova Gorica, Slovénie), 2019. English. NNT : 2019LYSES014 . tel-03262513

HAL Id: tel-03262513

https://theses.hal.science/tel-03262513v1

Submitted on 16 Jun 2021

HAL is a multi-disciplinary open access archive for the deposit and dissemination of scientific research documents, whether they are published or not. The documents may come from teaching and research institutions in France or abroad, or from public or private research centers.

L'archive ouverte pluridisciplinaire **HAL**, est destinée au dépôt et à la diffusion de documents scientifiques de niveau recherche, publiés ou non, émanant des établissements d'enseignement et de recherche français ou étrangers, des laboratoires publics ou privés.

N°d'ordre NNT : 2019LYSES014

Cotutelle PhD thesis of THE UNIVERSITY OF LYON

in

Laboratory Hubert Curien

Doctoral school N° 488
Science, Engineering & Health

Physics / Optics, Photonics

and

UNIVERSITY OF NOVA GORICA
Graduate school

Public defense on May 7th 2019 by :

Blaž Winkler

OXYGEN-EXCESS RELATED DEFECTS IN SiO_2-BASED MATERIALS : COUPLING THEORY AND EXPERIMENTS

Jury composed by :

Ouerdane, Youcef	Professor University of Lyon	President
de Gironcoli, Stefano	Professor SISSA	Reviewer
Skuja, Linards	Professor University of Latvia	Reviewer
Kokalj, Anton	Professor Jožef Stefan Institute	Reviewer
Boukenter, Aziz	Professor University of Lyon	Examiner
Martin-Samos, Layla	Professor University of Nova Gorica	Supervisor
Girard, Sylvain	Professor University of Lyon	Co-supervisor
Richard, Nicolas	PhD CEA DAM	Invited

UNIVERZA V NOVI GORICI
FAKULTETA ZA PODIPLOMSKI ŠTUDIJ

Blaž Winkler, *Oxygen-excess related defects in SiO_2 -based materials : Coupling theory and experiments, 2019*

Copyright and moral rights for this work are retained by the author.
A copy can be downloaded for personal non-commercial research or study, without prior permission or charge.
This work cannot be reproduced or quoted extensively from without first obtaining permission in writing from the author.
The content must not be changed in any way or sold commercially in any format or medium without the formal permission of the author.
When referring to this work, full bibliographic details including the author, title, awarding institution and date of the thesis must be given.

Acknowledgment

This thesis would not be possible without the amazing support from both of my mentors, *Prof. Dr. Layla Martin-Samos* and *Prof. Dr. Sylvain Girard*. I would like to thank you both for guidance, encouragement and all the patience during research and writing of the thesis.

A number of great people have also contributed to this thesis in many ways and I would like to express my greatest gratitude to all of you : Luigi, Nicolas S., Nicolas R. and Chaitanya for fruitful discussions about many properties of solids, Andraž, Mojca, Katja and other amazing coworkers from MRL for all the help and encouragement, everybody from LaHC for hospitality with particular mentions of Imène, Adriana, Diego, Antonino, Aziz and Youcef for their valuable help during the experimental measurements. I would also like to thank my family for endless encouragement and support.

This research has been made possible with the financial support from Slovenian Research agency (postgraduate research funding, research programs P1-0112 and P1-0134). Super-computing resources have been provided by Cineca and CINES through multiple projects.

Last but not least I would like to thank the members of the committee, *Prof. Dr. Sylvain Girard, Prof. Dr. Aziz Boukenter, Prof. Dr. Youcef Ouerdane, Prof. Dr. Anton Kokalj, Prof. Dr. Stefano de Gironcoli* and *Prof. Dr. Linards Skuja*.

Abstract

This work is primarily focused on application of standard first-principle computational approaches to model oxygen excess related point defects in amorphous silica. Atomic models with their respective electronic and optical properties are explored together with some conversion mechanisms between defect models.

The first chapter overviews extensive literature about the already known properties of oxygen related defects. Second chapter briefly introduces main methods that have been used in this research, in particular Density Functional Theory (DFT) as energy and force engine with short description of minimal energy path (MEP) algorithm used for modeling chemical/migration reactions, GW approximation for charged electronic excitations (band structure) and Bethe-Salpeter Equation (BSE) for neutral excitations (optical absorption and excitonic structure including electron hole interaction).

The third chapter is devoted to the presentation of results. Thanks to the calculation of optical properties of peroxy bridge (POL), a correlation has been found between structural disorder, specifically dihedral angle dispersion, and low coupling with light, which has been identified as main reason why no clear absorption bands have been assigned to the POL. Structure and stability of some other defects, like interstitial ozone molecule (ozonyl) and dioxasilirane (silicon analogy of dioxirane), have been studied. These defects are usually not considered as most important species, however their calculated formation energies are lower compared to some known defects, which indicates they might be present in silica.

From a detailed study on possible reaction mechanisms, it has been found that ozonyl might be one of the most important intermediate steps for oxygen exchange reactions. Results also show that dioxasilirane can be spontaneously created during the interaction of oxygen with lone pair defects. By exploring different reactions between oxygen and pre-existing oxygen deficiency centers (ODCs), calculations predict two kinds of passivation behaviors : single-barrier reversible mechanisms with the formation of dioxasilirane-like groups, for which the network keeps the memory of the precursory lone pair defects, and single or multiple-barrier mechanisms, for which the network loses its memory, either because of the high reverse barrier or because of a reconstruction.

Final part of this research has been devoted to experimental characterization of the response and tolerance of optical fibers loaded with oxygen under irradiation. These include experiments on commercial fiber along with canonical samples (Optical fibers developed with the intention of studying correlations between different fabrication parameters, dopant/impurity concentration and doping concentrations). Studied fibers also include rare-earth doped fibers.

Keywords

Silica, DFT, GW-approximation, Bethe-Salpeter equation, NEB, defect, oxygen, oxygen excess centers, oxygen deficiency centers, optical absorption, optical fibers, radiation induced attenuation.

Povzetek

Večji del raziskav predstavjenih v disertacji opisuje uporabo standardnih teoretičnih pristopov z namenom modeliranja vplivov presežnega kisika na točkaste defekte v amorfnem silicijevem dioksidu (silika). Ti pristopi omogočajo modeliranje strukture na atomski ravni, elektronske in optične lastnosti ter dinamične pretvorne mehanizme med različnimi defekti.

Prvo poglavje je namenjeno pregledu obsežne literature na temo defektov povezanih s presežnim kisikom. V drugem poglavju sledi kratek opis najpomembnejših lastnosti metod uporabljenih v raziskavah: Teorija gostotnega funkcionala kot osnova za izračun energij in strukture sistemov in predstavitev algoritma za simulacijo najnižje energijske poti, katera omogoča opis kemičnih/migracijskih reakcij, GW približek za nabite elektronske vzbuditve (struktura elektronskih pasov in nezasedenih stanj) in Bethe-Sapleterjeva enačba za nevtralne vzbuditve (optična absorpcija in ekscitonska struktura, katera vključuje sklopitev med elektroni in elektronskimi vrzelmi)

Rezultati so predstavljeni v tretjem poglavju. Optična struktura peroksidnega defekta, izračunana z metodo GW približka, je pokazala na povezavo med strukturnim neredom (kateri vpliva na disperzijo dihdralnega kota) in majhno verjetnostjo optične sklopitve, kar je najverjetneje glavni razlog zakaj ta defekt ni bil nikoli neizpodbitno zaznan z eksperimenti. V nadaljevanju so predstavljene strukture nekaterih manj očitnih defektov kot so ozonil (molekula ozona ujeta v kristalno mrežo) in dioksasiliran (silicijeva analogija dioksirana). Izračunane energije potrebne za njihov nastanek so primerljive z energijami drugih že poznanih efektov, zaradi česar lahko predvidevamo, da so lahko tudi ti defekti prisotni v silicijevem dioksidu. Ozonil je še posebej zanimiv defekt, saj rezultati simulacij kemičnih reakcij kažejo njegovo ključno vlogo v procesih izmenjave kisika. V reakciji kisika z obstoječimi defekti, kateri vključujejo proste elektronske pare, se lahko spontano tvori dioksasiliran. Dva glavna načina nasičenja sta bila odkrita za reakcije kisika z obstoječimi vrzelmi: Povratni mehanizem s katerim se tvori dioksasiliran in v katerem kristalna struktura ohrani sledi predhodnega defekta ter drugi, kompleksnejši, večfazni način v katerem se lokalna struktura okrog defekta rekombinira in posledično zabriše sled izvirnega defekta (zaradi rekombinacije ali visoke energije potrebne za povratno reakcijo).

Zadnji del opisuje eksperimentalne raziskave vpliva presežnega kisika na optčna vlakna ter odziv tovrstnih vlaken na sevanje. Raziskave so bile opravljene tako na komercialnih vlaknih kot tudi na posebnih prototipnih vlaknih izdelanih z namenom preučevanja vplivov različnih koncentracij dopantov/nečistoč in proizvodnih parametrov. Nekatera preučevana vlakna so dopirana tudi z redkimi zemljami.

Ključne besede

Silicijev dioksid, DFT, GW-približek, Bethe-Salpeterjeva enačba, NEB, defekt, kisik, defekti presežnega kisika, defekti pomanjkanja kisika, optična absorpcija, optično vlakno, izgube povzročene s sevanjem

Résumé

Ce travail de thèse est principalement dédié à l'application de méthodes computationnelles ab-initio pour la modélisation des défauts ponctuels liés à l'excés d'oxygéne dans la silice amorphe. Différents modelés atomiques de défauts, leurs correspondantes propriétés électroniques et optiques ainsi que quelques mécanismes de conversions y sont présentés et discutés.

Le premier chapitre offre un résumé des travaux précédents sur les propriétés connues des défauts lies à l'excés d'oxygéne. Le deuxiéme chapitre introduit briévement les approches principales qui ont éété utilisées pour ce travail de recherche, en particulier, la Théorie de la Fonctionnelle Densité (DFT) ainsi que l'algorithme de recherche du chemin d'énergie minimale (MEP), l'Approximation GW qui permet d'obtenir les énergies dexcitation chargées (structure de bande) et l'Equation Bethe-Salpeter pour les excitations neutres (absorption optique et excitons en incluant l'interaction électron-trou). Le troisiéme chapitre est dédié à la présentation des résultats. Grace aux calculs de propriétés optiques des Pont Peroxy (POL), une corrélation a été trouvé entre le désordre structurel, concrétement l'angle dihedral, et le faible couplage avec la lumiére. Ce faible couplage est la raison principale qui empêche d'associer des bandes d'absorption optiques claires au POL. La structure et stabilité d'autres défauts comme la molécule interstitielle d'ozone et le dioxasilarene (l'analogue silicium du dioxirane) ont aussi été étudies. Ces défauts sont rarement considérés, cependant, leurs énergies de formation sont plus basses que celle d'autres défauts plus connus, ce qui indique qu'ils pourraient être présent dans la silice. A partir d'une étude détaillée sur les possibles mécanismes de réaction, il a été trouvé que le pont ozonil pourrait être l'un des plus important intermédiaire dans l'exchange d'oxygène avec le réseau. Les résultats montrent aussi que le dioxasialrene pourrait être formé spontanément comme réaction de loxygène avec les lone pairs des Si-ODC(II) et GLPC. Les mécanismes de passivation additionnels entre l'oxygène et les ODC peuvent présenter une barrière unique et être réversibles avec la formation de groupes de type dioxasilarene, pour lesquels le réseau conserve la mémoire de l'ODC précurseur, ou à barrière simple ou multiple mais pour lesquels le réseau perd la mémoire (du fait de barriére inverse trop haute ou du faite de la présence d'une reconstruction).

La partie finale de ce travail est dédiée à la caractérisation expérimentale de la réponse et de la tolérance de fibres optiques chargées avec de l'oxygène et sous irradiation. Ceci inclus aussi des fibres dopées avec des terres rares.

Mots clés

Silice, DFT, approximation GW, Equation de Bethe-Salpeter, NEB, défauts, oxygène, centres d'excès d'oxygéne, centres déficients en oxygéne, absorption optique, fibres optiques, atténuation due à l'irradiation.

Table des matières

1 Introduction **1**

2 Defects in silica : an Overview **3**

2.1 Diamagnetic oxygen-related centers 5

2.1.1 Oxygen deficient centers 5

2.1.2 Oxygen excess related-defects 7

2.1.3 Dioxasilirane groups 12

2.2 Radicals 12

2.2.1 E' centers 14

2.2.2 NBOHC 14

2.2.3 Peroxy radical 14

2.3 Hydrogen groups 16

2.4 Oxygen exchange, passivation and diffusion 16

2.4.1 Oxygen-related Conversion mechanisms 16

2.4.2 Oxygen diffusion 18

2.5 Defects and doping in silica-based optical fibers 19

3 Methodology **23**

3.1 Density Functional Theory 24

3.1.1 Basics of Density Functional Theory 24

3.1.2 Approximation to exchange correlation 27

3.1.3 Plane wave expansion, k-point sampling and Bloch theorem 27

3.1.4 The pseudo potential approximation 29

3.1.5 Ewald summation 31

3.1.6 Computational procedure with matrix diagonalization . . . 32

3.1.7 Calculation of forces and geometry optimization 33

3.2 GW approximation and Bethe-Salpeter equation 34

3.2.1 Basics of GW approximation 35

3.2.2 Calculation of screened Coulomb potential 38

3.3 Bethe-Salpeter equation 40

3.4 Nudged elastic band simulations 43

3.5 Results representation 45

3.6 Confocal Micro Luminescence 46

3.7 Radiation Induced Attenuation and optical absorption measurements 47

3.8 Oxygen loading of fibers 48

3.9 Optical fibers 49

4 Results and Discussion **50**

4.1 Intrinsic oxygen excess defects 50

4.1.1 Creation of model and defects 50

4.1.2 Peroxy link defect 51

4.1.3 Ozonyl defect 66

4.1.4 Gaseous O_2 73

4.1.5 Dioxasilirane 74

4.2 Defect formation mechanisms and oxygen exchange 76

4.2.1 O_2 singlet to triplet treatments 77

4.2.2 Oxygen excess centers 80

4.2.3 Oxygen deficient centers 90

4.2.4 Comparison with available experiments 97

4.3 Experimental measurements on O_2 loaded fibers 101

4.3.1 Pure silica fibers 101

4.3.2 P-doped fibers 105

4.3.3 GeCe doped fibers 108

4.3.4 PCe doped fibers 110

4.3.5 Fujikura RRMMA fiber 114

Conclusions **117**

Scientific contributions **121**

List of abbreviations

$aSiO_2$ - Amorphous-SiO_2
BCB - Bottom of the conduction band
BFGS - Broyden-Fletcher-Goldfarb-Shanno
BSE - Bethe-Salpeter equation
CC - Coupled cluster
CI - Configuration interaction
CI-NEB - Climbing image nudged elastic band
CL - Cathodo luminescence
CML - Confocal micro luminescence
DFT - Density functional theory
DIOG - DIOxaGermirane
DIOS - DIOxaSilirane
DOS - Density of states
EMPA - Electron micro probe analysis
EPR - Electronic paramagnetic resonance
FWHM - Full width at half maximum
GLPC - Germaium lone pair center
HF - Hartree Fock
HOMO - Highest occupied molecular orbital
IR - Infra red
LDA - Local density approximation
LUMO - Lowest unoccupied molecular orbital
MCVD - Modified chemical vapor deposition
MEP - Minimum energy path
MM - Multi mode
MOSFET - Metallic oxide field effect transistor
NBOHC - Non-bridging oxygen hole center
NEB - Nudged elastic band
NIR - Near infra red
NMR - Nuclear magnetic resonance
OA - Optical absorption
ODC - Oxygen deficiency centers
OF - Optical fiber
PDOS - Projected density of states
PL - Photoluminescence
POHC - Phosphorus oxygen hole center
QE - Quantum Espresso

RIA - Radiation induced attenuation
POL - PerOxy Link (bridge)
POR - PerOxy radical
SOMO - Singly Occupied Molecular Orbitals
STH - Self Trapped holes
TD-DFT - Time dependent DFT
TVB - Top of the valence band
UV - Ultra violet
VB - Valence band
XRD - X-ray diffraction
XPS - X-ray photo emission

1. Introduction

Amorphous silicon dioxide (silica) is one of the key technological materials that is extensively used in many fields. Silica is most commonly associated with opto-electronic applications like optical fibers (OF) and with gate-insulator in Metallic Oxide Field Effect Transistors (MOSFET). In the case of optical fibers silica boosts high transparency across a very broad wavelength range, which allows to transport light over great distances with unprecedented speed, stability and most importantly - reliability [1]. Silicon based semiconductor technology has relied on silica for very long time due to its high band gap [2], high breakdown current [3] and high thermal/chemical stabilities [4, 5].

In the last decade, silica based OF technology has experienced a boom with the development of sensors [6], amplifiers [7] and lasers [8] for special applications. In particular, because of its tolerance to harsh environments (temperature, toxic environments, radiation) , silica based OF are foreseen as replacement of standard electronic devices and/or for novel applications in aerospace [9] and nuclear environments [10].

The road map is still under very active and intense development. Besides trial-and-error approaches, understanding and predicting degradation and performances is a nowadays challenge. Indeed, despite more than half a century of studies on silica and silica-based materials many open questions that impact reliability of such devices still remain. Defects are either directly responsible or mediators for most of the degradation processes. To some extents, degradation can be mitigated by controlling manufacturing or operational processes (when possible) in the case of very well known defects and defects-related generation and conversion mechanisms [2].

As soon as the situation is more complex, however, understanding the underlying processes and rational optimization of the properties becomes a formidable task. Under the experimental point of view different techniques and treatments have to be combined. For instance Electronic Paramagnetic Resonance (EPR) allows for accurate detection of paramagnetic defects, however it is not able to detect diamagnetic defects, generally lacks spatial distribution and cannot be performed on-line during various treatments. Optical absorption can be used to detect optically active defects also during various treatments, however it also provides limited spatial resolution, contribution from different defects can overlap and or even worst, some optical bands can be hidden by the presence of more active defects. Photoluminescence (PL) based methods are also frequently used for

the detection of defects in silica. Application of this method is limited to emitting defects and is often applied post-mortem. In addition PL signal can be quenched due to photo bleaching of defects. A variation of this method based on electron irradiation called Cathodo Luminescence (CL) has been shown as complementary technique that allows for characterization of defect dynamics under irradiation with electrons. Major setback of these methods is that they only provide partial information of defect properties, especially regarding the atomic structure. In this context the combination of experimental data and numerical modeling can provide the needed complementary information, in particular a deep knowledge on the atomic scale structure and mechanisms.

2. Defects in silica : an Overview

An oxide is by definition a chemical compound where oxygen is combined with at least one other element [11]. Oxides are among the most abundant compounds in nature and are also extremely important in science and technology.

Among all, silicon dioxide in its amorphous form (a-SiO_2 – silica), remains the keystone in many technological applications as for instance in microelectronics and opto-electronics. Besides its un-doubtful stakes and application challenges, silica offers a unique testbed for understanding basic phenomena, as the forming elements are simple enough but its bonding nature is iono-covalent, its structure has short-to-medium-range order characteristics while its long-range structure is amorphous, its electronic-structure is very similar to its crystalline counter polymorph while its defect-related behavior is significantly richer.

Low-pressure SiO_2 polymorphs consist of SiO_4 connected tetrahedra networks [12, 2]. The Si–O bond is partly covalent and partly ionic, resulting in effective charges of about $+3.4\ e$ and $-1.7\ e$ [13] for silicon and oxygen atoms, respectively. Ideal crystalline structures are normally described in terms of primitive cells (smallest non-repetitive units) and translational symmetry (space groups). Crystalline structures are easily characterized by means of diffraction techniques [5], for instance cristobalite belongs to $P4_12_12$ group, while α-quartz is $P3_121$. The situation is, of course, significantly more ambiguous for a-SiO_2. Indeed, in the case of amorphous solids (often named fused crystals, glass or vitreous materials), as a-SiO_2, diffraction measurements provide only close neighbor information while actual details of the connectivity remain unknown.

Historically a number of theories have been proposed to describe structure of non-ordered materials [2]. In the particular case of amorphous oxides, Zachariasen's *Random network theory* [14] has been widely adopted as it provides a simple description of bonding and structure of disordered materials. Zachariasen's theory has its roots from the observation that bonding energies of ordered and disordered structures should be comparable if both can be found in nature. This implies that the oxygen in the glassy polymorph should form polyhedrals similar to its crystalline counterpart with enough space for atoms to vibrate around their respective equilibrium position. The randomization of the connection between polyhedrals (as shown in figure 2.1) does not only affect the positions of atoms but virtually all network parameters like inter-atomic distances and bond angles that consequently give rise to a distribution of inter-atomic distance and angles. For example the ideal bond angle of inter tetrahedral Si–O–Si structure is 144°

in α-quartz while in silica it varies between 120° and 180°. The distribution is Gaussian-like with mean value of 148.3° and a standard deviation of about 7.5° obtained from experimental/theoretical approaches [15]. The connectivity of amorphous SiO_4 network is often characterized by its ring structure and statistics [16, 17, 18, 19]. The density of amorphous silica is 2.196 g/cm^3 [2], identical to cristobalite and slightly lower than quartz [5]. 1 cm^3 has approximately $6.6 \cdot 10^{22}$ atoms.

Figure 2.1 shows α-quartz crystalline structure and typical a-SiO_2 model.

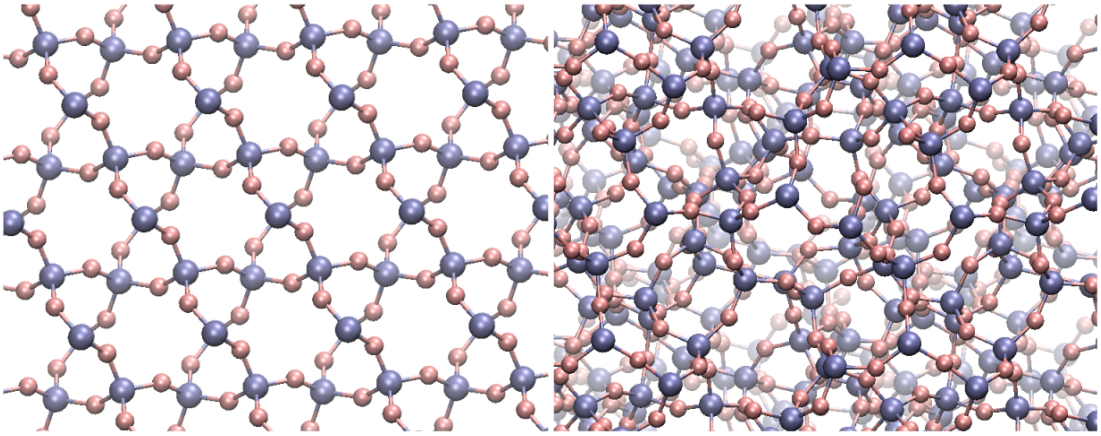

FIGURE 2.1 – Left : Atomic arrangement of ordered α-quartz structure, Right : Typical disordered amorphous silica structure

In general, a defect is identified as a change in any regular pattern. Defects are present in any material either because of thermodynamics as they reduce the Gibbs free energy [20] or because of manufacturing and/or working conditions [2, 21]. In the case of SiO_2 the pattern is perfectly connected SiO_4 tetrahedra. If a silicon/oxygen is missing/added it is referred as silicon/oxygen vacancy/interstitial. In the case of an element different from Si or O (intrinsic impurity or doping) replacing a silicon/oxygen atom then it is referred as a substitutionary defect. The reference to all the possible complexes could be build similarly.

Silica has been actively studied for over half a century and despite countless published articles there still remain a large number of unanswered questions, many of which refer to the properties and dynamics of defects.

One of the major bottleneck is originated from its disordered nature, which limits the use of some traditional experimental techniques able to detect defects like X-ray diffraction (XRD) [22]. In the case of defects that induce bonds of a significant different nature from Si–O (length or strength), a signature of this bond can be identified through Raman and/or Infra-Red (IR) spectroscopy [23]. Similarly, solid state nuclear magnetic resonance (NMR) might also provide some insight [2]. The presence of a single electron localized at a defect site (often

referred as a paramagnetic defect) can be detected through Electron Paramagnetic Resonance (EPR). EPR is of course blind to diamagnetic defects. The major optical techniques that allow to observe defect-related optical bands are Optical absorption and photo/cathodo Luminescence [24]. Most of the experimental techniques do not provide direct information of the local atomic structure. As such, bands are often labeled as centers. Link between a defect structure and its corresponding spectroscopic signature as well as its conversion mechanisms is, therefore, not straightforward. Indeed, different experiments are performed with different characterization means and treatments. In this context, computational modeling might contribute crucial insights. Concentration of defects has also been estimated to be relatively low, from 10^{13} to 10^{20} per cm^3 [21, 25], which further increases the aforementioned limitations.

All major types of neutral point defects [11] can be found in silica : Vacancies, interstitials, Frenkel and Shottky defects, impurities, diluted gas molecules and others [2].

Presence of paramagnetic defects is marginal in natural silica or in standard commercial samples and so the EPR signal is mainly absent. As such, under the experimental sensitivity pre-existing defects are generally assumed to be diamagnetic. Under irradiation, large amounts of paramagnetic defects are created either from the ionization of precursor diamagnetic defects or directly from the matrix [26]. These defects create new electronic states within the gap that open additional transport, absorption and luminescence channels which might strongly influence (degrade) performance of electronic and opto-electronic devices such as transistors, optical fibers and others. The deeper is our knowledge of defects the better we could predict the behavior of these devices under working conditions or design specific materials for targeted applications.

2.1 Diamagnetic oxygen-related centers

This section provides an overview on present knowledge regarding defects in amorphous silica. It is focused on oxygen excess defects, while other defects are briefly summarized. Each subsection ends with a table that highlight the main properties of the defects.

2.1.1 Oxygen deficient centers

The class of Oxygen Deficient Centers (ODC) describes a broad set of defects with important technological relevance [26]. Their creation is generally related to oxygen-deficiency in the local chemical environment or oxygen sub-stoichiometry

(SiO_x, $x < 2$). Table 2.1 summarizes the spectroscopic signatures (experimental and simulation) together with their corresponding structures. As the study of Si-ODCs has often been studied together with Ge-ODC(II) (also called Germanium Lone Pair Centers - GLPC in the context of luminescence experiments), table 2.1 also summarizes the main results on these centers.

Single oxygen vacancy, also known as neutral oxygen vacancy or oxygen deficient center - ODC(I), is one of the most studied defects. It is relatively easily identified by distinct optical absorption band at ∼7.6 eV with FWHM ∼0.4 eV, which has been confirmed both experimentally [24] and by ab-initio calculations [27, 28, 29]. It is diamagnetic, formed by two silicon atoms (≡Si−Si≡).

Two-fold-coordinated silicon or ODC(II) is a Si atom bonded to only two oxygens with two remaining free electrons forming a lone pair (=Si:). Historically, a long standing debate was attributing the origin for ODC(II) either to a bi-oxygen vacancy or to some kind of conversion mechanism with ODC(I) [24]. A recent theoretical study has shown that a direct conversion mechanism between ODC(I) and ODC(II) exist [30], with overall mechanisms and theoretical spectroscopic signatures in agreement with experimental observations [24]. ODC(II) is diamagnetic [31] and two optical absorption bands are associated to it, the main singlet to singlet transition at ∼5 eV with FWHM ∼0.31 eV and a second at about 3.15 eV with FWHM width ∼0.29 eV (singlet → triplet). It can be characterized further with photo luminescent bands at ∼4.4 eV, FWHM width of ∼0.45 eV with lifetime τ ∼4ns at room temperature and ∼2.7 eV, FWHM ∼0.35 eV with τ ∼10.2 ms, with first transition origin from singlet-singlet and second from triplet-singlet relaxation [24, 32, 33].

Table 2.1 – Summary of the main neutral oxygen deficiency defects and their structural/spectroscopic properties. ± is used to mark FWHM values of the bands.

Defect	O Vacancy ODC(I)	Twofold Si ODC(II)	
Structure	≡Si–Si≡	=Si :	
Type	Exp/Theo	Exp	Theo
OA (eV)	7.6±0.5	5±0.31(S→S) 3.15±0.29(S→T)	5±0.36(S→S) 3.07±0.15(S→T)
Osc. Str. / Cross. sec. σ(cm^2)	$\sigma = 7.5 \cdot 10^{-17}$ $f \sim 0.1 - 0.2$	$f = 0.15$ $f = 1.6 \cdot 10^{-7}$	$f = 0.11$
PL (eV)	4.4±0.45 τ∼4ns(S→S)	4.4±0.45 τ∼4ns(S→S) 2.7±0.35 τ∼10.2ms(T→S)	2.67±0.13 (T→S)
Ref	[24, 27, 28, 29]	[31]	[30]

2.1.2 Oxygen excess related-defects

Oxygen excess defects are related to oxygen rich environments or oxygen super-stoichiometric SiO_x ($x > 2$). These defects have been studied less compared to their oxygen deficiency counterparts however this does not diminish their technological importance [34]. A detailed biblio is provided as this field is the main focus of this work.

Oxygen interstitial

Oxygen interstitial also known as peroxy link (POL) or peroxy bridge remains one of the biggest questions in the field of defects in silica. POL has been historically considered as the main defect that incorporates excess oxygen under both normal conditions and irradiation, however it has never been detected directly in glassy SiO_2 [2]. Peroxy bridge is formed by two oxygen atoms between two silicons (≡Si–O–O–Si≡) as can be seen in figure 2.2. It is diamagnetic and no optical, vibrational or photo-luminescent bands have been clearly assigned to it.

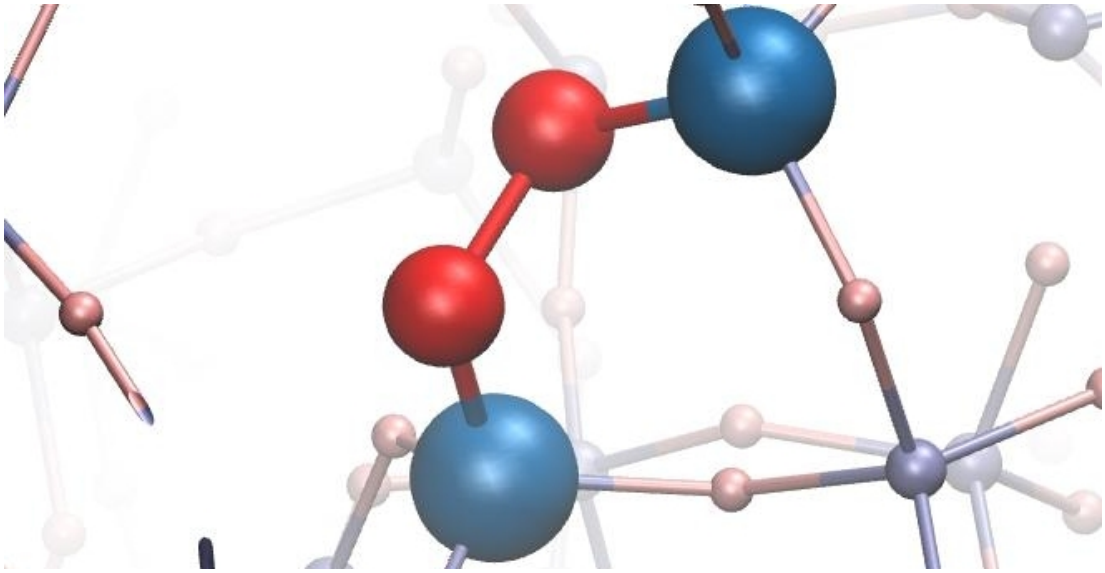

FIGURE 2.2 – Structure of POL. Oxygen atoms are represent by red balls and silicon in blue.

Peroxy link has been initially postulated as naturally occurring defect formed as a part of Frenkel pair as presented in equation 2.1. It was particularly interesting as a possible precursor of various defects such as peroxy radicals [35, 36].

$$2(\equiv \mathrm{Si} - \mathrm{O} - \mathrm{Si} \equiv) \rightleftharpoons \equiv \mathrm{Si} - \mathrm{Si} \equiv + \equiv \mathrm{Si} - \mathrm{O} - \mathrm{O} - \mathrm{Si} \equiv \tag{2.1}$$

One of the first presumable experimental detection of the POL defect in silica was described in 1989 by Nishikawa *et al.* [37]. The authors detected a weak

optical absorption around 3.8 eV in oxygen-surplus samples. After a treatment of the samples in hydrogen-rich atmosphere this peak decreased while the known absorption peak from hydroxyl group (-OH) increased significantly. Authors concluded that observed peaks probably originated from the precursory presence of POLs, as the lack of EPR signal (within the detection limit) from the initial samples excluded the presence of other pre-existing charged defects. The idea behind was that POL defects may be transformed into -OH groups during hydrogen annealing following the reaction 2.2 :

$$\mathrm{Si-O-O-Si+H_2 \rightleftharpoons Si-OH \quad HO-Si} \tag{2.2}$$

However, in later studies by Awazu *et al.* [38, 39] the 3.8 eV band has been re-assigned to the presence of Cl_2 impurities. As the Cl_2 model alone could not explain the -OH signal increase, the authors concluded that POL should also be present but with an optical signature hidden by the presence of other defects (including Cl_2 itself). Imai *et al.* [40, 41] have attributed a broad and weak absorption feature between 6.5 and 7.8 eV to the presence of POL by analyzing UV absorption of various synthetic silica glasses. This assignment was done on the same basis as Nishikawa *et al.* [37]. Indeed, the intensity of this broad band was decreasing while the -OH Infrared (IR) absorption was increasing after hydrogen treatment. At that time, there were no studies available on the contribution of -OH groups in the UV region [42]. In 2000 Y. Sakurai [43] studied the correlation between a photoluminescence band at 1.5 eV and the optical band at 3.8 eV. Because of their correlated behavior the author concluded that their origin was more likely to arise from the presence of POL than Cl_2. Skuja *et al.* [44] found weak band at 7.1 eV (FWHM of 0.7eV, oscillator strength f $\approx$ 0.01) by comparing the absorption spectra of oxygen-rich silica samples before and after laser treatment. In this study a piece of silica containing 10^{17}–10^{18} O_2 molecules (measured using characteristic O_2 PL emission) has been irradiated with F_2 laser at low (80K) and room ($\sim$300K) temperature. At both temperatures a significant decrease of O_2 PL signal has been observed without significant increase of any other known features leading authors to the idea that oxygen incorporated into network. Difference of optical spectra before and after treatment showed aforementioned weak peak at 7.1 eV.

Kajihara *et al.* attempted to detect POL using ^{18}O isotope labeled O_2 to measure the amount of oxygen that was inserted or exchanged with the silica network during thermal and F_2 laser treatments [45]. After irradiation researchers were only able to detect 65% of the initial O_2 concentration in the sample, indicating that the remaining 35% should have been incorporated into the network under some kind of defect. As none of the measured absorption bands could fully

explain the missing 35% of initial O_2, authors concluded that POL should be the main defect for the incorporation O_2, following the reaction 2.3.

$$\equiv \mathrm{Si} - \mathrm{O} - \mathrm{Si} \equiv + \frac{1}{2}\mathrm{O}_2 \rightleftharpoons \equiv \mathrm{Si} - \mathrm{O} - \mathrm{O} - \mathrm{Si} \equiv \tag{2.3}$$

More recently Mehonic *et al.* [46] have shown application of silicon oxide as a media for non-volatile data storage with very high capacity and stability. Contrary to previously described experiments that were based on silica glass, this research has been performed on a silicon rich oxide. Nevertheless, authors have shown that change of resistivity, which is the main mechanism behind data storage, is actually achieved by the migration of oxygen and formation of peroxy groups. Peroxy groups have been detected using characteristic shift of oxygen 1s orbital in –O–O– bond detected using X-ray photo-emission spectra (XPS). This could be considered as a first direct observation of POLs in silicon oxide.

On the theoretical side, the first calculation of POL absorption band was proposed by O'Reily and Robertson in classical 1983 study describing structure and optical properties of various defects by solving a tight-binding model Hamiltonian on an 243 atoms α-quartz cluster [47]. At this level of theory authors predict no significant change would be visible for disordered models. Parameters for POL defect have been adopted from H_2O_2 molecule with O–O bond length 1.49 Å and H–O–O (Si–O–O) bond angle 100°. Results show lowest σ to empty σ^* transition with an excitation energy of 8.6 eV.

Pacchioni *et al.* [27] studied the POL defect on a $Si_2O_8H_6$ cluster at different Configuration Interaction (CI) levels. Ideal POL structure is reported to be 1.43 Å, comparable to 1.45 Å of hydrogen peroxide molecule. Using bigger cluster which included full Frenkel pair yielded almost identical structure. Comparison of results for isolated defect and vacancy-interstitial pair shows almost no difference. Lowest transition has been found at 6.5 ± 0.3 eV with a very low oscillator strength (approximately 10^{-4}). This excitation was found to origin from a transition between an occupied π^* positioned on O–O group to the conduction band. Stefanov *et al.* [48] used bigger clusters compared to Ref. [27] and combination of double excitations and coupled cluster (CC) methods to find a weak singlet-to-singlet transitions at 5.5 eV (valence to empty σ^* band, $f = 10^{-4}$). Szymanski *et al.* [49] studied how structural disorder effects incorporation of POL with analysis of 48 different positions within 72 atoms amorphous-silica model. They reported a strong site-to-site dependence that effects not only local but also medium range geometry of the model. Formation (incorporation) energy of peroxy defect has been calculated using equation 2.3 and its values range from 1.1 eV to 2.7 eV with mean value of 1.9 eV. Detailed analysis has shown that there is no correlation between

structural parameters (bond angle, dihedral angle, ring sizes) and formation energy. Clear connection has been however found between bond angle of an oxygen site before incorporation and dihedral angle of created defect ; the two parameters are linearly dependent, i.e. with the increase of bond angle the dihedral angle converges towards 180°. Authors also report about relatively large discrepancy in O–O distances from two bonds of such type in single defect (one bond is usually longer than other). Correlation between incorporation energies and long range strain energies has also been described, showing that incorporation of POL changes each system uniquely implying that samples prepared using different parameters can have different properties. In final remarks authors have not only highlighted importance of statistical approach when studying disordered materials but have also shown that α quartz offers poor imitation of amorphous silica.

In Ref. [50] the authors calculated the optical absorption spectra of 7 different POL configurations in a 72-atom bulk-silica model using TD-DFT. According to their results, no correlation has been found between geometrical parameters (such as O–O, Si–Si or Si–O–O–Si angles) and excitation energies involving electronic states localized on the POL. Because the defect is strongly localized the authors concluded that the disorder would play a minor role in such transitions. The lowest excitation was found at 4.45±0.1 eV with an oscillator strength of about 10^{-3}. Authors remarked that this quantity is probably underestimated because of used TD-DFT method. Lowest excitation was found to originate mainly from transitions between an occupied σ and an empty σ^*. In one case however a different electronic transition involving σ bonding and delocalized state within the conduction band has been observed. This behavior has been explained by underestimation of wide-gap materials band gap typical for DFT based methods. Combination of many transitions near the conduction band edge with similar energy and gap underestimation eventually leads to the inversion of excitations. Authors also highlighted that medium range effects on geometry due to POL incorporation might not be properly described with cluster models, although similar statistical patterns have been observed in both cases.

Study in reference [51] provides statistical analysis of neutral defects based on 108 atom amorphous silica model. Formation energy of peroxy link is reported to be 1.6 eV with $\sigma = 0.4$ eV. Two peroxies have also been found as most probable result of silicon vacancy. Finally, clear linear connection has been found between initial local pressure of a site and formation energy of a defect.

Very recent study performed on cluster silica model at the simplest DFT level predicts a marked absorption at 7.35 eV [52]. In 2016 Wang *et al.* [53] performed some GW-BSE calculations on a bulk fused silica model which showed that POL induces three defect states due to hybridization of oxygen 2p orbitals

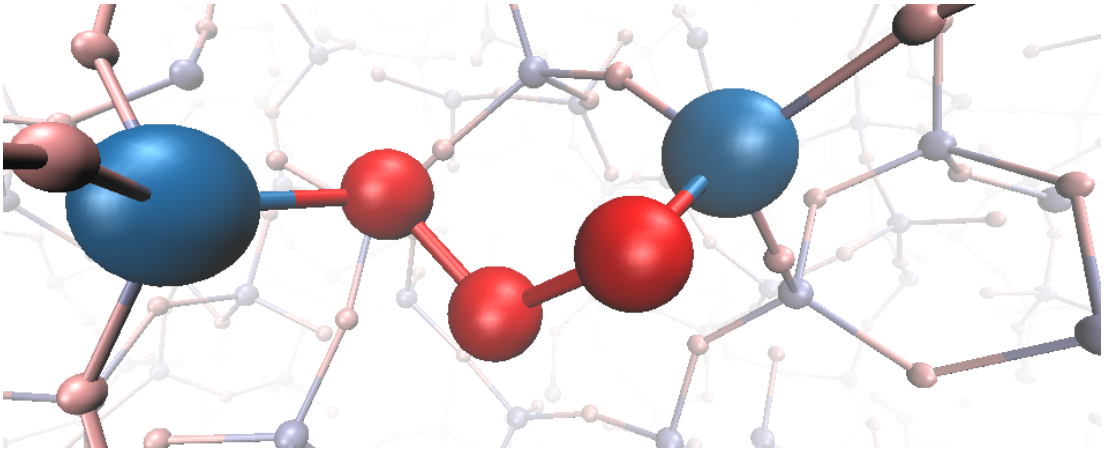

FIGURE 2.3 – Structure of ozonyl. Oxygen atoms are represented by red balls and silicon in blue.

and an unoccupied defect state coming from O 2p and Si 3s and Si 3p. The authors identified two distinct weak peaks at 4.3 and 6.6 eV to be associated with the presence of POL. The number and nature of these defect-related electronic states combined with the lack of a statistical study lead to some doubts on the representativity of results.

Ozonyl

Ozonyl (interstitial ozone molecule) is a diamagnetic defect with the structure shown in figure 2.3.

It has been first proposed as defect related to oxygen diffusion [54, 55] where results showed that it might be energetically favorable to peroxy [56]. Equation 2.4 shows proposed formation mechanism of ozonyl.

$$\equiv \mathrm{Si} - \mathrm{O} - \mathrm{Si} \equiv + \mathrm{O}_2 \rightleftharpoons \equiv \mathrm{Si} - \mathrm{O} - \mathrm{O} - \mathrm{O} - \mathrm{Si} \equiv \tag{2.4}$$

Formation of ozonyl in closed regime would require creation of two Frenkel pairs, which is, because of high formation energy (7 eV for quartz Frenkel pair [57]) not favorable. Later studies have shown it might also exist in pristine silica as a result of silicon vacancy [51].

Molecular oxygen

Oxygen is also known to exist in molecular form inside the SiO_2 matrix in form of oxygen molecule (O_2) [58] and ozone (O_3) [59].

Presence of molecular oxygen has been first detected in 1985 observing characteristic O–O stretching vibration at 1549 cm^{-1} using Raman spectroscopy. Groundwork for the detection of molecular oxygen using characteristic Raman

and photoluminescence band at ∼1270 nm (0.98 eV) is described in references [58, 60]. This approach allowed significant breakthrough of understanding reactions involving oxygen like diffusion or exchange mechanisms. Using this method concentration of molecular O_2 has been estimated between 10^{14} and 10^{18} molecules per cm^3 for various dry silica samples. Other absorption bands are related with oxygen triplet to singlet transitions at 1.62 eV ($\tau \sim 0.46$ s) and 1.79 eV, which both decay non-radiatively to 0.98 eV emission band [61]. UV absorption takes place at energies above 7 eV [34].

O_2 is known to dissociate at energies above 5.1 eV resulting in two oxygen ions [5]. Oxygen atoms are expected to be highly mobile and reactive even at room temperature. They can incorporate into the network forming, among others, defects described earlier in this subsection. Reaction of oxygen ion with another oxygen molecule leads to the formation of ozone in a reaction similar to atmospheric ozone [62]. In silica, creation of ozone is closely related to irradiation [59]. Historically 4.8 eV absorption and 1.9 eV PL emission have been a source of controversy as some studies have connected them to the presence of ozone [63, 64, 65] while others connect them to other defects like non-bridging oxygen hole centers [66, 67]. It has finally became evident that both defects have absorption bands at ∼4.8 eV although with different FWHMs (0.84 eV for ozone) [59]. Moreover ozone line is very sensitive to UV bleaching of photons with energy above 4 eV. Finally it has been observed that photo bleaching also produces O_2 singlet to triplet emission with energy ∼0.98 eV after O_3 molecule dissociation. With properties of ozone well known it might serve as another tool for better understanding of excess oxygen behavior in silica.

2.1.3 Dioxasilirane groups

Dioxasilirane groups are known to exist on SiO_2 surfaces, however they have never been identified in bulk silica [34]. These centers are formed by both atoms of oxygen molecule bonded to single silicon atom ($Si{<}O_2$). On surface they give rise to optical absorption band at 5.14 eV (σ=2.7·10^{-12} cm^2) and 3.2 eV (σ=5.3 ·10^{-20} cm^2) [68]. Green and blue PL bands have also been tentatively attributed to this defect [69, 70]. The fact that this defect has not yet been identified can be indirectly explained by very low concentrations.

2.2 Radicals

This section describes defects characterized by unpaired electrons, that are of greatest interest because of their strong emission/absorption bands and role in

TABLE 2.2 – Summary of main neutral oxygen excess defects and their structural/spectroscopic properties. ± is used to mark FWHM values of the bands.

Name	Structure	OA (eV)	Osc. str./ Cross sec. σ (cm^2)	PL (eV)	Ref
Oxygen interstitial	Si–O–Si	3.8,6.5/7.8		1.5	[37, 40, 41, 43]
		7.1 ± 0.7	∼0.01		[44]
Peroxy link/bridge		8.6, 6.5 ± 0.3	$\sim 10^{-4}$		[47, 27]
		4.45± 0.1	$\sim 10^{-3}$		[50]
Ozonyl	Si–O–O–O–Si				[54, 51]
O_2	O–O	0.98			
		1.62		0.98 $\tau \sim 0.46$ s	
		1.79		0.98 $\tau \sim 0.8$ s	[58, 60, 34, 61]
		>7.0			
O_3	O–O–O	4.8 ± 0.84			[63, 64, 65, 59]
Dioxasilirane	Si<(O_2)				

conversion to other defects.

2.2.1 E' centers

While sometimes called silicon dangling bond, this defect is best known as E'. It consists of a three-coordinated silicon atom with a single unpaired electron (≡Si·) [24]. It is paramagnetic and has therefore been studied extensively using EPR [71, 72, 73, 74, 75, 76]. E' is also characterized by clear absorption band at ∼5.8 eV and FWHM ∼0.8 eV, however no luminescence band had been clearly connected to this defect [72, 73]. While its nature seems quite simple, detailed EPR studies have shown that different configurations exist depending on the local structure [74, 75, 76]. List of most probable precursors of E' involves ODC center, Si–OH or Si–H, regular Si–O–Si under γ irradiation [2].

2.2.2 NBOHC

Oxygen dangling bond is a paramagnetic defect commonly known as non-bridging oxygen hole center (NBOHC) consisting of a single dangling oxygen bond (≡Si–O·) [77, 78, 79]. EPR studies have been fundamental for understanding many properties of NBOHC including its structure [34]. NBOHC has a characteristic absorption band at ∼1.97 eV (FWHM ∼ 0.17 eV) [2, 67, 80, 81] followed by a broad absorption feature in visible-UV domain spanning from ∼ 4 eV to ∼ 8 eV and a peak at 4.8 eV (FWHM 1.04 eV) [82, 80, 34].

An emission band has also been assigned to this defect at ∼1.91 eV with FWHM ∼0.17 eV and lifetime 10-20 µs [67, 83]. Different mechanisms have been proposed for formation of NBOHC : Breaking of regular silica bonds ≡Si–O–Si–≡ (which should produce both NBOHC and E') [84], radiolysis of OH groups [85, 86, 87] and breaking of peroxy linkage [88].

2.2.3 Peroxy radical

Peroxy radical (POR) is a paramagnetic defect with a peroxide structure and an unpaired electron (≡Si–O–O·). It has been extensively studied thanks to its strong EPR signature [35]. Its optical signature however remains one of the biggest unanswered questions in the field. Earlier studies predict absorption in the 7.6 eV region [64] while surface PORs are assumed to produce 5.4 eV band [89, 2]. It has been observed that wide component in 4.5 eV to 5.5 eV gets bleached together with the POR signal under irradiation with 5 eV photons [90].

Theoretical study estimates POR absorption at 6.4 eV (f=5·10^{-4}) using $Si_2O_8H_6$ cluster at different Configuration Interaction (CI) levels [27]. Weak

oscillator strength could be an important factor in why the absorption hasn't been clearly identified yet. POR also has no known emission bands. Study performed on optical fibers preform has shown that POR might be responsible for the ∼2.25 eV emission band, however this assignment has not been confirmed [91].

Figure 2.4 schematically shows the structure of neutral and charged defects that have been found or predicted to exist in pure silica.

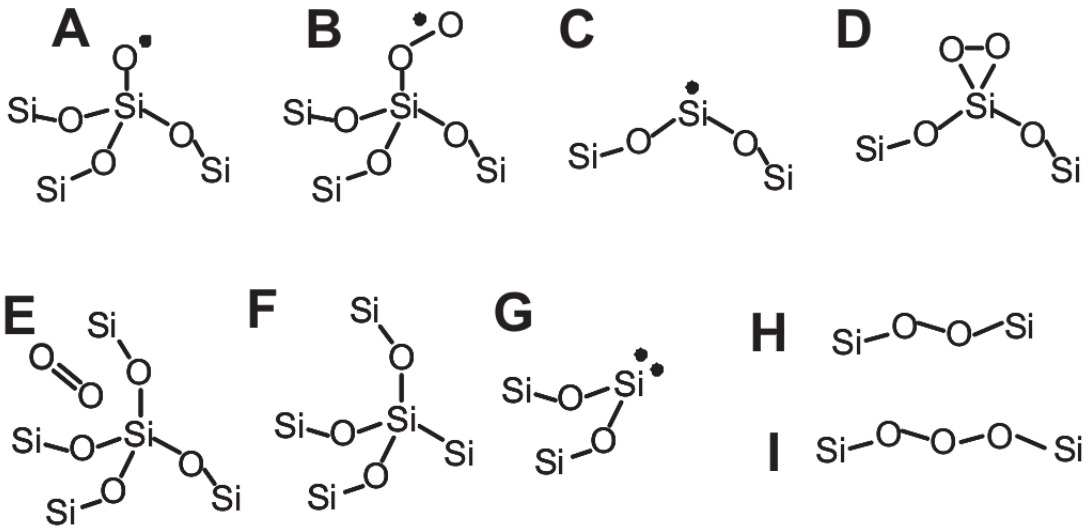

Figure 2.4 – Schematic representation of structure of defects studied in this work : A - NBOHC, B - POR, C - E', D - DIOS, E - Molecular oxygen, F - ODC(I), G - ODC(II), H - POL, I - Ozonyl. Adopted from [34]

Table 2.3 – Summary of most important radicals found in a-SiO_2 and their structural/spectroscopic properties. ± is used to mark FWHM values of the bands.

Defect	E'	NBOHC		POR		
Structure	≡Si·	≡Si–O·		≡Si–O–O·		
Type	Exp	Exp	Exp	Exp	Exp	Theo
OA (eV)	5.8±0.8	1.97±0.17	4.8±1.04	7.6, 5.4	4.5 - 5.5	6.4
Osc. Str.	0.14±0.1	$\sim 10^{-4}$	0.14			$5 \cdot 10^{-4}$
PL (eV)			1.91±0.17 $\tau \sim 10$ µs	2.25 ±0.19		
Ref	[24, 72] [73, 74] [75, 76]	[67, 77] [78, 79] [80, 81]	[82, 67] [83]	[64, 89] [2, 91]	[90]	[27]

2.3 Hydrogen groups

Hydrogen is one of the most common impurities/dopants in many forms of silica. Using infrared spectroscopies it has been determined that hydrogen generally bonds to silica in two configurations, in the form of silanol groups (≡Si–O–H) or silicon hydride (≡Si–H) [92, 93].

Silanol groups are one of the most common defects in general as the concentration might exceed 10^{20} cm^{-3} [2]. Presence of OH groups decreases local strain and in some cases even increases optical resistance to irradiation while in other cases it has been shown that resistance deteriorates significantly [94, 95, 96]. SiOH groups do not absorb with a distinct band but with a broad feature overlapping fundamental absorption edge. Silanol is also believed to be a precursor to NBOHC as significant increase of 4.8 eV absorption band has been observed under irradiation [95]. OH groups can be related to excess oxygen defects as precursors of POL supposedly shown by [37] via corresponding equation 2.2. This reaction has also been studied very recently along with the optical properties of the OH group [97]. Results show Si–O–H H–O–Si as ground state in singlet state and Si–O–O–H O–Si in triplet state. OH group introduces a defect state just above the valence band resulting in very weak absorption within the conduction band tail.

Study of Bakos [98, 99] has shown that the ground state of water in silica is in the molecular form, however silanol groups can be formed with a relatively small formation energy gain between 0.3-0.7 eV and a barrier of ∼1.5 eV.

2.4 Oxygen exchange, passivation and diffusion

A second important aspect of defect related knowledge regards chemical reactions describing their creation and conversion.

In the case of silica, complete understatement of oxygen diffusion has been historically considered fundamental because of the crucial role it plays in many technologically important processes like corrosion or semiconductor oxidation [100].

2.4.1 Oxygen-related Conversion mechanisms

O_2 exchange describes a broad set of reactions where oxygen transforms between molecular (O_2, O_3) and different network species. These reactions are fundamental for many processes related to exposure of oxides to extreme environments, diffusion, oxidation of surfaces and others. While related processes have been already extensively studied, their accurate descriptions are still not available.

While oxygen excess related defects are usually linked to oxygen rich environments they can be created in neutral conditions, for example Frenkel pair defect as shown in equation 2.1. Oxygen has also been predicted to reduce concentrations of some other defects, like E' with passivation of oxygen vacancy, which is considered as main precursor of E' with reaction shown in equation 2.5 [101].

$$\mathrm{Si-Si+O_2 \rightleftharpoons Si-O-O-Si} \tag{2.5}$$

In oxygen excess conditions POL is usually considered to be formed through dissociation and incorporation of oxygen molecule as shown in reaction 2.3.

Regarding the oxygen exchange processes, it has been already observed in the study of oxidation of silicon surface [102]. In this study Si-oxide surface has been re-oxidized with 98% pure ^{18}O isotope resulting in both increased signal of the isotope and native ^{16}O decrease clearly indicating that some sort of exchange mechanism has occurred.

Later studies were more focused towards providing accurate descriptions of exchange dynamics monitoring concentrations of observable defects [44, 45]. First study [44] describes experiments where oxygen loaded silica has been irradiated with fluorine excimer laser at low temperature followed by a series of incremental temperature increases while monitoring the concentration of O_2. Authors report that more than 99% of oxygen is photolysed under F_2 laser irradiation at 80 K. Results of heating show that 3% of initial oxygen concentration is recovered between 80 K and 180 K, further 85% are restored in second step between 470 and 670 K, while remaining 10% were restored between 870 and 1070 K. All the annealings were isochronal at 15 min. First recovery step is also accompanied by strong infrared thermo-stimulated luminescence at 1272 nm which corresponds to oxygen singlet $\rightarrow$ triplet relaxation. It has been however shown in a different study that intensity of photoluminescence decreases with temperature [101, 103, 104].

In the second study [45], isotope labeled oxygen ($^{18}O_2$) has been used to monitor the behavior of oxygen species by measuring the shifts of PL spectra sidebands. Results show that under F_2 irradiation the concentration of oxygen reduces in accordance with previous study, however additional information provided by labeled oxygen showed that only 65% of loaded oxygen formed detectable defects so the authors assumed excess was incorporated into undetectable network species like peroxy defect. After annealing the concentration of oxygen was restored, however the share of isotope labeled O_2 changed, directly proving the actual exchange between gaseous and network forms. While direct exchange with O_2 gas appears most appealing, the real process under irradiation is considerably more complex because it is known that irradiated oxygen also converts into ozone [59].

Irradiation also induces many charged defects, which are also known to facilitate oxygen excess defects (for example NBOHC conversion to POR [105]). Pacchioni [27] also considered release of oxygen with the creation of two adjacent vacancies (of Si–O–Si–O–Si $\rightarrow$ Si–Si–Si+O_2) however this reaction with the formation energy of 12 eV appears unfavorable in comparison to some other reactions.

2.4.2 Oxygen diffusion

Traditionally diffusion in silica was studied on macroscopic scale in the interest of silicon surface oxidation [105], while the technological advance has lately allowed to understand processes on atomic scale [106, 107, 55].

Some studies even postulated that oxygen in silica might migrate in a form of water because of its general abundance in materials and lower diffusivity [100].

Many experiments however showed that oxygen generally diffuses through silica in molecular form [108, 109, 110].

Growth rates of silica thin films through silicon thermal oxidation predicted by using the value of the diffusion coefficient for molecular oxygen are in good agreement with experimental observations [111]. Similarly, the values of activation energies for O_2 (calculated from Arrhenius' law) agree well with the experimental data placing it between 1.35 eV and 1.70 eV [108, 109, 110, 57]. Combination of these evidences strongly supports the idea that molecular oxygen diffuses in silica without significant interactions with the matrix [109, 110, 106]. Theoretical studies based on a combination of DFT and Monte-Carlo approaches predict lowest activation energy for O_2 diffusion around 1.12 eV [107, 55].

Some theoretical studies predict oxygen migration through network species like peroxy defects with activation energy similar to molecular oxygen [56]. Experimental results obtained from treating silica in oxygen environment provide some support to this idea [112]. Chelikowsky postulated that migration of oxygen through interstitials might not be energetically favorable as it first requires dissociation of the molecule ($h\nu$ $\sim$5.1 eV) while incorporation of whole oxygen molecule resulting in ozonyl defect might be more convenient [54].

Of course the activation of one or another mechanism will depend, not only on its activation energy but also on the conditions. For instance, at high O_2 partial pressures and ambient temperature, within the percolation regime, diffusion of oxygen occurs through diffusion of O_2 molecules [107, 51]. Understanding the whole story is relevant for the fine tuning of O_2 loading conditions, as it determines the temperature and the loading time.

2.5 Defects and doping in silica-based optical fibers

Optical fibers (OF) are dielectric waveguides of electromagnetic radiation that have established as the backbone of modern telecommunications [1]. OFs offer fast and reliable transmission over long distances unprecedented by most other media. Telecommunication applications usually exploit near-infrared (NIR) spectral domain while visible and UV domains are being researched for various technological and scientific applications such as sensors and diagnostics.

Figure 2.5 shows a very simplified scheme of basic optical fiber. Central part is named core as this is the part of the fiber where most of the light is propagating. It is surrounded by a cladding, which is a material with different refractive index n_2 (core then has refractive index n_1). In the simplest approximation the optical fiber works on the principle of total reflection described by Snell's law $\sin\theta_1 n_1 = \sin\theta_2 n_2$ where θ_1 is the angle of the incident light with respect to the normal and θ_2 is angle of the reflected light. If the angle θ_1 is large enough (depending on the ratio n_1/n_2) light will be reflected meaning that n_1 has to be larger than n_2.

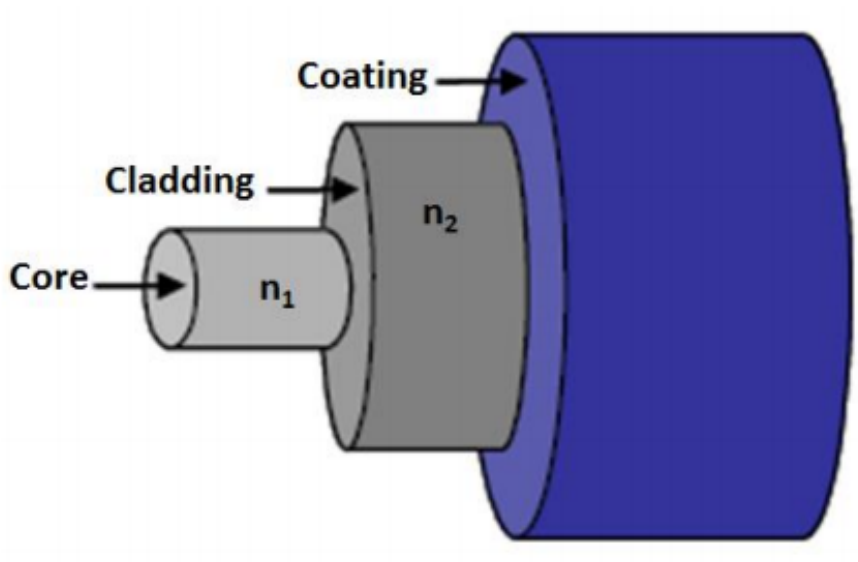

FIGURE 2.5 – Simple cut of common optical fiber with labels marking most important layers. Adapted from [113].

Change of refractive index is usually achieved by means of introducing small quantities of other elements into silica matrix in a process called doping. Most common dopants used for increasing refractive index are germanium and phosphorus while boron or fluorine are used to reduce refractive index. Solving wave equation for propagation of electromagnetic waves inside media yields properties

of light propagation. Solutions are expressed in terms of electric field spatial properties called wave guided (transverse) modes. Based on these results two main types of optical fibers exist : Single mode (SM) where only one mode of light is guided through fiber at infrared telecom wavelengths (1310 nm and 1550 nm). Such fibers have cores of small diameters ($\sim$ 10 µm) and small difference between core/cladding refractive index. On the other hand multi mode (MM)fibers support numerous modes on the whole transmission spectra and are characterized by larger core/cladding refractive index ratio.

It should be also noted that modern MM fibers can be either step-index (homogeneous index for the fiber core) or graded index (non homogeneous index in the fiber core). Graded index fibers are needed for longer distances of operation in order to reduce the dispersion issue that limits the bandwidth [1].

Losses in fibers (called attenuation) are one of the most important parameters describing practical scope of optical fibers. Figure 2.6 shows typical sources of losses in silica based optical fibers. The most important contributions are Rayleigh scattering, which is a consequence of microscopic local variation of density and its amplitude depends strongly on the wavelength (as $1/\lambda^4$), tails of UV and IR bands, waveguide imperfections and losses due to defects.

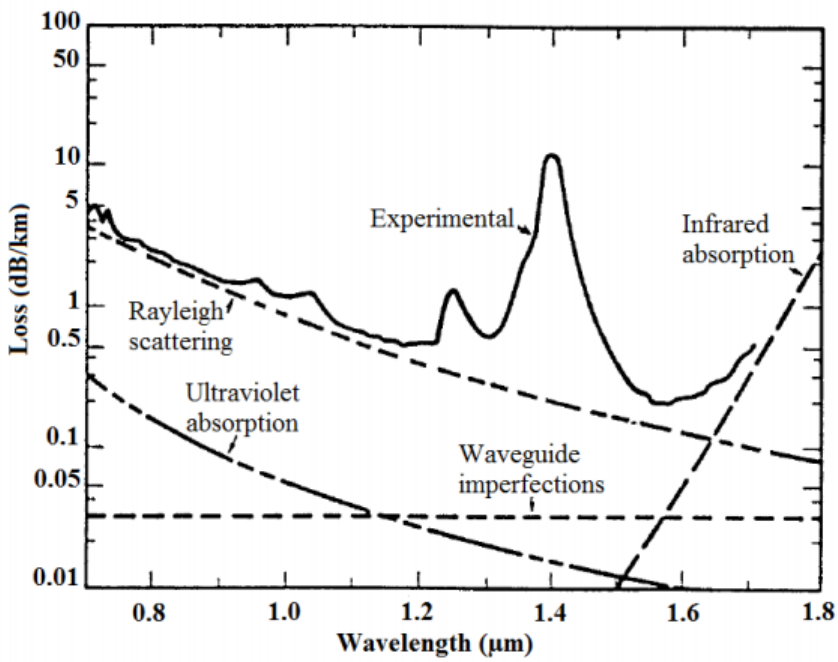

FIGURE 2.6 – Typical attenuation contributions from different sources in silica based optical fibers spectrum. Adopted from [1]

Fibers are generally fabricated in two steps, first a preform is created from which a fiber is eventually drawn. Preform is made from a glass tube into which a thin layer of silica is deposited, most commonly utilizing Modified Chemical

Vapor Deposition (MCVD) method [1, 113]. Basically silica is created by heating $SiCl_4$ in O_2 atmosphere which results in deposited SiO_2 while Cl_2 is vented from system (while in low concentration Cl impurities are always present when this method is used). As reactants are introduced in gas phase it is relatively simple to add dopants into the mix. Glass tube is then reheated until it collapses into solid rod, which is heated further until it softens (around 1600 °C) and an optical fiber is drawn from it. Drawing speed and tension are fundamental parameters in fabrication of fibers.

Telecom-grade OFs are generally doped with Ge, P and F. They are characterized by very low attenuations. Radiation resistant fibers commonly have pure silica core in order to reduce number of sites related to the dopants which could act as precursor sites for the generation of radiation induced point defects. Radiation sensitive OFs on the other hand generally exploit absorption/emission bands created by dopants like aluminum, phosphorous, cerium and others.

Furthermore rare-earth co-doped fibers extend usage into completely different field of amplification and lasers. They allow easy and low cost production of light sources and amplifiers at telecom wavelengths [114]. While this technology dates back to the 90's, it only recently became interesting for application in harsh environments, like for example space missions. Girard showed that it is possible to increase radiation resistance of optical fibers with rare-earth co-doping through the mechanism of limitation of silica matrix generated defects [115]. Such methods were successfully applied for real devices intended for space application [116].

The field is in rapid progress, in particular in the last years, and as such, the list of dopants and specific recipes are evolving and changing very fast.

Oxygen loaded optical fibers

Studies regarding effects of radiation on oxygen loaded optical fibers have also seen some rapid progress in recent years. Oxygen is not mobile at room temperature and its concentration will remain constant during the fiber lifetime. Such treatment also strongly changes the defect equilibrium under irradiation, with a positive or negative impact on the radiation induced levels and kinetics depending on the considered signal wavelength [9]. Systematic approach of D. Di Francesca described in his doctoral dissertation [113] provides great foundation in the field. Using high temperature/pressure loading method author was able to load approximately 10^{18} molecules/cm^3, which is about an order of magnitude higher compared to more standard approaches [44, 59]. In general O_2 loaded glasses have shown higher concentration of radiation induced NBOHC and presence of O_3. The concentration of E' has been noticeably reduced which can be, in combination with increased NBOHC concentration, explained by passivation mechanism displayed

in reaction 2.5. In the case of irradiated P-doped fibers it has been shown that O_2 loaded fibers see an increase of phosphorus oxygen excess related center (POHC - P analogue of NBOHC) defect while concentration of P1 (analogue to E') and P2 (4-coordinated P with free electron) decreases dramatically increasing the radiation resistance in IR region. Authors also performed similar study on Ge doped fibers loaded with oxygen [117]. GLPC is very common defect found in Ge-doped glasses with strong optical signature. It is basically ODC(II) with Ge atom substituting Si [118, 119]. Results show that loading transforms GLCP defects into different centers but the overall resistance of fibers is increased, most noticeably in the UV range. Recent studies of Di Francesca *et al.* [104] show that the oxygen-rich pure and fluorine doped silica shows very stable infra-red radio luminescence (iRL) emission in a broad thermal range making it feasible for detector applications. Similarly the group of Tomashuk [120] showed that the irradiation resistivity of pure and F-doped fibers is increased when extra oxygen is present in silica.

3. Methodology

Calculations performed in this thesis use two open source software packages for simulations at atomic scale. Ground state electronic structure, geometry optimization and reaction barrier calculations were performed using the Density Functional theory (DFT) based Quantum Espresso (QE) package [121]. SaX software [122], which is based on GW approximation, was used for calculations of quasi particles and corresponding optical properties. The computational approach is summarized in figure 3.1.

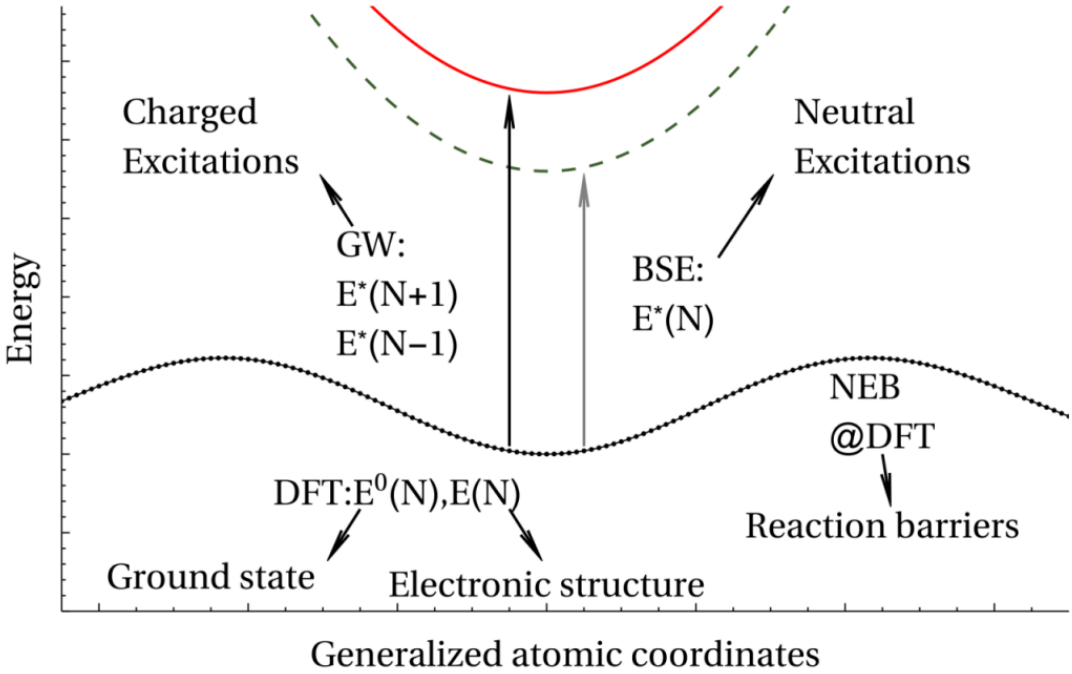

FIGURE 3.1 – Schematic representation of used computational approaches. $E^0(N)$ is the total energy of the system with N electrons in their ground state (electronic ground state is calculated within DFT framework). Migration paths and activation energies are calculated through Nudged Elestic Band with electrons in their ground state. $E^*(N-1)$ or $E^*(N+1)$ are charged excitations energies for, respectively, a system with $N-1$ or $N+1$ electrons. These energies are calculated using GW approximation that includes many-body screening. E^* are the energy of neutral excitations of a N electron system. The excitonic energies, calculated by solving the Bethe-Salpeter Equation, include many-body screened electron-hole interactions.

Experimental characterization of defect generation and interconversion has been performed in Laboratory Hubert Curien of University Jean Monnet in Saint-Etienne, France. This section of research is based on Confocal Micro Luminescence

(CML) spectroscopy/imaging and Radiation induced Attenuation (RIA) experiment. In general RIA allows for identification of generation or annihilation of optically active defects while CML enables to observe photo-luminescent defects.

3.1 Density Functional Theory

3.1.1 Basics of Density Functional Theory

Density functional theory (DFT) is a quantum mechanical modeling method widely used in computational physics, chemistry and material science. Contrary to classical approaches for solving many body problems it does not try to obtain approximate wave functions as diagrammatic expansions but it uses functionals (special functions of function) of the electron density to describe interacting system of fermions [123]. DFTs major downside is that it only provides the ground state electronic density. It has been applied to a large variety of systems giving very accurate results for ground-state properties [124]. DFT theory has been developed in the 70's on the basis of Thomas-Fermi semi-classical method for many body electronic structure calculation and received multiple corrections especially in the correlation parts constantly increasing accuracy and general scientific popularity [123, 124].

DFT is based on the variational principle of Hohenberg and Kohn that allows the determination of the exact ground state density of a specified many-particle system.

In general DFT is used for solving Schrödinger equation (3.1) describing local, spin-independent external potentials which would result in a non-degenerate ground state.

$$i\hbar\frac{\mathrm{d}}{\mathrm{d}t}\left|\Psi(\mathbf{r},t)\right\rangle = \hat{H}\left|\Psi(\mathbf{r},t)\right\rangle \tag{3.1}$$

Where i is imaginary unit, $\Psi(\mathbf{r},t)$ wave function depending on time (t) and space $(\mathbf{r})$ and $\hat{H}$ Hamiltonian operator. This equation is generally not solvable for many-body systems, however it can be simplified using various approximations.

Born-Oppenheimer is one of such fundamental approximations being generally used in many modern first principles based methods. This principle originates from the observation that mass of electrons is insignificant compared to nuclear masses and that it can therefore be safely assumed that electrons will instantly respond to any atomic movement. This allows for the separation of electronic and nuclear wave functions :

$$\Psi_{\text{total}} = \Psi_{\text{electronic}}\Psi_{\text{nuclear}} \tag{3.2}$$

Moreover, as most of the atomic elements have a De Broglie wavelength very small, the atomic degrees of freedom are always treated classically. Finding of the ground state is then separated into two loops : First the search for electronic ground-state at fixed ionic positions followed by a solution of classical Newton equations for the ions.

Furthermore assuming potential depends only on position the solution for electronic part can be expressed with variables separated :

$$\Psi(\mathbf{r}, t) = \Psi(\mathbf{r})\Psi(t) \tag{3.3}$$

This allows to separate Schrödinger equation into time and space dependent components and solve them individually. Time independent equation can be written as :

$$\hat{H} \left|\Psi\right\rangle = E \left|\Psi\right\rangle \tag{3.4}$$

Where E is constant that equals to total energy of a system. Most important aspect of this approximation is that a differential equation has been reduced into algebraic eigenvalue-eigenvector problem meaning that wave vectors are actually eigenvectors of Hamiltonian operator.

Many fermion systems are characterized by a non-relativistic time independent Hamiltonian [123]

$$\hat{H} = \hat{T} + \hat{V} + \hat{W} \tag{3.5}$$

where T is kinetic energy, W coulomb energy and V energy produced by external field.

First Hohenberg-Kohn theorem states that ground state expectation of any observable $\hat{O}$ is a unique functional of the exact ground state density (n)

$$\left\langle \Psi\left[n\right]\right| \hat{O} \left|\Psi\left[n\right]\right\rangle = O\left[n\right] \tag{3.6}$$

If ground state density is known it also determines the external potential of the system. Specifically if the kinetic and inter-particle energy are specified, they also allow determination of entire Hamiltonian.

Second statement of Hohenberg-Kohn theorem defines the variational character of the energy functional as :

$$E_{v_0}\left[n\right] := \left\langle \Psi\left[n\right]\right| \hat{T} + \hat{W} + \hat{V}_0 \left|\Psi\left[n\right]\right\rangle \tag{3.7}$$

with $\hat{V}_0$ being the external potential of a specific system with ground state density $n_0(\mathbf{r})$ and ground state energy E_0. Minimization of expression 3.7 determines the

exact ground state density.

$$E_0 = \min E_{v_0}[n] \tag{3.8}$$

According to Hohenberg Kohn theorem (3.7) a unique functional exits that depends on the density and the external potential v_s such that :

$$E_s[n] = T_s[n] + \int v_s(\mathbf{r})n(\mathbf{r})d^3\mathbf{r} \tag{3.9}$$

Using variational equation $\delta E_s[n] = 0$ gives the exact ground state density $n_s(\mathbf{r})$. In this case $T_s[n]$ represents the universal kinetic energy functional of non-interacting particles.

Kohn and Sham have established that for any interacting system there exists a local single-particle potential $v_s(\mathbf{r})$ such that the exact ground state density $n(\mathbf{r})$ of the interacting system equals to the ground state density $n_s(\mathbf{r})$ of the auxiliary problem

$$n(\mathbf{r}) = n_s(\mathbf{r}) \tag{3.10}$$

meaning that interacting v-representable densities are assumed to be also non-interacting v-representable.

In this scheme the many-body ground state density is described in terms of lowest N single-particle orbitals assuming $\hat{H}_s$ is non-degenerate so ground state density $n_s(\mathbf{r})$ is unique :

$$n(\mathbf{r}) = \sum_{i=1}^{N} |\phi_i(\mathbf{r})|^2 \tag{3.11}$$

$\phi_i(\mathbf{r})$ being lowest single particle orbital obtained from a Schrödinger like equation :

$$\left(-\frac{\hbar^2}{2m}\Delta + v_s(\mathbf{r})\right)\phi_i(r) = \epsilon_i\phi_i(\mathbf{r}), \epsilon_1 \leq \epsilon_2 \ldots \tag{3.12}$$

Using Hohenberg-Kohn uniqueness theorem on potential $v_s(\mathbf{r})$, which generates particular density $n(\mathbf{r})$, grants unique $v_s(\mathbf{r})$ meaning that single-particle orbitals are unique functionals of density $n(\mathbf{r})$

$$\phi_i(\mathbf{r}) = \phi_i([n];\mathbf{r}) \tag{3.13}$$

Adding Hartree term [123] into total energy functional yields :

$$E_{v_0}[n] = T_\mathrm{s}[n] + \int \mathrm{d}^3\mathbf{r}v_0(\mathbf{r})n(\mathbf{r}) + \frac{1}{2}\iint \mathrm{d}^3\mathbf{r}\mathrm{d}^3\mathbf{r}'\frac{n(\mathbf{r})n(\mathbf{r}')}{|\mathbf{r}-\mathbf{r}'|} + E_\mathrm{xc}[n] \tag{3.14}$$

where the exchange correlation functional E_{xc} is formally defined as :

$$E_{\mathrm{xc}}[n] = F_{\mathrm{HK}}[n] - \frac{1}{2}\iint \mathrm{d}^3\mathbf{r}\mathrm{d}^3\mathbf{r'}\frac{n(\mathbf{r})n(\mathbf{r'})}{|\mathbf{r}-\mathbf{r'}|} - T_{\mathrm{s}}[n] \tag{3.15}$$

With universal functional $F_{\mathrm{HK}}[n] = \langle\Psi[n]|\,\hat{T}+\hat{W}\,|\Psi[n]\rangle$. E_{xc} contains all interactions for which we don't know exact form and for which we need an approximation to the exchange functional.

Combining these terms yields the final expression for external potential [123] :

$$v_{s,0}(\mathbf{r}) = v_0(\mathbf{r}) + \int \mathrm{d}^3\mathbf{r}'\frac{1}{|\mathbf{r}-\mathbf{r'}|}\mathrm{n}_0(\mathbf{r'}) + \mathrm{v}_{\mathrm{xc}}\left([\mathrm{n}_0]\,;\mathbf{r}\right) \tag{3.16}$$

Equations (3.11,3.16) represent classical Kohn-Sham scheme. While this theory uses some approximations, it is in principle exact if universal exchange functional would be known.

3.1.2 Approximation to exchange correlation

The Kohn-Sham equations represent a mapping of the interacting many-electron system onto a system of non-interacting electrons in the effective potential produced by all the other particles. Complete knowledge of universal exchange correlation energy functional would produce exact total density. However approximations have to be used because the universal functional is unknown. The most common drawback of these approximate functionals is an over-counting of the electron-electron self-interaction in the Hartree term [125].

One of the frequently used approximations is Local Density Approximation (LDA), which states that exchange-correlation energy functional can be approximated by the one of the homogeneous electron gas :

$$\varepsilon_{\mathrm{XC}}(\mathbf{r}) \approx \varepsilon_{\mathrm{XC}}^{\mathrm{hom}}\left[n(\mathbf{r})\right]. \tag{3.17}$$

Various methods exist for exchange-correlation energy calculation from homogeneous electron gas that give similar accuracy. They are all based on some parametrization and are formulated to compute global minimum of the system. Calculations in this work are based on Perdew-Zunger LDA functional [126].

3.1.3 Plane wave expansion, k-point sampling and Bloch theorem

Problem of dealing with multiple non-interacting electrons moving in static background potential is covered by Bloch theorem, which states that in a periodic

lattice, wave function can be written as a periodic part and a wavelike part [127] :

$$\psi_i(\mathbf{r}) = \exp\{i\mathbf{kr}\} f_i(\mathbf{r}). \tag{3.18}$$

A very convenient choice for description of "cell function" is the expansion into a plane-wave basis set :

$$f_i(\mathbf{r}) = \sum_{\mathbf{G}} c_{i,\mathbf{G}} \exp\{i\mathbf{Gr}\}, \tag{3.19}$$

where $\mathbf{G}$ are reciprocal lattice vectors defined as $\mathbf{G} \cdot \mathbf{L} = 2\pi z$. $\mathbf{L}$ are lattice vectors and z integers. In full form electronic wave functions are expressed as :

$$\psi_i(\mathbf{r}) = \sum_{G} c_{i,\mathbf{k}+\mathbf{G}}\, exp\left[i(\mathbf{k} + \mathbf{G} \cdot \mathbf{r})\right] \tag{3.20}$$

Electronic states are sampled only at discrete k-points of Brillouin zone depending on particular system. Density of allowed k-points is proportional to the volume. System with infinite number of electrons would in principle require infinite number of k-points, while only a certain number of occupied states can exist at each k-point [125]. Bloch theorem transforms perfect problem of calculating an infinite number of electronic wave functions to calculation of a finite number of electronic states at an infinite number of k-points. However if k-points are relatively close together their description of particular states would be very similar hence it is possible to describe wave functions over a region by a single k-point. This way electronic states can be described using finite number of k-points albeit this approximation would induce certain error depending on how finite number of k-points is determined [125], denser set would normally produce more accurate results.

Bloch theorem also states that electronic wave functions at each k-point can be expressed in terms of a discrete plane-wave basis set (this is particular case useful for DFT method where discrete k-point sampling is used as will be evident later, in general different basis sets can be used). In principle an infinite set of plane vectors is needed, however coefficients $c_{i,\mathbf{k}+\mathbf{G}}$ for plane waves with smaller kinetic energy $(\hbar^2/2m)|\mathbf{k} + \mathbf{G}|^2$ are usually more important. Consequently a cut off value can be used to truncate the basis set. This approximation allows a description of wave functions with a discrete set of plane waves, i.e. with a finite basis set. Convergence has to be checked with respect to this cut-off. A correction factor can be calculated [128] for estimating the difference between theoretical infinite number of wave functions and practical finite basis sets.

Inserting plane wave function 3.20 into Kohn-Sham equation 3.12 followed by

integration over $\mathbf{r}$ simplifies expression :

$$\sum_{G'}\left[\frac{\hbar^2}{2m}|\mathbf{k}+\mathbf{G}|^2\delta_{\mathbf{GG}'}+V_{\text{ion}}(\mathbf{G}-\mathbf{G}')\right.$$
$$\left.+V_{\text{H}}(\mathbf{G}-\mathbf{G}')+V_{\text{xc}}(\mathbf{G}-\mathbf{G}')\right]c_{i,\mathbf{k}+\mathbf{G}'}=\epsilon_i c_{i,\mathbf{k}+\mathbf{G}} \tag{3.21}$$

In this form kinetic energy term is diagonal and various potentials are described in terms of their Fourier transforms. Size of the matrix depends on the cutoff energy $(\hbar^2/2m)|k+G_c|^2$.

One of the main limitations of Bloch theorem is its incapability to describe defects and surfaces. In theory infinite set of k-points would be needed but since this is not practical a super-cell must be considered. It is essential to include a bulk large enough so the defects do not interact with their respective periodic replicas. Similar approach must be applied to surfaces : Super-cells large enough that surface does not interact with its periodic bulk.

3.1.4 The pseudo potential approximation

In practice plane-wave basis set provides very limiting platform for computation of all-electron structure in real crystal as this would require extremely large cut-off for describing the strongly oscillating electronic wave functions in the core region. The pseudo potential approximation allows the electronic wave functions to be built from much smaller basis set. The basis for this approximation comes from the fact that most of the physical and chemical properties of materials depend on the valence electrons. Thus effect of core levels are replaced by weaker pseudo potentials that act on set of pseudo wave functions rather than the true valence wave functions. Pseudo potential is build in such a way that scattering properties or phase shifts for pseudo functions are identical to core level electrons and ion interaction, but with no nodes in the core region as it can be seen in figure 3.2. Thanks to the smoothing of the high spatial oscillations of the radial functions in the core the number of basis functions to describe the wave functions can be drastically reduced, thus saving computational cost.

The most general form of pseudo potential is :

$$V_{\text{NL}}=\sum_{lm}|lm\rangle\, V_l\, \langle lm| \tag{3.22}$$

where $|lm\rangle$ are the spherical harmonics and V_l is the pseudo potential for angular momentum l. This operator decomposes the wave function into spherical harmonics, each one is then multiplied with the relevant pseudo potential V_l. It is possible to

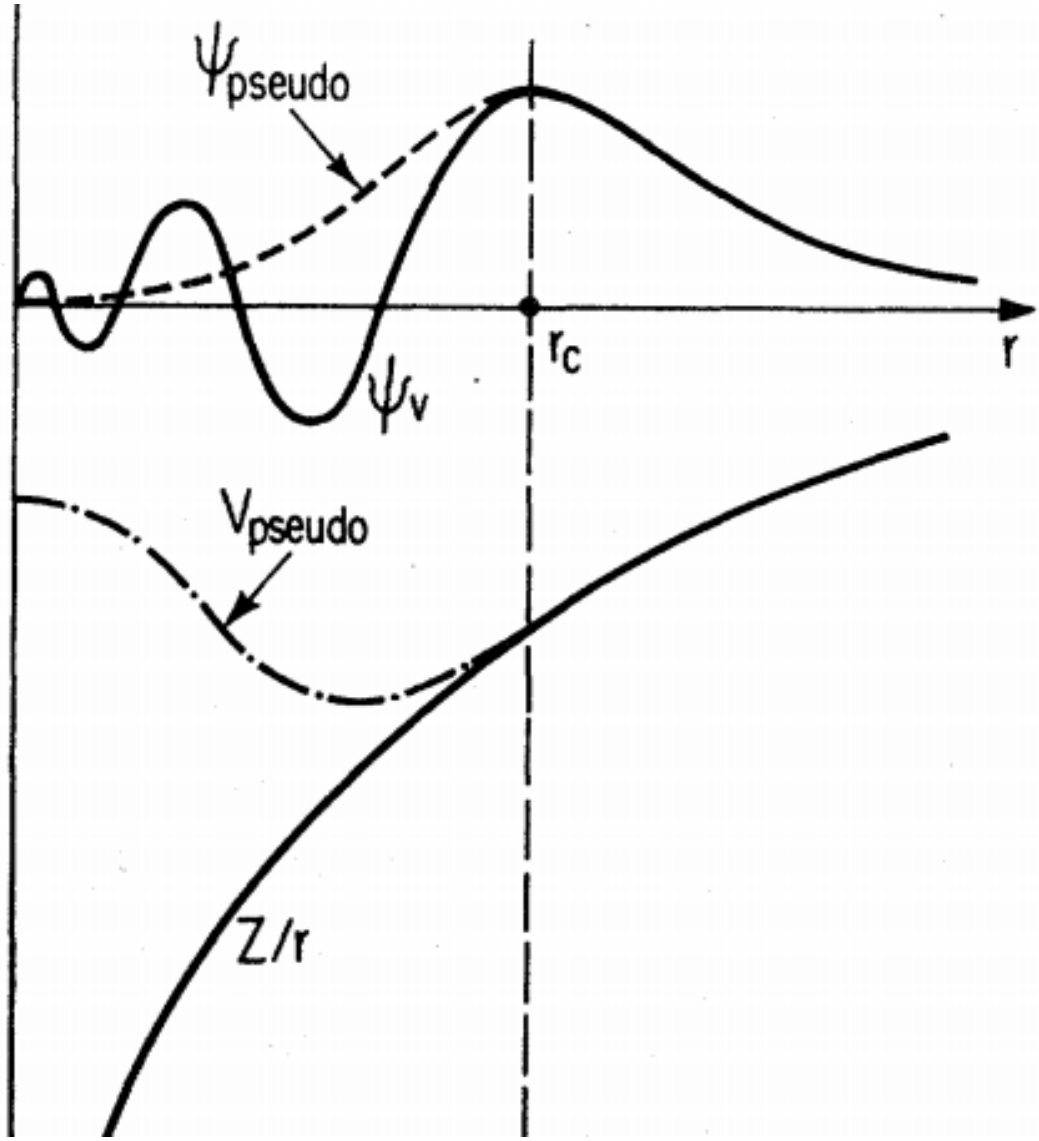

FIGURE 3.2 – Schematic illustration of real all-electron (continuous lines) and pseudo-electron (dashed lines) wave-functions (top) and potentials (bottom). r_c represents the radius after which all-electron and pseudo potential/wave function become matching. Figure adapted from [125]

produce predetermined phase shifts for each state but limitations arise with the number of those shifts maintaining sufficient smoothness. Without a smooth and weak pseudo potential, it becomes difficult to expand the wave functions using reasonable number of plane-wave basis functions. It is important that not only spatial dependences of real and pseudo functions are the same but also absolute magnitudes in order to produce same charge densities.

Pseudo potentials are very useful in simplification of DFT simulations however they have significant drawback when used in total energy calculations. Accurate description of exchange-correlation energy requires that both spatial dependencies and absolute values of pseudo wave functions produce identical values to real sys-

tem. This is normally not the case when pseudo potentials are used. Consequently corrections to the pseudo-potentials are required in order to properly reproduce behavior inside the core region needed for accurate calculations of total energies. Pseudo potentials including these kinds of corrections [125] are usually termed norm-conserving.

Total ionic potential of the solid is obtained by placing a pseudo potential at the position of each ion. Information about positions can be expressed in the terms of the structure factor for each wave vector $\mathbf{G}$ at atomic position $\mathbf{R}_I$:

$$S_\alpha(\mathbf{G}) = \sum_I \exp\left[i\mathbf{G}\cdot\mathbf{R}_I\right] \tag{3.23}$$

where the sum runs over all positions of defined specie α in single unit cell. Periodicity of the system restricts nonzero components to reciprocal lattice vectors.

Total ionic potential V_{ion} is formulated as a product of the structure factor and pseudo potential over all the atomic species :

$$V_{\text{ion}}(\mathbf{G}) = \sum_\alpha S_\alpha(\mathbf{G}) v_\alpha(\mathbf{G}) \tag{3.24}$$

At large distances pseudo potential is reduced to bare Coulomb potential (Z/r where Z is the valence of the atom). For a certain atomic specie ionic potential becomes :

$$v_{\alpha,core} = \int \left[Z/r - v_\alpha^0(r)\right] 4\pi r^2 dr \tag{3.25}$$

with v_α^0 is pseudo potential for $l = 0$ angular momentum. This integral is nonzero only within core region because the potentials are identical outside.

3.1.5 Ewald summation

The Coulomb energy is difficult to calculate using either real or reciprocal space as the interaction is always long range. Ewald developed a rapidly convergent method for Coulomb summation over a periodic lattice :

$$\begin{aligned}\sum_{\mathbf{l}} \frac{1}{|\mathbf{R}_l + \mathbf{l} - \mathbf{R}_2|} = \frac{2}{\sqrt{\pi}} \sum_{\mathbf{l}} \int_\eta^\infty \exp\left[-|\mathbf{R}_1 + \boldsymbol{l} - \mathbf{R}_2|2\rho^2\right] \mathrm{d}\rho + \\ \frac{2\pi}{\Omega} \sum_{\mathbf{G}} \int_0^\eta \exp\left[-\frac{|\mathbf{G}|^2}{4\rho^2}\right] \exp\left[i(\mathbf{R}_1 - \mathbf{R}_2)\cdot\mathbf{G}\right] \frac{1}{\rho^3} \mathrm{d}\rho\end{aligned} \tag{3.26}$$

where $\mathbf{l}$ are the lattice vectors, $\mathbf{G}$ reciprocal-lattice vectors, Ω volume of the unit cell and ρ is a smooth cutoff parameter that accounts for decay of the short range part of the coulomb potential. This identity rewrites the lattice summation for the Coulomb energy between ion position on $\mathbf{R}_2$ and an array of atoms placed

at the points $\mathbf{R}_1 + \mathbf{l}$. It holds for all the positive η. At first sight the infinite summation has been replaced by two sums, one over real and other for reciprocal space. However it has property of much faster convergence in both spaces when applied with correct η. Yet there is a problem, as the separation of sum into two spaces does not give the exact value of final total energy. So additional terms need to be included into equation 3.26.

$$E_{\text{ion}} = \frac{1}{2}\sum_{I,J} Z_I Z_J e^2 \left[\sum_{l} \frac{\text{erfc}(\eta|\mathbf{R}_1 + \boldsymbol{l} - \mathbf{R}_2|)}{|\mathbf{R}_1 + \boldsymbol{l} - \mathbf{R}_2|} - \frac{2\eta}{\sqrt{\rho}}\delta_{IJ} + \right.$$
$$\left. \frac{4\pi}{\Omega} \sum_{G\neq=0} \frac{1}{|\mathbf{G}^2|} \exp\left\{ -\frac{|\mathbf{G}|^2}{4\eta^2} \right\} \cos\left[(\mathbf{R}_1 - \mathbf{R}_2)\cdot\mathbf{G}\right] - \frac{\pi}{\eta^2\Omega} \right] \tag{3.27}$$

where Z_I and Z_J are the valences of the ions I and J. Erfc is complementary error function. As ions do not interact with their own Coulomb charge, $l = 0$ term must be omitted from the real space when $I = J$.

3.1.6 Computational procedure with matrix diagonalization

Standard procedure for DFT calculation of total energy is shown in figure 3.3. It starts by the determination of ionic potential from the atomic positions of the atoms (provided as input). Calculations require initial guess (or very simplified self consistent calculation ; trial density in figure 3.3) for electronic charge density from which Hartree potential (V_H) and exchange correlation functional can be calculated. Hamiltonian matrices are then constructed for each k-points from equation 3.21.

Kohn-Sham eigenvalues are calculated from this matrix using Davidson diagonalization. In case the results are not self-consistent procedure is repeated until convergence is achieved. Total energy usually depends more on the ionic potential than absolute energies of the individual potentials so calculations are performed using an energy cutoff and number of **k** points at which energy differences have converged rather than absolute energy convergence. Self-consistency is achieved when energy difference between two consecutive calculated values reduces below threshold.

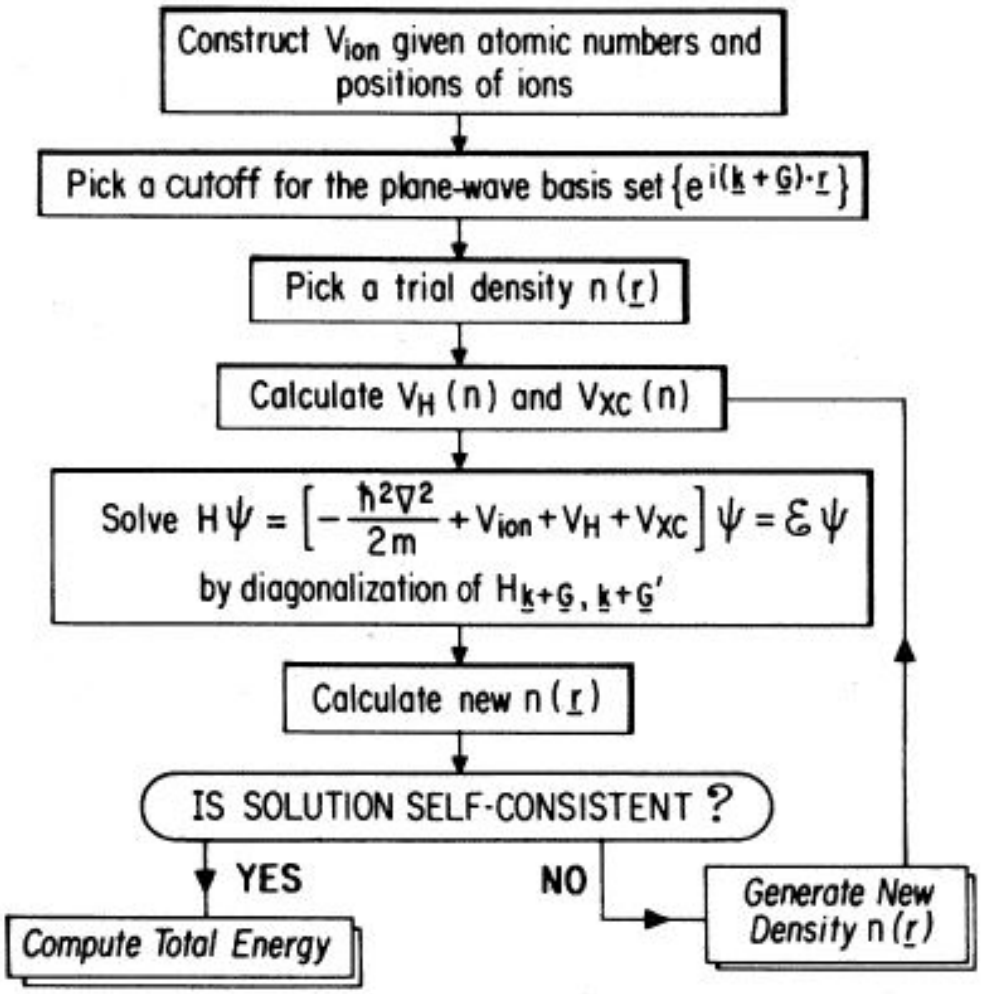

FIGURE 3.3 – Procedure for calculation of total energy using conventional matrix diagonalization. V_H and V_{XC} represent Hartree potential of electrons and exchange correlation term, which both depend on charge density $n(\mathbf{r})$. Adopted from [125].

3.1.7 Calculation of forces and geometry optimization

Force $\mathbf{f}_I$ on ion I is calculated from Hellmann-Feynman theorem as derivative of the total energy of the system with respect to the position of particular ion $\mathbf{R}_I$

$$\mathbf{f}_I = -\frac{\partial E}{\partial \mathbf{R}_I} \tag{3.28}$$

If the forces are used as part of geometry optimization calculations and the ions move, wave functions must be recalculated to new self-consistent eigenstates corresponding to new positions.

Geometry optimization, and the search for minimum of a function in general, is formidable computational problem. With forces and stresses calculated Quantum Espresso software uses powerful Broyden-Fletcher-Goldfarb-Shanno (BFGS)

algorithm to solve, now classical Newtonian problem. This algorithm works by obtaining direction $\mathbf{p}_k$ of movement by solving Newton equation

$$\mathbf{B}_I \mathbf{p}_I = -\nabla \mathbf{f}(\mathbf{R}_I) \tag{3.29}$$

Where $\mathbf{B}_I$ is an approximation of Hessian matrix that is updated after every step. In a second step one-dimensional optimization is performed to find appropriate step-size for the direction found in the first step

$$\alpha_I = \text{argmin} f(\mathbf{R}_I + \alpha \mathbf{p}_I) \tag{3.30}$$

With direction and length set the atoms can move by

$$\mathbf{R}_{I+1} = \mathbf{R}_I + \alpha_I \mathbf{p}_I \tag{3.31}$$

Forces and matrix $\mathbf{B}_k$ are then corrected after every step. Details of BFGS method are more accurately described in reference [121].

3.2 GW approximation and Bethe-Salpeter equation

While DFT is by far most commonly used method for modeling various properties of materials it has one significant flaw originating straight from its design of being ground state theory, which is the underestimation of band gap. While some further developments were somehow able to remedy this shortcoming to some extent, none of them can be considered universal. Similarly none is able to provide accurate descriptions of electronic structures for wide-gap materials [129].

Classical quantum chemistry *ab-initio* methods, largely based on Hartree-Fock (HF) method, perform better in these regards [130]. HF approach effectively reduces N-body problem into N one-body problems [131]. This theory also has significant flaw as it is impossible to describe wave-function of a system only with contributions of single particles. Indeed the overlap between exact wave function and HF approach reduces exponentially with the number of electrons N

$$|\langle \Psi_{exact} | \Psi_{HF} \rangle| \approx \exp(-\alpha N) \tag{3.32}$$

meaning this approach is more suitable to small systems than solid-state supercells. Furthermore advanced quantum chemistry approaches, aimed at improving accuracy of bare HF approach, use a diagrammatic expansion of the electronic

interactions through the bare Coulomb potential making the inclusion of electronic correlations computationally very demanding [130].

3.2.1 Basics of GW approximation

GW approximation has been developed by Lars Hedin and Stig Lundqvist in 1960's [131]. As in the case of DFT it is used to solve Schrödinger equation (3.1).

In the first approximation GW Hamiltonian can be described using Hartree-Fock approach for N-electrons

$$H = \sum_{i=1}^{N} h(\mathbf{x}_i) + 1/2 \sum_{i,j} v(\mathbf{r}_i, \mathbf{r}_j) + V_{\text{nucl}} \tag{3.33}$$

where $\mathbf{x}$ denotes both space and spin $\mathbf{x}$=($\mathbf{r}$,s), V_{nucl} is ion electron interaction and since it can be considered as external potential, v coulomb interaction between electrons and h one electron part defined as

$$h(\mathbf{x}) = -(\hbar^2/2m)\nabla^2 - \sum_n Z_n v(\mathbf{r}, \mathbf{R}_n) \tag{3.34}$$

As mentioned earlier, HF theory does not describe systems with many electrons well (equation 3.32). This is mainly because HF approach does not include any description of correlation effects which are fundamental for electronic interactions of large systems. For the interpretation of the many-body problem describing electrons interacting with each others a Hamiltonian H that contains two terms needs to be defined : The ground state H_0 and a perturbing term H_1. $\phi(\mathbf{x}, t)$ represents small external perturbing potential.

$$\begin{gathered} H = H_0 + H_1 \\ H_0 = \int \Psi^\dagger(\mathbf{x}) h(\mathbf{x}) \Psi(\mathbf{x}) \mathrm{d}\mathbf{x} + \frac{1}{2} \int \Psi^\dagger(\mathbf{x}) \Psi^\dagger(\mathbf{x}') v(\mathbf{r}, \mathbf{r}') \Psi(\mathbf{x}') \Psi(\mathbf{x}) \mathrm{d}\mathbf{x} \mathrm{d}\mathbf{x}' \\ H_1 = \int \Psi^\dagger(\mathbf{x}) \Psi(\mathbf{x}) \phi(\mathbf{x}, t) \mathrm{d}\mathbf{x} \end{gathered} \tag{3.35}$$

The annihilation field operator $\Psi(\mathbf{x}, t)$ satisfies the equation of motion :

$$i\frac{\partial \Psi(\mathbf{x}, t)}{\partial t} = [h(\mathbf{x}) + \phi(\mathbf{x}, t)]\, \Psi(\mathbf{x}, t) + \int v(\mathbf{r}, \mathbf{r}') \Psi^\dagger(\mathbf{x}', t) \Psi(\mathbf{x}', t) \Psi(\mathbf{x}, t) \mathrm{d}\mathbf{x}' \tag{3.36}$$

Using the relation $\mathrm{d}\Theta(t)/\mathrm{d}t = \delta(t)$ and the commutation rules at equal times for

$\Psi(\mathbf{x},t)$ and $\Psi^{\dagger}(\mathbf{x},t)$ one electron Green function can be obtained :

$$\begin{gathered}[i(\partial/\partial t)-h(\mathbf{x})-\phi(\mathbf{x},t)]\,G(\mathbf{x}t,\mathbf{x}'t') \\ +i\int v(\mathbf{r},\mathbf{r}'')d\mathbf{x}''\,\langle N|\,T\left\{\Psi^{\dagger}(\mathbf{x}'',t)\Psi(\mathbf{x}'',t),\Psi(\mathbf{x},t),\Psi^{\dagger}(\mathbf{x}',t)\right\}|N\rangle \\ =\delta(\mathbf{x},\mathbf{x}')\delta(t,t')\end{gathered} \tag{3.37}$$

Where N is a quantum state of a system. This term with four field operators contains two particle Green function and describes two-body correlations in the system. It can be used as basis for formation of infinite chains for more complicated correlations.

To describe interaction of a particle with the rest of the system a notation can be generalized with the introduction of a nonlocal time (or energy) dependent quantity called the self-energy operator Σ which is defined from equation 3.37 as :

$$\begin{gathered}[i(\partial/\partial t)-h(\mathbf{x})-V(\mathbf{x},t)]\,G(\mathbf{x}t,\mathbf{x}'t') \\ -\int\Sigma(\mathbf{x}t,\mathbf{x}''t'')G(\mathbf{x}''t'',\mathbf{x}'t')\mathrm{d}\mathbf{x}''\mathrm{d}t''=\delta(\mathbf{x},\mathbf{x}')\delta(t,t')\end{gathered} \tag{3.38}$$

The quantity $V(\mathbf{x},t)$ is the total average potential in the system :

$$V(\mathbf{x},t)=\phi(\mathbf{x},t)+\int v(\mathbf{r},\mathbf{r}')\,\langle N|\,\Psi^{\dagger}(\mathbf{x}'t)\Psi(\mathbf{x}',t)\,|N\rangle\,\mathbf{d}\mathbf{x}' \tag{3.39}$$

It is more convenient to use frequency domain when dealing with energies therefore Fourier transformation is applied :

$$G(\mathbf{x},\mathbf{x}';\omega)=\int G(\mathbf{x}t,\mathbf{x}'t')\exp\left[i\omega(t-t')\right]\mathrm{d}(\mathrm{t}-\mathrm{t}') \tag{3.40}$$

This expression is not valid unless G depends only on time arguments, implying time independence (or zero value) of external potential $\phi(\mathbf{x},t)$. Fourier transform of self energy operator 3.38 becomes

$$[\omega-h(\mathbf{x})-V(\mathbf{x})]\,G(\mathbf{x},\mathbf{x}';\omega)-\int\Sigma(\mathbf{x},\mathbf{x}'';\omega)G(\mathbf{x}'',\mathbf{x}';\omega)\mathrm{d}\mathbf{x}\mathrm{d}\omega=\delta(\mathbf{x},\mathbf{x}') \tag{3.41}$$

Complicated many-body character of G originates in energy dependence of the self-energy Σ. If it did not depend on energy the set of equations could be solved for a set of eigenfunctions u_k. Since this in not generally the case, one of the possible solutions is to find physically meaningful approximations.

When dynamical interactions are included the full Green function is needed, and the self energy has to be interpreted as a functional of $G:\Sigma=\Sigma(G)$. Formally

it can be expressed from the dynamically screened Coulomb potential W as :

$$W(12) = \int v(13)\epsilon^{-1}(32)\mathrm{d}(3) \tag{3.42}$$

Introduction of the following abbreviated notation greatly simplifies perception :

$$(1) = (\mathbf{x}_1, t_1), \quad v(12) = v(\mathbf{r}_1, \mathbf{r}_2)\delta(t_1 - t_2) \tag{3.43}$$

Inverse dielectric function ϵ^{-1} obtained from classical theory measures screening of change δV due to small variation $\delta\phi$ in the external potential where ρ is electronic density.

$$\epsilon^{-1}(1,2) = \frac{\delta V(1)}{\delta\phi(2)} = \delta(12) + \int v(13)\frac{\delta\langle\rho(3)\rangle}{\delta\phi(2)}\mathrm{d}(3) \tag{3.44}$$

The key quantity needed to be calculated is the irreducible polarizability P, with ϵ related to P as :

$$\epsilon(12) = \delta(12) - \int P(32)v(13)\mathrm{d}(3). \tag{3.45}$$

And W can be expressed as a function of P :

$$W(12) = v(12) + \int W(13)P(34)v(42)d(34) \tag{3.46}$$

The self energy Σ and P can now be written as functional derivatives :

$$\Sigma(12) = -i\int v(13)G(14)\frac{\delta G^{-1}(42)}{\delta\phi(3)}\mathrm{d}(34) \tag{3.47}$$

$$P(12) = i\int G(23)G(42)\frac{\delta G^{-1}(42)}{\delta V(1)}\mathrm{d}(34) \tag{3.48}$$

Finally, the vertex Γ is defined as :

$$\Gamma(12;3) = -\frac{\delta G^{-1}(12)}{\delta V(3)} = \delta(12)\delta(13) + \frac{\delta\Sigma(12)}{\delta V(3)} \tag{3.49}$$

Equations 3.46, 3.47, 3.48, 3.49 can be rewritten as a set defining Σ. This set is commonly refereed to as "Hedin equations".

$$\Sigma(12) = i\int W(1^+3)G(14)\Gamma(42;3)\mathrm{d}(34) \tag{3.50}$$

$$W(12) = v(12) + \int W(13)P(34)v(42)\mathrm{d}(34) \tag{3.51}$$

$$P(12) = -i \int G(23)G(42)\Gamma(34;1)\mathrm{d}(34) \tag{3.52}$$

$$\Gamma(12;3) = \delta(12)\delta(13) + \int \frac{\delta\Sigma(12)}{\delta G(45)} G(46)G(75)\Sigma(67;3)\mathrm{d}(4567) \tag{3.53}$$

Hedin's equations in general are still considered too difficult (or time consuming) for practical applications.

GW approximation are actually Hedin equations simplified by setting the vertex term to 1 as :

$$\Gamma(12;3) = \delta(12)\delta(13) \tag{3.54}$$

Rewritten and simplified equations of GW approximation then read as :

$$\Sigma = iGW \tag{3.55}$$

$$G = G_0 + G_0\Sigma G \tag{3.56}$$

$$\Gamma = 1 \tag{3.57}$$

$$P = -iGG \tag{3.58}$$

$$W = v + vPW \tag{3.59}$$

As in the case of DFT these equations are solved iteratively, in the first step G is considered as G_0 and Σ=0. GW approximation in general involves screening effects of electron cloud affecting coulomb interaction between particular particles. If screened potential W is replaced with bare Coulomb interaction GW approach reduces to Hartree-Fock method. Screened interactions also have smaller range than bare Coulomb forces which has two important consequences, faster convergence and smaller overestimation. In summary, GW provides the ($N\pm1$) quasi particle electronic structure. It does not however account for electron-hole interactions in the dielectric response function meaning that while it provides better values for energies of empty states it still does not describe optical transitions.

3.2.2 Calculation of screened Coulomb potential

GW approximation can be normally calculated self-consistently. However this approach is generally not efficient as the computational costs are relatively high. One approach that is commonly used, as in the case of software used in this

work [122], is to use DFT ground state results as starting point. DFT initial wave functions are assumed to be very close to the "real" quasi-particle wave functions and are not re-calculated, while DFT Kohn-Sham energies are corrected with a diagonal GW self-energy. In the literature this approximation is often referred as GW@DFT or G_0W_0 [129]. As the GW correction does not come from a diagonalization of complete hamiltonian, and DFT exchange-correlation potentials fail in describing energy differences between electronic states of different nature (delocalized-localized, occupied/un-occupied) sometimes a change in the energy ordering of the states may appear between DFT and GW@DFT.

The first step for GW calculation is evaluation of polarizability P. In order to do so a product between two Kohn-Sham states is used :

$$M_{nk,n'k'}(x) = \sqrt{N\Omega}\Psi^*_{nk}(x)\Psi_{n'k'}(x) \tag{3.60}$$

where Ω is volume of unit cell and N number of considered unit cells. Because of the poles at excitations energies on the real axis, the calculation of W and subsequent integration is performed on the imaginary axis ($\omega = is$) that has a smoother numerical behavior (analytic continuation). The expression for polarizability in reciprocal space is :

$$\begin{aligned} P_q(GG';is) = -\frac{4}{N\Omega}\sum_{cvqk}\theta(\epsilon_{ck}-\mu)\theta(\mu-\epsilon_{vk+q}) \\ M^*_{ck,vk+q}(G)M_{ck,vk+q}(G')\frac{2(\epsilon_{ck}-\epsilon_{vk+q})}{(\epsilon_{ck}-\epsilon_{vk+q})^2+s^2} \end{aligned} \tag{3.61}$$

μ in the Fermi energy, so the θ function selects a band index v, which belongs to occupied bands (valence) and bands c representing unoccupied states (conduction).

Ideally, sums over k and q should be performed over infinitely dense mesh in first Brillouin zone. In practice special points technique is used : Fourier quadrature of the integrand [122].

Second step is to compute screened Coulomb potential, obtained as :

$$W(is) = \left[1 - v^c P(is)\right]^{-1} v^c \tag{3.62}$$

For imaginary frequencies W is Hermitian as well. Screened Coulomb potential can be split into pure exchange and pure correlation by subtracting v^c. This way the exchange self-energy is given by :

$$\langle nk|\,\Sigma_x\,|n'k\rangle = -\frac{1}{N\Omega}\sum_{vq}\sum_{G}\theta(\mu-\epsilon_{vk-q})M^*_{vk-q,nk}(G)v^c_q(G)M_{vk-q,n'k}(G) \tag{3.63}$$

and correlation by :

$$\langle nk| \Sigma_c(\omega) |n'k\rangle = -\frac{1}{N\Omega}\sum_{n''q}\sum_{GG'} M^*_{n''k-q,nk}(G)M_{n''k-q,n'k}(G') \\ -\frac{1}{2\pi i}\int d\omega' \frac{W^P_{GG'(q;\omega')}e^{-i\delta\omega'}}{\omega+\omega'-\epsilon_{n''k-q}-i\eta\text{sign}(\mu-\epsilon_{n''k-q})} \tag{3.64}$$

Setting σ_c to zero will again give Hartree-Fock approximation. This integral is problematic to solve and computationally demanding for systems with more than a few electrons. In this case Godby-Needs [132] plasmon-pole model has been used because it allows for an analytical solution of the energy integral.

The dynamical behavior of the dielectric matrix is given by a parametrized model of the dielectric function in reciprocal space :

$$\varepsilon^{-1}_{GG'}(q;\omega) = \delta_{GG'} + \frac{\Omega^2_{GG'}(q)}{\omega^2 - \omega_{GG'}(q)^2} \tag{3.65}$$

where $\Omega_{GG'}$ (effective bare plasma frequency) and $\omega_{GG'}$ are the two parameters of the model. These frequencies are chosen, when ϵ^{-1} is actually computed, as : $\omega = 0$ and $\omega = i\omega_p$ (ω_p is an estimate for plasmon frequency). This should only work, in principle, for systems where plasmons are well defined. However, it has been also applied to molecules and has given very accurate results.

3.3 Bethe-Salpeter equation

In order to properly calculate optical excitations Bethe-Salpeter equation is used. It must be assumed that excited state can be calculated as a coherent linear superposition of vertical interacting electron-hole excitations :

$$|E\rangle = \sum_{nn'k} A_{nn'k}\hat{a}^\dagger_{nk}\hat{a}_{n'k}|O\rangle + |C\rangle \tag{3.66}$$

with $|C\rangle$ being higher order correction.

Eigenstate $|E\rangle$ and energy Ω of "unknown" excitonic state can be calculated from :

$$\bar{H}|E\rangle = \Omega|E\rangle \tag{3.67}$$

$|E\rangle$ can be written in the basis of single-particle orbitals as :

$$\Psi(xx') = \sum_{nn'k} \psi^{qp}_{nk}(x)\psi^{qp*}_{n'k}(x') \tag{3.68}$$

Excitation energies are solutions of an eigenvalue problem and it is necessary

to find a form of effective two-particle Hamiltonian of equation 3.67. In the context of neutral excitations, this effective two-particle Hamiltonian is called the Bethe-Salpeter equation, describing electron-hole pairs.

The information about this excitation is given as two-particle Green-Function :

$$G_2(x_1t_1, x_2t_2, x_3t_3, x_4t_4) = (-i)^2 \langle N| T\{\Psi(x_1t_1)\Psi(x_2t_2)\Psi^\dagger(x_3t_3)\psi^\dagger(x_4t_4)\} |N\rangle \tag{3.69}$$

G_2 describes the propagation of created electron-hole pair and $|N\rangle$ is the ground state of N particle system.

Four point independent particle polarizability is relatively similar to the polarizability of GW method :

$$P^0(1,1';2,2') = -iG(1',2')G(2,1) \tag{3.70}$$

Generalized form for response function is then :

$$\begin{aligned}\chi(1,1',2,2') = P_0(1,1',2,2') + \int P_0(1,1',3,3')[v(3,3',4,4') \\ -W(3,3',4,4')]\bar{P}(4,4',2,2')\mathrm{d}3\mathrm{d}3'\mathrm{d}4\mathrm{d}4'\end{aligned} \tag{3.71}$$

Expression for polarizability differs only in term of long range Coulomb potential ($v \to \bar{v}$).

In practice all of the quantities are calculated in frequency domain thus requiring Fourier transform :

$$\chi(1,1',2,2') = \chi(x_1t_1, x_1't_1^\dagger, x_2t_2, x_2't_2^\dagger) \to \chi(x_1, x_1', x_2, x_2', \omega)\delta(x_1 - x_1')\delta(x_2 - x_2') \tag{3.72}$$

Another important assumption implemented is the energy dependence of the screen potential which is neglected assuming $W(\omega) = W(\omega = 0)$. In theory this could be solved by inverting the matrix for each possible frequency ω. However there exists a more practical way, reformulating the problem into an effective eigenvalue problem. First step consists of changing the basis set, consisting of single particle eigenfunctions $\psi_n(x)$ (the subindex n has to be read as $n = (n,k)$, it now contains the information of the band and k point). In this basis four point quantities become :

$$S(x_1, x_{1'}, x_2, x_{2'}) = \sum_{(n_1,n_{1'})(n_2,n_{2'})} \psi^*_{n_1}(x_1)\psi_{n_1'}(x_1')\psi_{n_2}(x_2)\phi^*_{n_2}(x_{2'})S_{(n_1,n_{1'})(n_2,n_{2'})} \tag{3.73}$$

The active eigenvalue problem now becomes :

$$\sum_{(n_1,n_{1'})(n_2,n_{2'})} H_{(n_1,n_{1'})(n_2,n_{2'})^{2p}} A^{\mu}_{(n_2,n_{2'})} = E^{\mu} A^{\mu}_{(n_2,n_{2'})} \tag{3.74}$$

where the two-particle Hamiltonian is :

$$H_{(n_1,n_{1'})(n_2,n_{2'})^{2p}} = (\epsilon_{n_{1'}} - \epsilon_{n_1})\delta_{(n_1,n_2)(n_{1'},n_{2'})} + (f_{n_1} - f_{n_{1'}})\Xi_{(n_1,n_{1'})(n_2,n_{2'})} \tag{3.75}$$

with $\epsilon_{n_{1'}}$ and ϵ_{n_1} being quasi particle energy eigenvalues and $\Xi_{(n_1,n_{1'})(n_2,n_{2'})}$ presenting the interaction kernel, defined as :

$$\begin{aligned}\Xi_{(n_1,n_{2'})(n_2,n_{2'})} = &-\int \mathrm{x}_1\mathrm{x}x_{1'}\psi_{n_1}\psi^*_{n_{1'}}(x_{1'})W(x_1,x_{1'})\psi^*_{n_2}(x_1)\psi_{n_{2'}}(x_1) \\ &+\int \mathrm{x}x_1\mathrm{x}x_{1'}\psi_{n_1}(x_1)\psi^*_{n_{1'}}(x_1)v(x_1,x_{1'})\psi^*_{n_2}(x_{1'})\psi_{n_{2'}}(x_{1'})\end{aligned} \tag{3.76}$$

In general A^{μ} are not orthogonal. In the case of semiconductors this expression can be simplified : $(f_{n_1} - f_{n_{1'}})$ is different from zero only for transitions for which $(n_1, n_{1'})$= (occupied, unoccupied) or vice versa.

The matrix representation of the two body Hamiltonian for a semiconductor-insulator is :

$$\begin{pmatrix} [c|cccc] & v_c, c_2 & c_2, v_2 & v_2, v_{2'} & c_2, c_{2'} \\ \hline v_1, c_1 & H^{2p}_{(v_1c_1)(v_2c_2)} & \Xi_{(v_1c_1)(c_2v_{2'})} & \Xi_{(v_1c_1)(v_2v_{2'})} & \Xi_{(v_1,c_1)(c_2c_{2'})} \\ c_1, v_1 & -\Xi_{(c_1,v_1)(v_2c_2)} & -H^{2p}_{(c_1v_1)(c_2v_2)} & -\Xi_{(c_1v_1)(v_2v_{2'})} & -\Xi_{(c_1v_1)(c_2c_{2'})} \\ v_1, v_{1'} & 0 & 0 & e_v\delta_{(v_1,v_2)(v_{1'},v_{2'})} & 0 \\ c_1, c_{1'} & 0 & 0 & 0 & e_c\delta_{(c_1,c_2)(c_{1'},c_{2'})} \end{pmatrix} \tag{3.77}$$

where $e_v = (E_{v_{1'}} - E_{v_1})$ and $e_c = (E_{c_{1'}} - E_{c_1})$. v_i and c_i stand for valence and conduction states, respectively.

In "block" representation matrix for H^{2p} is :

$$\begin{pmatrix} H^{2p-\text{resonant}}_{(v_1c_1)(v_2c_2)} & \Xi^{\text{coupling}}_{(v_1c_1)(c_2v_2)} \\ -\left[\Xi^{\text{coupling}}_{(v_1c_1)(c_2v_2)}\right]^* & -\left[H^{2p-\text{resonant}}_{(v_1c_1)(v_2c_2)}\right]^* \end{pmatrix} \tag{3.78}$$

$H^{2p-\text{resonant}}$ is Hermitian and corresponds to positive absorption energy while $-\left[H^{2p-resonant}\right]$ gives de-excitation energies. Ignoring the coupling part of the matrix the eigenvalue problem is reduced to :

$$\sum_{(v_2,c_2)} H^{\text{exc ,2p resonant}}_{(v_1,c_1)(v_2,c_2)} A^{\mu}_{(v_2,c_2)} = E^{\text{exc}}_{\mu} A^{\mu}_{(v_1,c_1)} \tag{3.79}$$

Diagonalization of resonant part provides the exitonic structure. Differently to GW, screening has been approximated with the static picture.

Finally the macroscopic dielectric tensor is calculated which provides information about the oscillator strength of optical transitions :

$$\epsilon_M = 1 - \lim_{q \to 0} v_0(\mathbf{q}) \sum_n \sum_{v_1, c_1} \frac{|M_{c_1 k-q, v_1 k}(0) A^{\mu}_{(v_1, c_1)}|^2}{\Omega^{\mu} - \omega - i\eta} \tag{3.80}$$

This function provides probability of excitations as "raw" number at given energy, ie. plot would picture particular excitations as delta functions.

3.4 Nudged elastic band simulations

An important problem in theoretical materials science is the identification of the lowest energy path from one stable configuration to another. This path is often referred to as "Minimum energy path" (MEP). Potential energy maximum along the MEP is a saddle point which describes the activation energy for the transition. This problem is still one of the most active research fields [133]. Many methods have been presented for finding MEPs [134]. First order saddle point is, in principle, a maximum in one direction and minimum in all others. These methods must invariably depend on some kinds of degrees of freedom minimization/maximization. Main issue is how to properly identify critical degrees of freedom.

Nudged elastic band (NEB) has been proven as efficient method for finding MEP between two stable states. Schematic overview of MEP optimization is shown in figure 3.4. NEB method finds minimum energy path by constructing a set of images (typically in range of 5-20) between initial and final step, marked as gray ellipsoids in figure 3.4. In Quantum Espresso software [121] an initial path is constructed as linear interpolation between initial ($\mathbf{R}_0$) and final image ($\mathbf{R}_N$). A spring interaction is calculated between adjacent images to ensure continuity of the path by roughly equalizing the distance between images. This interaction mimics an elastic band hence the name. Without the spring constrain the higher energy images could slide toward lower energy images. Optimization of the "elastic band" reduces force between images bringing path to minimum energy.

Essential feature of NEB is a force projection ensuring that the spring forces (forces between adjacent images) do not affect convergence of the band towards MEP while "true" forces (forces created by the geometrical optimization of individual images) do not effect distribution of images along the path. This means that only perpendicular component of "true" force and parallel part of spring forces are included with a projection referred as "nudging".

Reaction path is separated into [$\mathbf{R}_0$,$\mathbf{R}_1$,$\mathbf{R}_2$,...,$\mathbf{R}_N$] images where end points

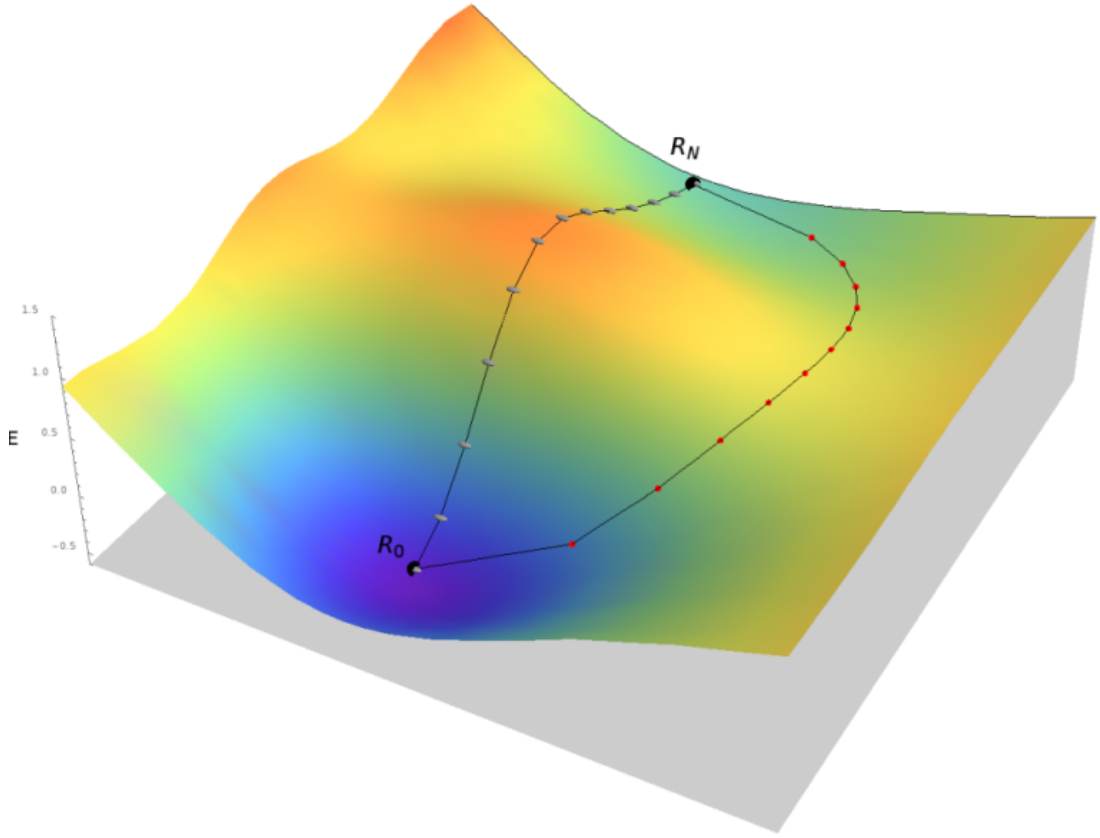

FIGURE 3.4 – Schematic representation of initial NEB path and MEP. $\mathbf{R}_0$ and $\mathbf{R}_N$ represent initial and final configurations respectively. Gray ellipsoids mark initial path while red circles are used to label MEP.

$\mathbf{R}_0$ and $\mathbf{R}_1$ are fixed. End points can in principle also be set free however this might lead to development of a system into a new state. Points between terminal points are then geometrically optimized. Total force acting on an image is the sum of spring along the tangent and true force perpendicular to it :

$$\mathbf{F}_i = \mathbf{F}_i^s|_{||} - \nabla E(\mathbf{R}_i)|_{\perp} \tag{3.81}$$

with the true force defined as

$$\nabla E(\mathbf{R}_i)|_{\perp} = \nabla E(\mathbf{R}_i) - \nabla E(\mathbf{R}_i) \cdot \hat{\tau}_i \tag{3.82}$$

where E is the energy of a system and $\hat{\tau}_i$ is the normalized local tangent at image i. Spring force is defined as

$$\mathbf{F}_i^s|_{||} = k(|\mathbf{R}_{i+1} - \mathbf{R}_i| - |\mathbf{R}_i - \mathbf{R}_{i-1}|)\hat{\tau}_i \tag{3.83}$$

with k being spring constant. An optimization algorithm is then used to move forces according to the force $\mathbf{F}_i$ from equation 3.81. Usual criteria of the convergence

is equalization of all the forces between images. This convergence mechanism however strongly favors overall smoothness of the MEP and this can sometimes cause the algorithm to miss the actual saddle point. A small fix called climbing image (CI - CI-NEB) is then applied to the algorithm. This approach retains general form of MEP but adds extra term to improve convergence towards saddle point. CI works by identifying image (i_{max}) with the highest energy. Force acting on this image is then replaced with

$$\mathbf{F}_{i_{max}} = -\nabla E(\mathbf{R}_{i_{max}}) + 2\nabla E(\mathbf{R}_{i_{max}}) \cdot \hat{\tau}^2_{i_{max}} \tag{3.84}$$

This is actually full force due to the potential with the component along the elastic band inverted meaning that the maximum energy image is not affected by spring forces at all. Consequently CI moves the image up the potential energy surface along the reaction path and down the perpendicular direction. Addition of CI does not make computations any more difficult, however total computational time might extend because of newer restrains caused by unrestricted image. Removal of forces acting on CI means that the spacing around the saddle point might become uneven. But since the saddle point is usually most interesting domain of MEP it would be reasonable to have more accuracy in this region. Simple solution would be to increase number of images which would come at the cost of additional computational power required. Another solution to the problem is to vary spring forces around the saddle point, i.e. spring constant increases near saddle point. Again many approaches can be used to change spring forces but normally they are weighted with the total energy of images, i.e. images with lower energy are connected by springs with lower coefficients.

3.5 Results representation

Visualizations of silica atomic structure and particular defects have been created using VMD [135] and Xcrysden [136] softwares. Plots of molecular orbitals are represented as contributions of selected wavefunction(s) to the (pseudo-)charge density. For norm-conserving PPs this is actually square of wave-function $|\psi|^2$, which is basically expectation value of particular wave function.

Results for Density Of States (DOS) from both DFT and GW approach, projected-DOS (PDOS), and optical spectra result produce a single line (delta function) for each state or optical excitation. In order to plot meaningful spectra these peaks have been artificially broadened using Lorentzian function.

3.6 Confocal Micro Luminescence

Photoluminescence (PL) is a phenomenon when light is irradiated from any form of solid material after some kind of excitation (usually photon or thermal). Some defects in silica are PL active so this phenomena can be used as a tool for studying these defects. Incident light promotes electrons into higher state followed by a relaxation into ground state. Decay is usually delayed by some time (life-time of excited state) and the energy of emitted photons is usually smaller than energy of incident light (reduction of energy is called Stokes shift while anti-Stokes shift is characterized by higher emission energy).

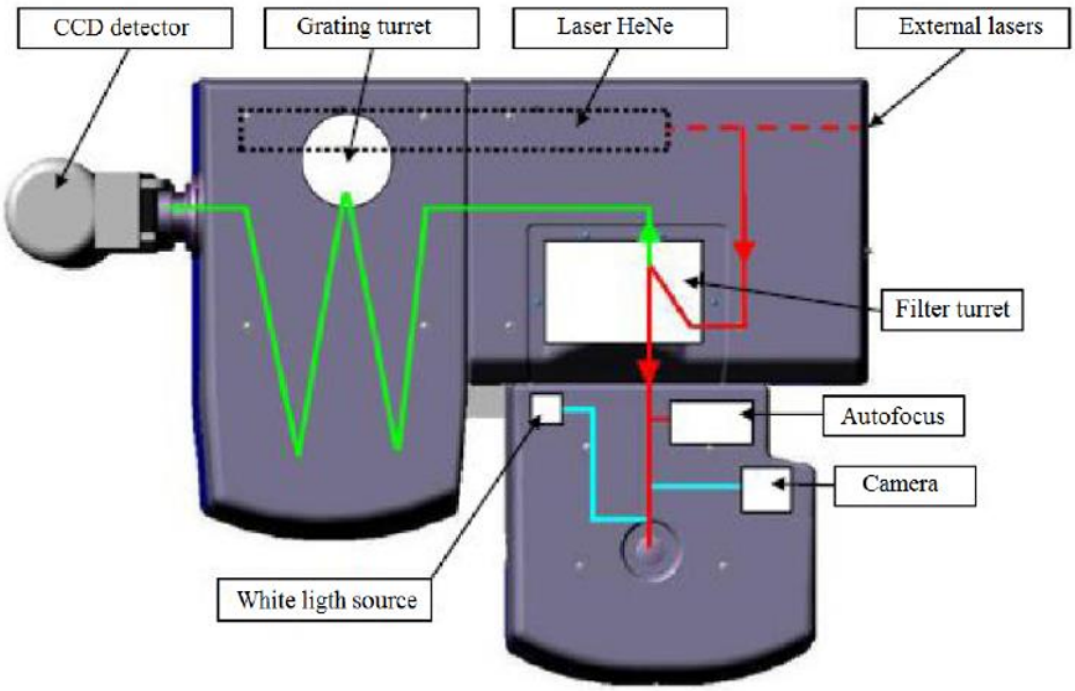

FIGURE 3.5 – Schematic representation of Aramis instrument with red line indicating incident light and green line emitted light. Adapted from [113].

Photoluminescence measurements have been performed using LabRam Aramis instrument, which is an integrated confocal micro-photoluminescence (CML) system. Figure 3.5 schematically shows operational principle of instrument. System is equipped with three lasers providing light at four excitation energies : HeNe 633 nm (1.96 eV), Ar+ 488 nm (2.54 eV) and HeCd providing 442 nm (2.81 eV) and 325 nm (3.82 eV).

Focusing can be adjusted by changing the objectives (UV-40x, 10x, 50x and 100x) which results in beam size of below 10 µm. X,Y and Z coordinates of the samples can be changed because samples were mounted on translational stage with micrometric precision. Fibers were cleaved and placed in line with the incident

light allowing the analysis of the fibers cross section. This experimental setup allows spectral resolution up to 0.5 nm for PL measurements.

3.7 Radiation Induced Attenuation and optical absorption measurements

Optical absorption usually denotes interaction of light with energy in vicinity of visible light (order of few electron volts). Photons can only be absorbed when their energy is equal or greater than the energy difference between highest occupied and lowest unoccupied state. In the case of semiconductors this usually refers to valence-conduction band gap, however inclusion of defect can introduce the additional states within the band gap thus lowering the energy needed for absorption.

On-line Radiation induced attenuation (RIA) is a technique that evaluates the losses of transmitted light during irradiation in real time. This experiment requires that an optical fiber is connected to a light source and spectrometer while being irradiated. Time evolution of induced losses is determined relatively to the reference transmitted spectrum. Multiple fibers are generally measured simultaneously to ensure identical irradiation conditions. Figure 3.6 shows schematic representation of RIA experiment with two fibers being irradiated simultaneously. Absorption coefficient, which actually describes radiation induced attenuation, is calculated as :

$$\alpha(D,\lambda) = -\frac{10}{l}\log\left[\frac{I(D,\lambda) - I_{\mathrm{bg}}(\lambda)}{I_{\mathrm{ls}}(\lambda) - I_{\mathrm{bg}}(\lambda)}\right] \tag{3.85}$$

Where l is the length of irradiated sample, $I(D,\lambda)$ intensity of light passing through fiber at given dose and wavelength, $I_{\mathrm{ls}}(\lambda)$ reference intensity of light source at certain wavelength and $I_{\mathrm{bg}}(\lambda)$ background intensity, which is always subtracted from results. This method compares absorbed intensity with reference intensity at given wavelength therefore eliminating the response of detector.

Experiments have been performed using Deuterium-Halogen DH 2000 light source (Ocean Optics) and two spectrometers working in visible/UV spectral domain (HR4000 and HR 2000 by Ocean Optics, spectral resolution above 1 nm). Irradiated lengths of the samples were between 5 cm and 15 cm. Optical fibers were placed on a heater plate with adjustable temperature between 25 and 280 °C (±4 °C at room temperature and ±1 °C at higher temperatures).

Samples were irradiated using MOPERIX X-ray tube with tungsten target operating at 100 kV. Samples were placed between 20 and 30 cm from the x-ray source which resulted in silica absorbed dose rate of approximately 4 Gy(SiO_2)/s. Fibers have been irradiated for two hours which nets to total absorbed dose of 30

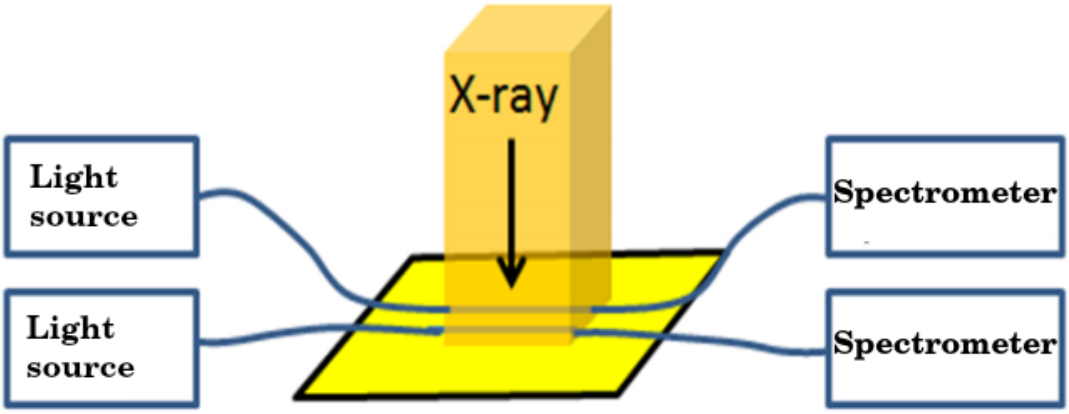

FIGURE 3.6 – Schematic representation of Radiation induced attenuation experiment. Adapted from [113]

kGy.

All of RIA experiments have been performed using standard procedure consisting of measuring noise and reference signals at room temperature followed by an increase of temperature to approximately 300 °C after which the noise and reference spectra of light source have been measured again. After these preparatory steps the X-ray source has been turned on for two hours. With irradiation switched off, noise and spectra of light source have been measured again after which the heating plate was turned off while the optical transition has been measured constantly until the temperature dropped bellow 50 °C.

3.8 Oxygen loading of fibers

Optical fibers of interest have been loaded with oxygen using high temperature and pressure loading treatment [113]. Fibers have been striped of polymer coating and placed inside 250 ml high pressure vessel. After sealing the container oxygen atmosphere has been established by means of venting with high purity technical oxygen gas (impurities < 5 ppm/mol) followed by a gradual increase of temperature to 500 °C. Final pressure of oxygen in the vessel was around 150 bar. Loading procedure lasted for 21 days maintaining constant high pressure/purity oxygen atmosphere. Thermal treatment conditions have been chosen to maximize the quantity of loaded oxygen. Using Raman spectroscopy it has been shown that the loaded concentration is uniform across the diameter of a fiber [113].

Table 3.1 – Chemical compositions of the core zones of analyzed fibers with drawing conditions.

Fiber	Inner core (wt%)	Outer core (wt%)	Drawing speed (m/min)	Drawing tension (g)
GeD3	Ge 8.6	Ge 4.6	70	135
SiD1	F 0.4	Pure Si	55	80
PD1	P 7.6	P 3.0	22	30
PCe	P 12.6, Ce 1.4	P 12.6, Ce 0.7	15	27
GeCeD3	Ge 4.4, Ce 3.9	Ge 4.4, Ce 2.0	17	30

3.9 Optical fibers

All of the fibers, except Fujikura RRMMA fiber, have been produced by iXBlue Photonics [137]. Samples produced by iXBlue Photonics, referred to as canonical samples, have been produced to represent current commercials fibers and to serve as a basis for development of new generation of OFs that might be employed into more advanced applications. Core diameter of all fibers is $\sim$ 62 µm. Beside pure silica fibers a number of doped and rare-earth co-doped fibers have been studied. These include germanium/phosphorous doped fibers, some of which have been also co-doped with cerium.

Properties of canonical samples fibers are summarized in table 3.1. This table however does not include Fujikura RRMMA fiber (which is a commercial fiber) because its manufacturing conditions and dopants concentrations are not known.

4. Results and Discussion

4.1 Intrinsic oxygen excess defects

Oxygen-excess-related defects are a class of defects that includes diamagnetic precursors such as O_2 and O_3 molecules, peroxy bridges and ozonyl bridges. Because of the well known high barrier for the penetration of oxygen through an oxidized surface, and in particular, of SiO_2, such defects have only been studied marginally. However, recent advances in oxygen-loaded optical fibers tends to indicate that this treatment increases radiation resistance [120, 117] which could lay foundation for a broad range of potential applications. Beside the application potential, the mechanisms for oxygen exchange between the SiO_2 network and dissolved gas molecules are still poorly understood.

This chapter presents results obtained by theoretical studies on oxygen excess defects. Whenever possible, the calculations are compared to available experimental observations. The results include structural, electronic and optical characterizations as well as a series of potential reactions with their corresponding reaction path and activation energy.

The first section is devoted to clarify why peroxy bridges, defects which are expected to be one of the major diamagnetic oxygen-excess related defects, have not been straightforwardly observed through their optical signature. The second section is focused on the characterization of ozonyl bridges. Finally, several possible reactions between oxygen and the silica network are explored, including reaction with oxygen deficient centers.

Structural and energy results are computed at the level of Density Functional Theory. For the electronic structure, DFT is compared to the more advanced GW calculations. Optical absorption is calculated within Many-Body Perturbation theory by solving the Bethe-Salpeter equation. Reaction path and barriers are obtained combining NEB with DFT energy and forces.

4.1.1 Creation of model and defects

The amorphous SiO_2 model has been generated from a standard melting and quenching of a 108-atoms crystalline SiO_2 model using classical molecular dynamics, see Ref. [51] for the generation details. In this way a random network of perfectly coordinated SiO_4 tetrahedra has been obtained. A further DFT-LDA relaxation is performed for obtaining first-principles relaxed angles and bond-

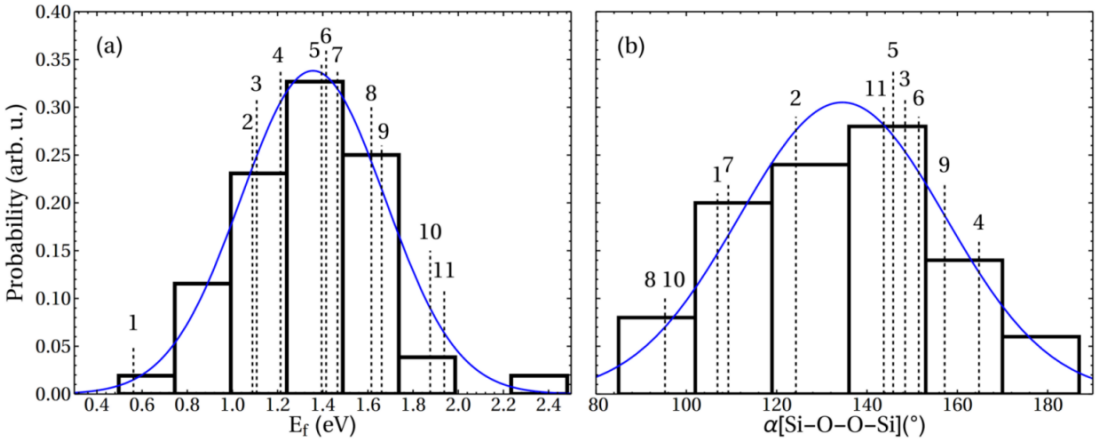

FIGURE 4.1 – Formation energy (E_f) and dihedral angle (α[Si–O–O–Si]) distributions, respectively subfigures a) and b). Numbered vertical lines indicate the E_f and α[Si–O–O–Si]) of the 11 selected configurations for the calculation of electronic and optical properties at the GW-BSE level.

lenghts. Comparison with larger models (192 and 648 atoms) shows that 108 atoms (36 silicon and 72 oxygen atoms) unit cell properly describes both local structure (bond lengths and angles) and macroscopic properties (density, dielectric constant) [51, 138, 28].

Defect models were created with the manual insertion of atoms or molecules into bonds or cavities with a further full-first principles relaxation. Because of the disorder, all site-related properties are distributed, leading to 72 non-equivalent sites for peroxy bridges or ozonyl bridges and a large number of non-equivalent cavities for molecular species.

4.1.2 Peroxy link defect

Structure and formation energies

After the relaxation of the 72 POL configurations their respective formation energies have been calculated as total energy differences, assuming an equilibrium with an O_2 gas reservoir :

$$E_f^{pol} = E_{SiO_2}^{pol} - E_{SiO_2} - \frac{1}{2}E_{O_2} \tag{4.1}$$

Where $E_{SiO_2}^{pol}$ is total energy of a cell containing pol defect, $-E_{SiO_2}$ total energy of a cell without the defect and E_{O_2} total energy of isolated oxygen molecule in its triplet ground state.

Due to the site-to-site disorder, formation energies are normally distributed (see figure 4.1 a), with values ranging from 0.56 eV to 2.30 eV and a mean of 1.36 ($\pm$ 0.32) eV. Lowest formation energy configuration (E_f=0.56 eV) is particularly

Table 4.1 – O–O distance d(O–O) and dihedral angle α(Si–O–O–Si) averaged over all 72 POL configurations. For comparison, the d(O–O) and α(Si–O–O–Si) of the lowest formation energy configuration are also shown.

	d(O–O) (Å)	α(Si–O–O–Si) (°)
Mean	1.49(0.01)	134.5(23.1)
lowest E_f	1.495	106.9

important as it represents ideal peroxy link defect in thermodynamical equilibrium. The geometrical parameters are also normally distributed (see table 4.1 and figure 4.1 b) : –O–O– distance varies between 1.47 Å and 1.52 Å with a mean value of 1.49(±0.01) Å, while the Si–O–O–Si dihedral angle takes values ranging from 90° to 180° with a mean value of 134.5 (±23.1)°. Obtained results agree well with previous works [48, 27, 49, 54, 107, 98, 99]. Vertical lines in figure 4.1 represent configurations that were selected for the further calculation of electronic and optical properties.

Electronic structure

Theoretical interpretation of electronic structure in amorphous semiconductors or insulators is based on pioneering ideas of Anderson, Mott and Cohen [139, 140, 141, 142]. It could be supposed that the opening of a-SiO_2 gap originates in extreme localization of band-edge states, with the subsequent observation of Urbach tails in optical absorption (OA). Structural disorder induces different degrees of electronic localization through the bias of ion-electron potential-well disorder which affects hybridization of the orbitals.

Network-related localization near the valence band (VB) edge has only been indirectly observed through the measurement of Self-trapped Holes (STH) [143] Besides strong localization at band edges, two effects are, however, compensating each other : the disorder and the atomic density. Indeed it is well known that in tetrahedric systems the gap increases with the density, hence a-SiO_2 should exhibit a gap that is smaller than quartz because of its lower density [138]. On the other side, disorder opens mobility gap which is expected to be larger than the gap of the crystalline counterpart. These two effects result in a silica mobility gap and electronic structure that is very similar to quartz [138].

In the case of a-SiO_2, as the Bottom of the Conduction Band (BCB) is governed by O 3s orbitals and the disorder strongly affects only bond angles, the spherical symmetry of s orbitals precludes any significant localization at BCB edges (excluding point-defect-related bands). The Top of the Valence Band (TVB) is more sensitive to disorder in SiO_2 as it is controlled by non-bonding O 2p (with

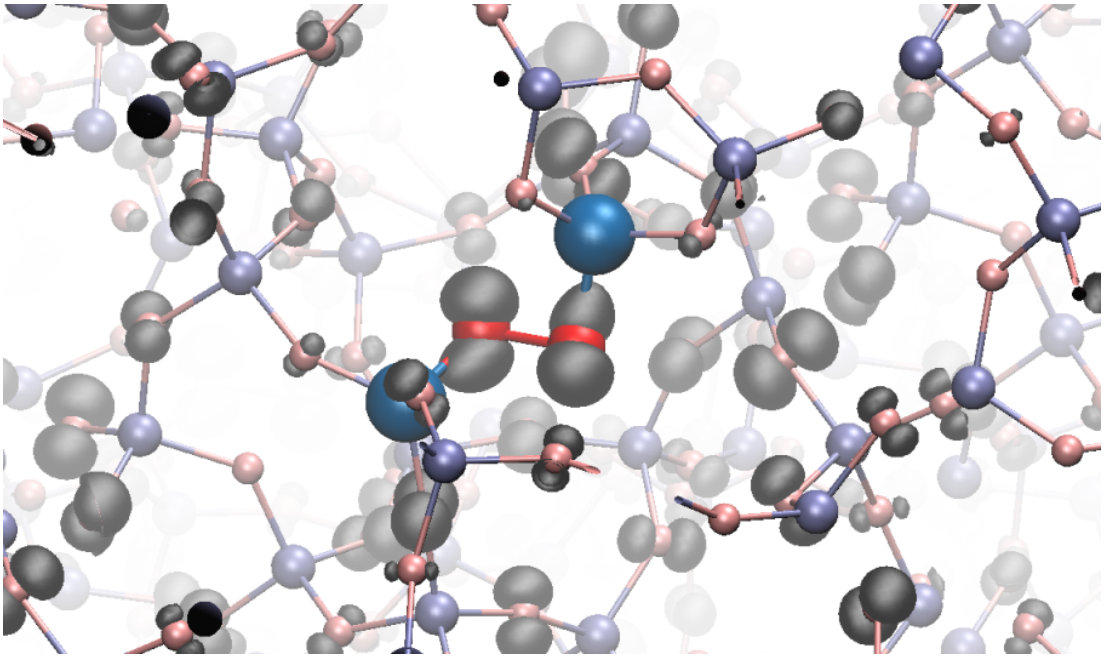

FIGURE 4.2 – Incorporation of HOMO-1 into delocalized state near TBV. Similar states dominate electronic structure near TVB. Si and O atoms are represented in blue and red, respectively. Two Si and two O atoms forming peroxy bridge are highlighted.

angular dependency).

Oxygen electronic states of peroxy link around the band gap of silica are two full and one empty 2p orbitals (p_x, p_y occupied and empty p_z). Plots of the electronic states calculated at DFT level are shown in the figures 4.3 and 4.2. Figure 4.3 shows defect states (a,b,c) and BCB (d). Two occupied states form weak π^* (a,b) while the strong repulsion of p_z pushes σ^* (c) inside the band gap. Part (d) of figure 4.3 shows that BCB is controlled by oxygen 3s orbitals, [28]. DFT approach, which is known to underestimate the wide gap of insulators, calculates the gap to be around 5 eV. This electronic configuration in surprisingly similar to results of first POL theoretical study [47] based on tight binding approach (with an obvious difference in energies).

Since peroxy-related orbitals are strongly localized and are of the same nature as the HOMO and LUMO orbitals in the H_2O_2 case, see figure 4.3 and 4.4, the terminology HOMO-1 (a), HOMO (b) and LUMO (c) typical for molecules can also be used for labeling POL π^* and σ^* orbitals [144].

Detailed analysis has revealed that there exist two characteristic behaviors of POL induced defect states. This is shown by projecting the Density Of electronic States (PDOS) on atomic orbitals. Figure 4.5 shows the DFT PDOS on the atomic oxygen 2p orbitals for two identified POL prototypical configurations. In the first situation (case 1), two occupied defect states can be easily distinguished, while

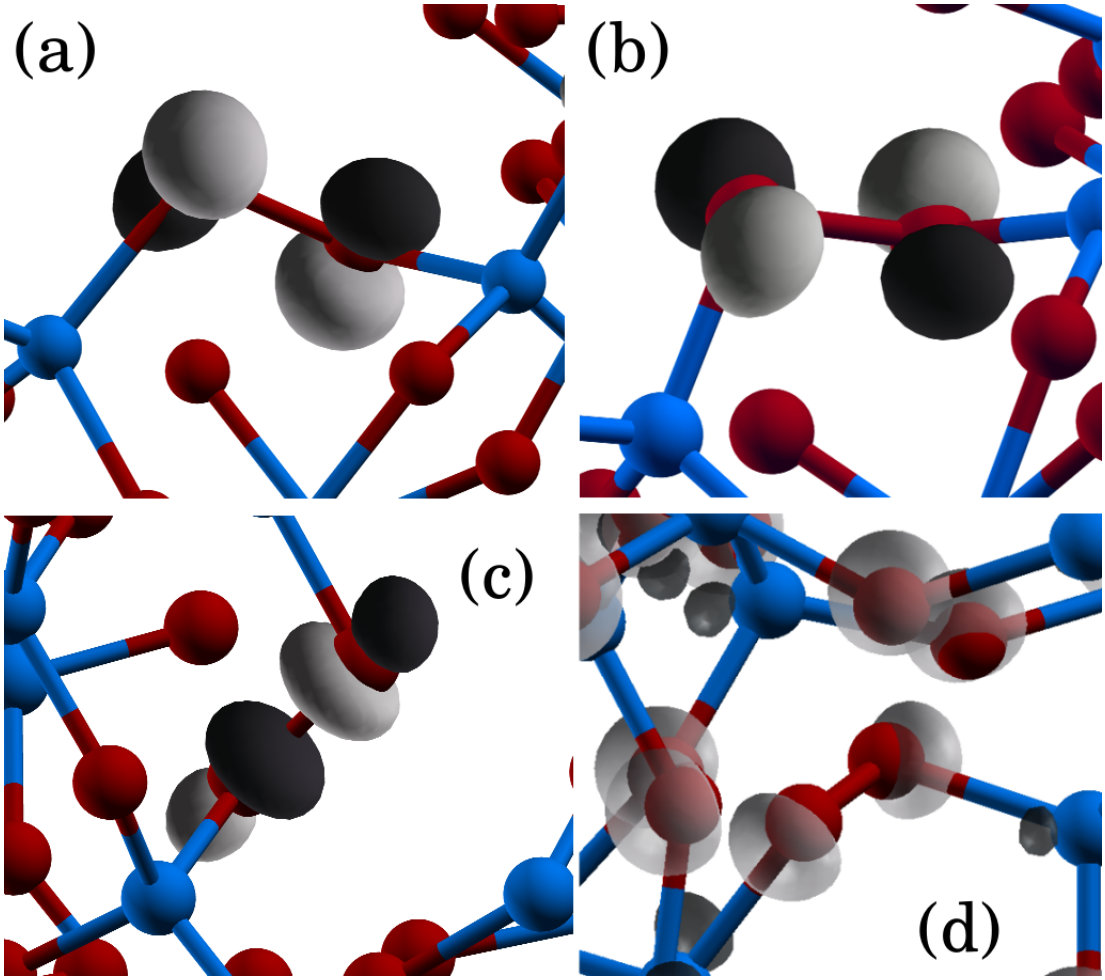

FIGURE 4.3 – Defect electronic states for the prototypical situation where two occupied defect states can be seen : HOMO-1 (a) and HOMO (b) π^* pair σ^* LUMO (c) and BCB (d). Si and O atoms are represented in blue and red, respectively. Light and dark gray represent the + and - sign of the wave function respectively.

in the second one (case 2), only higher of the two occupied defect states is still visible. Energy of the lower state decreased, which allowed its entanglement with the Top of the Valence Band (TVB) so it can no longer be distinguished on the spectra. This can be seen in figure 4.2, where defect state is entangled with valence band. While visualization of this state provides some qualitative representativity, p-state projection must be used to qualitatively identify particular states within the band.

Because of high computational costs of GW method, the initial set of 72 configurations has been reduced to just 11 that were selected to sample the formation energy and dihedral angle distributions. Vertical lines on figure 4.1 mark the angles and formation energies of sampling set. Mean mobility gap of 9.4($\pm$0.06) eV calculated at the GW level has been found to agree well with the measured photo conductivity threshold in silica [145]. This agreement validates the theoretical approach and selected 108-atom model, which appears to be

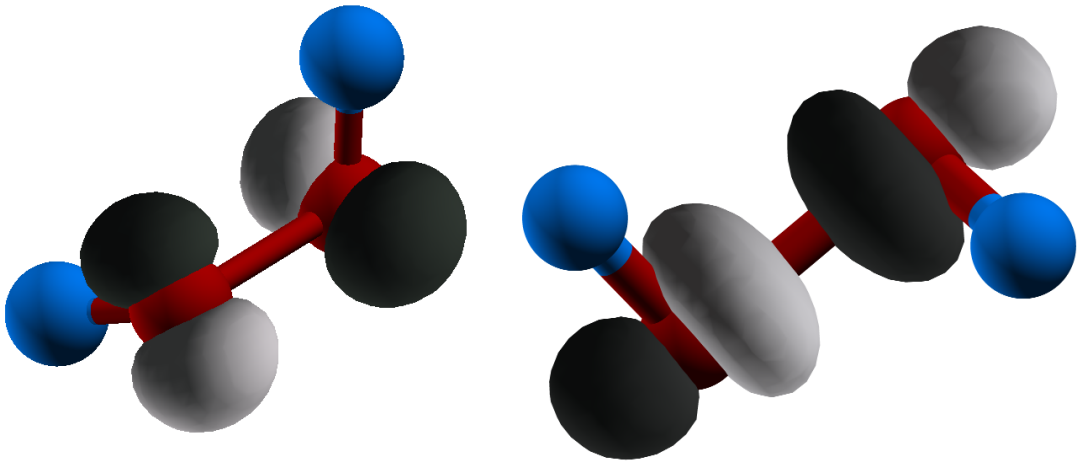

FIGURE 4.4 – Right : Highest occupied (HOMO), Left : lowest unoccupied (LUMO) molecular orbitals of H_2O_2 molecule form π^* and σ^* bonds, which closely resemble states in POL defect. H and O atoms are represented in blue and red, respectively. Light and dark gray represent the + and - sign of the wave function respectively.

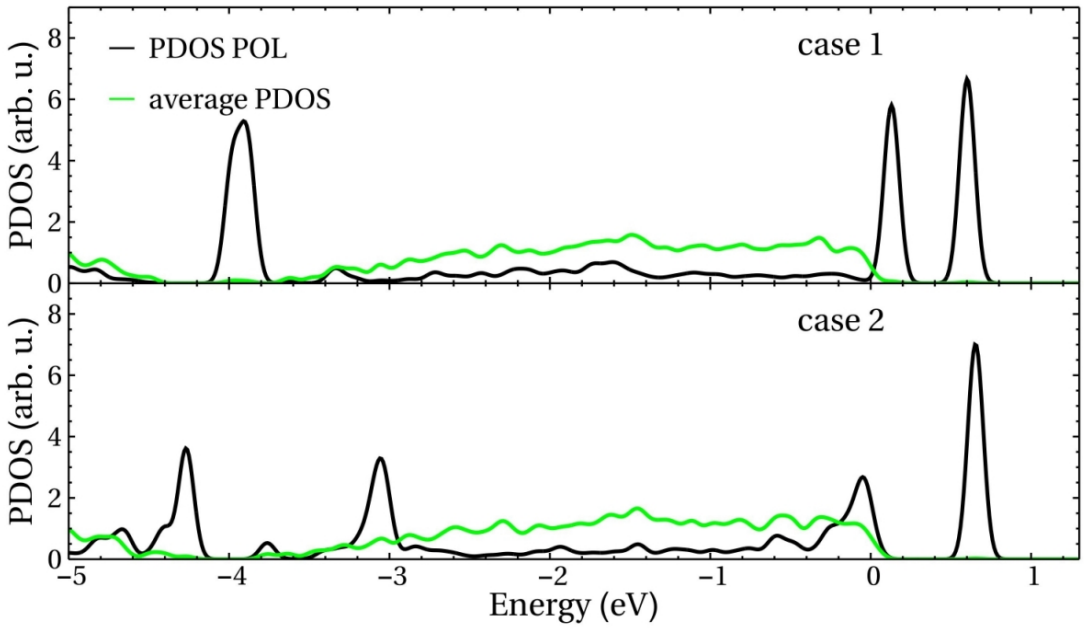

FIGURE 4.5 – Projected DOS for two prototypical behaviors (case 1 and case 2). Green line shows average PDOS on non-defective atoms while black line is the PDOS on the two oxygens involved in the POL. Artificial broadening of 0.07 eV has been used.

large enough to properly describe the POL low-concentration limit (negligible defect-defect interaction).

The insertion of a POL defect did not change the dielectric properties of the matrix (position of TVB and BCB does not change with the presence of defect). Table 4.2 summarizes the defect level energy positions with respect to the TVB for two prototypical situations. In the case when both occupied defect states

Table 4.2 – Average GW energy positions, with respect to the TVB, of defect levels induced by the presence of POL. The two situations, where HOMO-1 is disentangled (case 1) or entangled (case 2) with TVB states, are given separately. All units are in eV.

	HOMO-1	HOMO	LUMO
case 1	0.16(0.07)	0.41(0.18)	10.58(0.23)
case 2	-	0.73(0.20)	10.40(0.18)

are distinguishable (case 1), the lower defect state (HOMO-1) is, on average, at 0.16($\pm$0.07) eV above TVB while the highest occupied state (HOMO) is at 0.41($\pm$0.18) eV. The lowest unoccupied defect state (LUMO) is on average found at 10.58($\pm$0.23) eV above the top of valence band. When HOMO-1 cannot be easily distinguished from the TVB (case 2), the energy of the HOMO seems to be on average slightly higher, at 0.73($\pm$0.20) eV above TVB. In this case average energy of LUMO is 10.40($\pm$0.18) eV. In all cases, the LUMO is approximately 1 eV above the BCB, similarly to what was found in Ref. [27], despite the differences in the level of theory and in the use of a 10-atoms SiO_2 cluster model passivated with hydrogen instead of a bulk model.

Optical properties

In the analysis of excitonic structure a distinction between the two prototypical cases has been preserved (see table 4.3 and figure 4.6). In general, the oscillator strengths are very low (between 10^{-3} and 10^{-4}) which is a direct effect of the small overlap between π^* (figure 4.3 a,b) and σ^* (figure 4.3 c) orbitals. Table 4.3 summarizes low energy excitons for two cases while figure 4.6 shows DOS and corresponding optical absorption.

In the first case (case 1) there are 5 excitons while the second case (case 2) only shows four excitons. Previously described lower state hybridization with the valence band reduces a number of possible transitions as it is now impossible to distinguish excitations coming from "pure" valence states and defect-valence hybridized state. This phenomena strongly affects optical properties of POL. Analysis can also be separated in two spectral regions : low energy excitations with energies covering visible/UV domain from 3.0 to 6 eV (table 4.3 A, B, A', B') and high energy excitations that occupy the high UV region from 6 up to 8.0 eV (C, D, E, C', D'). Low energy excitations are mainly transitions between occupied (with the contribution of hybridized defect-TVB state in case 2) and unoccupied defect states.

Larger energy dispersion is caused by geometry changing the relative energy

Table 4.3 – Excitation energies and oscillator strengths of optical excitations ascribed to the presence of POL, when the two occupied defect states (HOMO-1 and HOMO) are distinguishable (case 1) and when the lower state (HOMO-1) is hybridized with TVB (case 2). The columns "From/To" and "Weight" provide the main single-particle states involved in a given excitation and their corresponding weight (weight of a given single-particle to single-particle transition contributing to the two-particle excitonic wave function), respectively. Numbers in parenthesis are standard deviations. Notation used is equal to figure 4.6.

Ind	Energy (eV)	Osc. Str. (10^{-3})	From	To	Weight
Case 1					
A	3.8 (0.2)	1.9 (1.4)	HOMO	LUMO	0.74 (0.19)
B	4.2 (0.6)	3.0 (1.6)	HOMO-1	LUMO	0.65 (0.14)
C	7.3 (0.2)	0.7 (0.7)	HOMO	BCB	0.92 (0.01)
D	7.5 (0.1)	0.5 (0.4)	HOMO-1	BCB	0.92 (0.01)
E	7.6 (0.0)	0.5 (0.3)	TVB	BCB	0.79 (0.17)
Case 2					
A'	3.2 (0.1)	0.5 (0.4)	HOMO	LUMO	0.93(0.01)
B'	5.2 (0.4)	1.4 (1.0)	HOMO-1/TVB	LUMO	0.14 (0.05)
C'	7.0 (0.2)	2.8 (2.1)	HOMO	BCB	0.93 (0.01)
D'	7.6 (0.6)	5.1 (6.7)	HOMO-1/TVB	BCB	0.90 (0.04)

of the state, i.e. these configurations are affected more by structural disorder. On the other hand, high excitations show smaller energy broadening. Single-particle decomposition of high energy excitons shows that in the first case they originate from occupied defect states into the conduction band, while in the second case their origin is strongly influenced by the valence band. Specifically, this transition is not characterized by only two electronic states (excitation from occupied to empty state) but rather by transition of non-trivial valence band states combination to empty defect state. These series of single-particle transitions are mostly involving 2p and 3s states of TVB and BCB neighborhood and less the defect states, their individual probability for a single to single particle transition (weight) is very low. Combination of low individual weights, which reduce the contribution from dispersed defect state, in combination with the previously described stability of valence/conduction states, with respect to the geometry, explains why defect states have virtually no effect on the high energy excitons. In other words, these excitations are barely influenced by POL site-to-site disorder. Another interesting notation can be seen from oscillator strength as it appears that in the first case oscillator strengths are stronger for defect→defect state transitions while in the second case probabilities are higher for transitions into the conduction (the dispersion in sampling set is also greater).

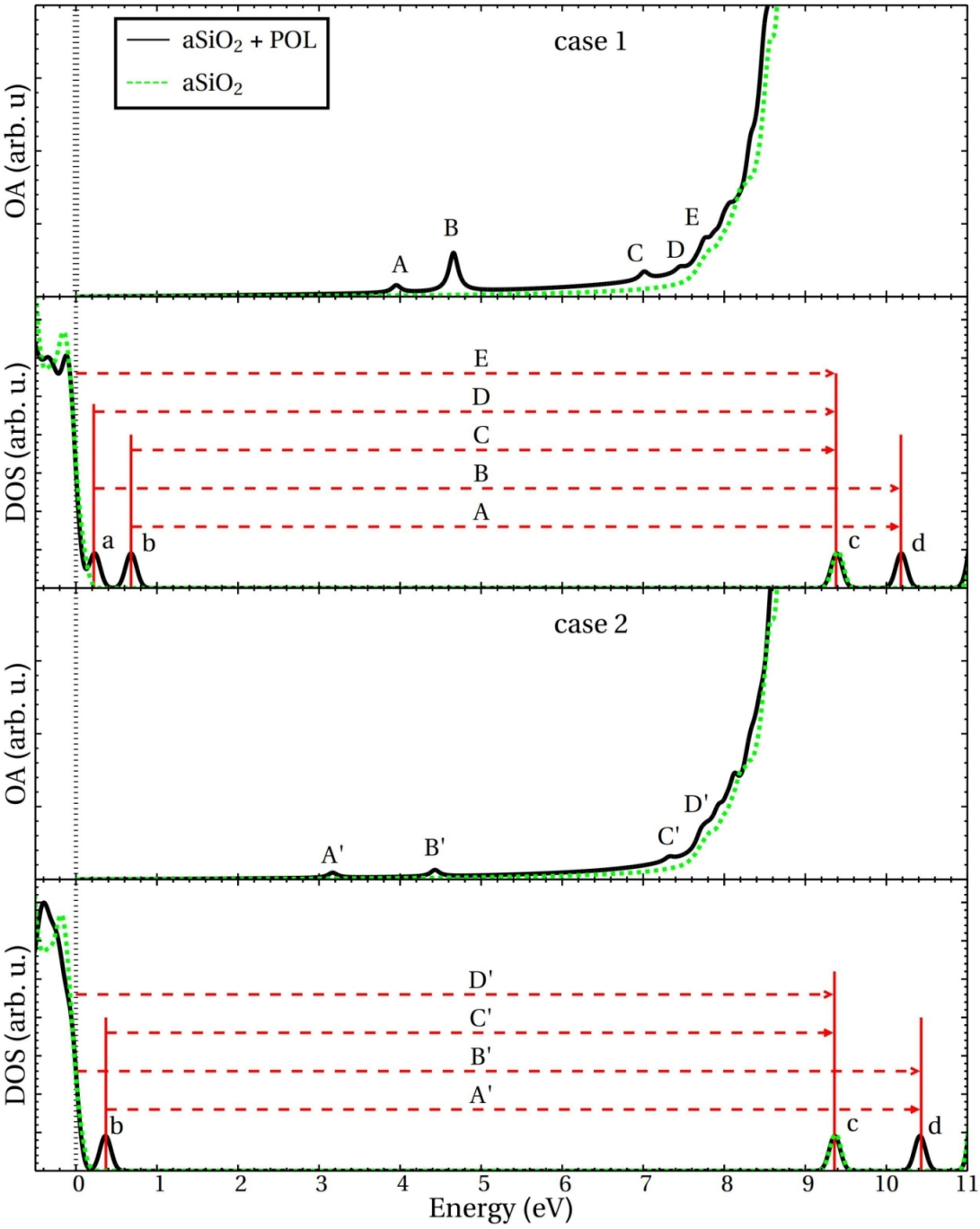

FIGURE 4.6 – DOS (at the GW level) and optical absorption spectra (OA) of two prototypical situations (case 1 and case 2). Vertical dashed line at 0 eV marks TVB. Uppercase letters label excitation peaks (A, B, C, D, E for case 1, A',B',C',D' for case 2) while lowercase letters label single-particle electronic state energies (a-HOMO-1, b-HOMO, c-BCB, d-LUMO). Red arrows underline the main single-particle transition contributing to a given excitation in the OA. An artificial broadening of 0.07 eV has been used for both DOS and OA.

Mean optical absorption spectrum has been calculated as an average of all 11 individual excitation energies and oscillator strengths and is shown in figure 4.7. It also shows why the optical signature of POL has never been clearly assigned. The

Table 4.4 – Optical excitations of POL configuration with the lowest formation energy. Same notation as in figure 4.6 is used. From/To describes which states/bands are mainly involved in the transition together with its corresponding weight.

Ind.	Energy	$f(10^{-3})$	From	To	Weight
A	3.95 eV	0.9	HOMO	LUMO	0.935
B	4.65 eV	5.0	HOMO-1	LUMO	0.845
C	7.00 eV	0.9	HOMO	BCB	0.922
D	7.45 eV	0.7	HOMO-1	BCB.	0.918
E	7.67 eV	0.2	TVB	BCB	0.922

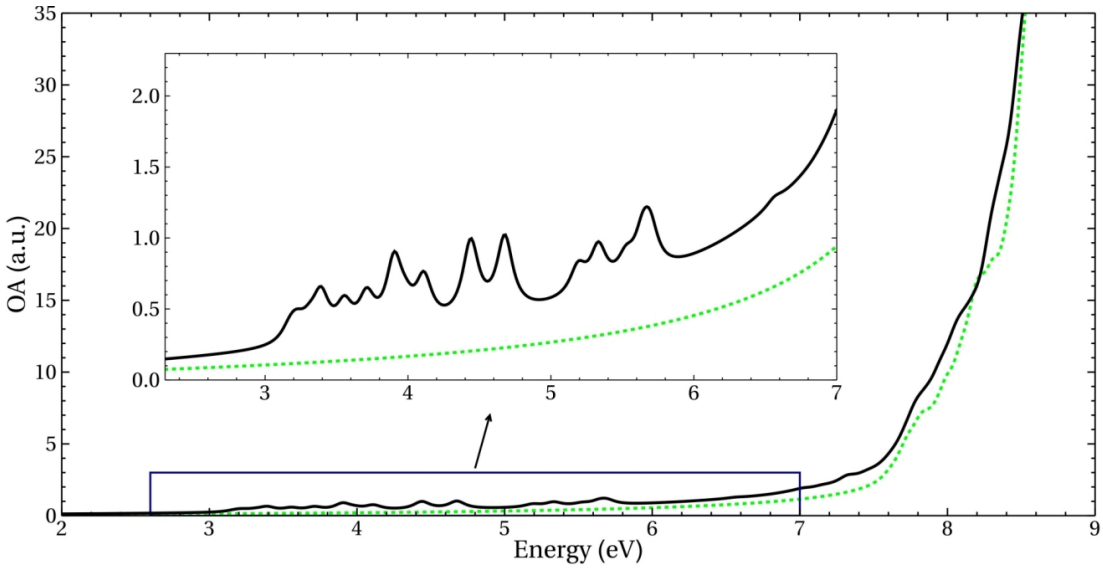

Figure 4.7 – Mean optical absorption spectra (OA) of all calculated configurations is represented by black line while dashed green line represents optical absorption of undefective silica model. Inset shows a zoom of the spectrum between 2.5 and 7 eV.

overall low oscillator strength in combination with the high energy dispersion that spans an energy range between 3.0 and 8.0 eV, make the POL optical contribution very low. As this spectral range is in real oxygen rich samples already populated by other, optically more active defects, the contribution from POL would very easily be hidden by other defects.

Correlations between structure and optics of POL defect

The presence of POL induces small distortions to the silica matrix and gives rise to strongly localized electronic defect states (no additional Anderson localization is induced at the silica network level). Within these premises, it would be expected that POL exhibits well-identifiable absorption peaks. However, contrary to the

case of other point defects like the oxygen vacancies [28], the energy dispersion of the low-lying excitations is very broad. Two questions arise from the results : why does the site-to-site disorder impact OA so strongly and would it be possible to find an explanation of this behavior.

Inspired by older studies of Pacchioni [27, 48] the H_2O_2 molecule has also been used as a simplest POL model to understand the relation between local-geometry, in particular, the dihedral angle and its electronic properties. It should be noted that the reference study was performed approximately 20 years ago when available computational power was much lower and the use of oversimplified models was the only modeling option. The strong influence of the dihedral angle on many electronic properties of H_2O_2 is known since many decades (see for instance [146]) but, according to available literature, this relationship has never been exploited in the context of POL.

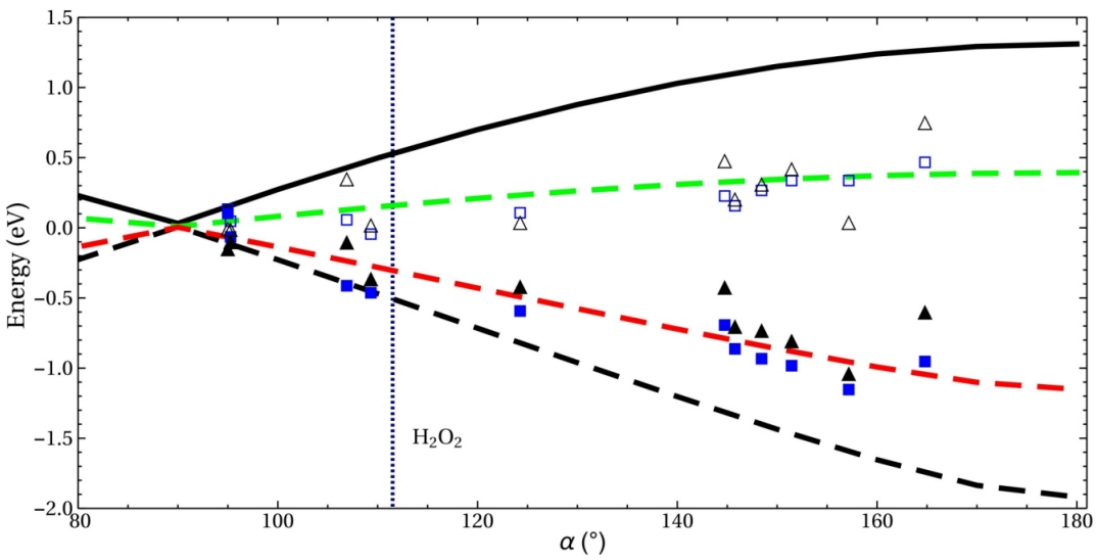

FIGURE 4.8 – Energy variation of HOMO and HOMO-1 as a function of the dihedral angle (α[Si-O-O-Si]). Dashed and continuous black lines represent the Kohn-Sham energies of HOMO-1 and HOMO of H_2O_2 molecule in vacuum. Blue squares represent HOMO-1 (filled squares) and HOMO (empty squares) Kohn-Sham energies of the two occupied POL defect states (for readability, we used only 20 different POL configurations from the calculated 72). Triangles indicate GW quasi-particle energies of HOMO-1 (filled) and HOMO (empty) of the two occupied POL defect states. Vertical dashed line shows the dihedral angle of the H_2O_2 molecule in gas phase. Dashed green and red lines are fits of the GW quasi-particle energies of the two occupied POL defects states.

A series of ground-state calculations have been performed at fixed geometry changing manually the H–O–O–H dihedral angle. Figure 4.8 shows the variation of HOMO-1 and HOMO energy positions with respect to the dihedral angle (σ^*-like LUMO is barely affected by the dihedral angle variations) for the H_2O_2 molecule

(black-dashed line and black line in figure 4.8, respectively). The relative minimum energy difference between HOMO-1 and HOMO occurs at 90° where both states are degenerate in energy and spatially orthogonal to each other. Increasing the angle rotates p_x and p_y orbitals towards each other which increases their overlap and consequently the energy difference up to 3 eV, which corresponds to a dihedral angle of 180°. When energy levels for each POL configuration are plotted as a function of their corresponding dihedral angle, as figure 4.8 shows for the case of HOMO and HOMO-1, it becomes clear that Si–O–O–Si dihedral angle distribution (shown in figure 4.1), which originates from the site-to-site disorder, is the key quantity that governs the electronic properties of POL.

In Si–O–O–Si the energy difference between HOMO and HOMO-1 reduces (red and green dashed lines of figure 4.8, which roughly follow results presented by squares for DFT and triangles for GW approach) with respect to the H_2O_2 molecule in vacuum (dashed and continuous black lines of figure 4.8) due to the interaction of electrons with the electron cloud of silica matrix. It is important to note that GW and DFT yield very similar relative energy positions of the occupied defect levels, validating the DFT total energy calculations. Site-to-site disorder again induces some fluctuation into the energy positions however such effects are relatively low and would require extremely accurate analysis to properly describe the fluctuations.

Defect state and its energy can be identified by PDOS even when it becomes entangled with broad valence states as shown in figure 4.5 so it is again used to find accurate energy positions for the cases in which HOMO-1 become entangled with the TVB. Results show that at 95° the two states (HOMO-1 and HOMO) are practically degenerate. When the angle increased to around 107°, the two states become clearly distinguishable. Interestingly this angle almost corresponds to the geometry of the lowest formation energy (106.9°) that is close to the H_2O_2 equilibrium dihedral angle (111.5°). At higher angles starting from approximately 140° HOMO-1 becomes strongly entangled with the TVB states.

This knowledge describing how electronic structure is affected by the site-to-site dihedral angle disorder can be used to better understand the energy dispersion of the low-lying optical excitations. In figure 4.9 the energy difference between the two lowest lying optical transitions (B–A or B'–A', see table 4.3 and figure 4.6) is plotted as a function of the dihedral angle and/or of the energy separation between HOMO-1 and HOMO for the eleven POL configurations.

For the dihedral angles, in which HOMO-1 is disentangled from TVB, energy differences between the excitons increase linearly with the HOMO and HOMO-1 energy separation. When the energy separation of two states becomes approximately 1 eV, which corresponds to dihedral angles of about 140°, the energy difference

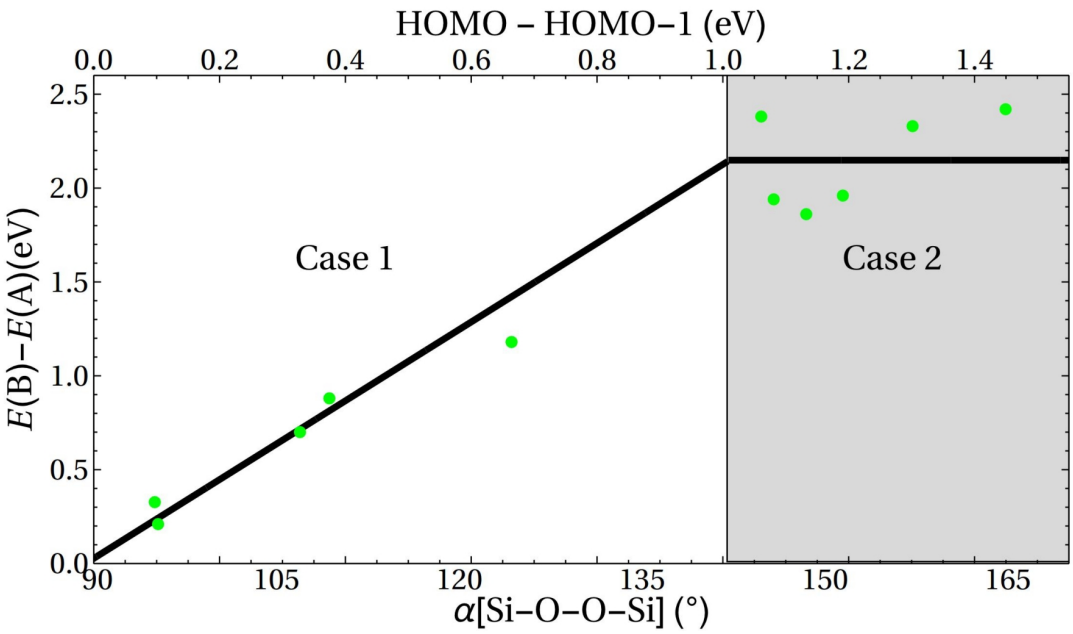

FIGURE 4.9 – Correlation between the α Si–O–O–Si dihedral angle (lower x-axis), energy difference of HOMO-HOMO-1 occupied defect states (upper x-axis) and difference between the two lowest excitation energies ($E(\mathrm{B}) - E(\mathrm{A})$).

of the lowest lying excitons reaches a mean value of 2.1 eV and stays constant even at higher energies (higher dihedral angles). In other words, the excitation energy becomes independent of the HOMO and HOMO-1 energy difference (independent of the dihedral angle). This can be understood by analyzing the single-particle state decomposition of the corresponding exciton B' in table 4.3. The contribution of HOMO-1 on B' is only of about 14% of the total single-particle decomposition, indicating that the exciton B' is mainly (86%) made up from different transitions involving TVB states. Consequently this implies that the specific energy position of HOMO-1 is no longer relevant.

Multiple peroxy configurations

Configurations containing multiple peroxy structures have also been considered, not for their electronic or optical properties but as possible candidates in oxygen exchange reactions. While insertion of two independent defects into 108 atoms cell used in this study greatly overestimates experimentally measured concentrations of defects [2, 21], presence of multiple peroxies positioned in relative vicinity can be expected following the dissociation of oxygen molecules, for example under irradiation.

Models containing multiple defects have been created by a manual insertion of extra oxygen atom in Si–O–Si bonds within the models already containing POL defect (as described and used in section 4.1.2) followed by a full relaxation

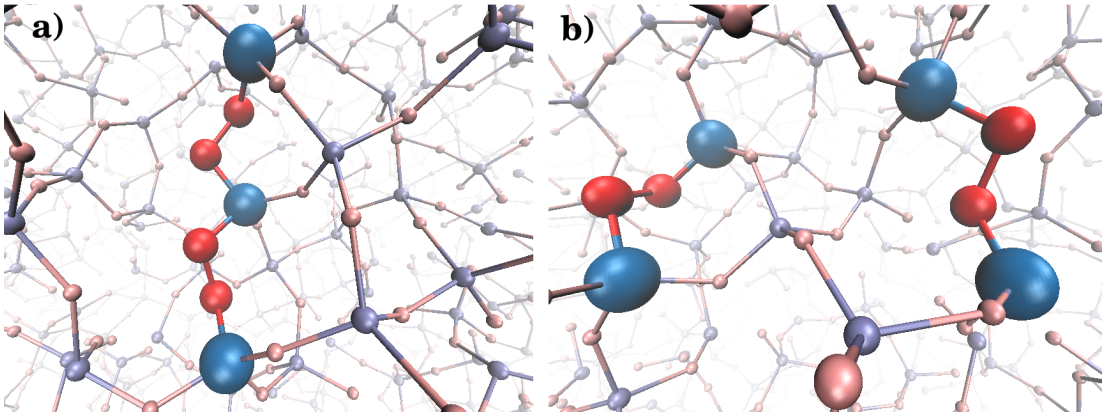

FIGURE 4.10 – Typical adjacent peroxy linkages (a) and non-adjacent defects (b).

of the atomic positions. Multiple peroxy configurations have been divided into two subgroups, namely adjacent and non-adjacent sites. Adjacent (neighboring) peroxies are separated by a single silicon atom while there are more than one silicon atoms between non-adjacent defects. Incorporations of second peroxy into the model, for both adjacent and non-adjacent sites, induced little bit more strain but didn't result in any significant distortion of the cell or any formation of different defects, which can be attributed to the great flexibility of the disordered silica network. Geometry of secondary peroxy bridges does also not deviate significantly compared to the single peroxy configurations as described in section 4.1.2 with mean dihedral angle around 135° and mean distance between defect atoms 1.5 Å.

Examples of both configurations can be seen in figure 4.10, where left image (a) shows typical adjacent configuration and (b) shows non-adjacent peroxy defects.

Formation energy has been calculated using standard formula 4.2 :

$$E_f = E_{2pol} - E_{SiO_2} - E_{O_2} \tag{4.2}$$

Formation energies are summarized in table 4.5. Results show combined formation energy ranges from 1.54 eV to 3.16 eV with mean value 2.53(±0.44) eV. When considering particular configurations, E_f of adjacent sites range from 1.81 to 3.25 eV with mean value 2.27(±0.42) eV. For non-adjacent sites formation energy is spread from 1.54 to 3.1 eV with average 2.66(±0.39) eV (this energy does not include contribution from defects separated by infinite distance as presented below). Non-adjacent peroxide defects surprisingly have, on average, 0.4 eV higher formation energy compared to adjacent defects. Comparison of formation energy with the single peroxy link defect (figure 4.1) shows there is small overlap between formation energies of two defects meaning both could coexist even in equilibrium conditions.

The lower energy of adjacent peroxies might show that there exist attractive

Table 4.5 – Two POL formation energy comparison

Arrangement of two POL defects	E_f (eV)
Adjacent	2.27 ± 0.42
Not-adjacent	2.66 ± 0.39
Combined	2.53 ± 0.44

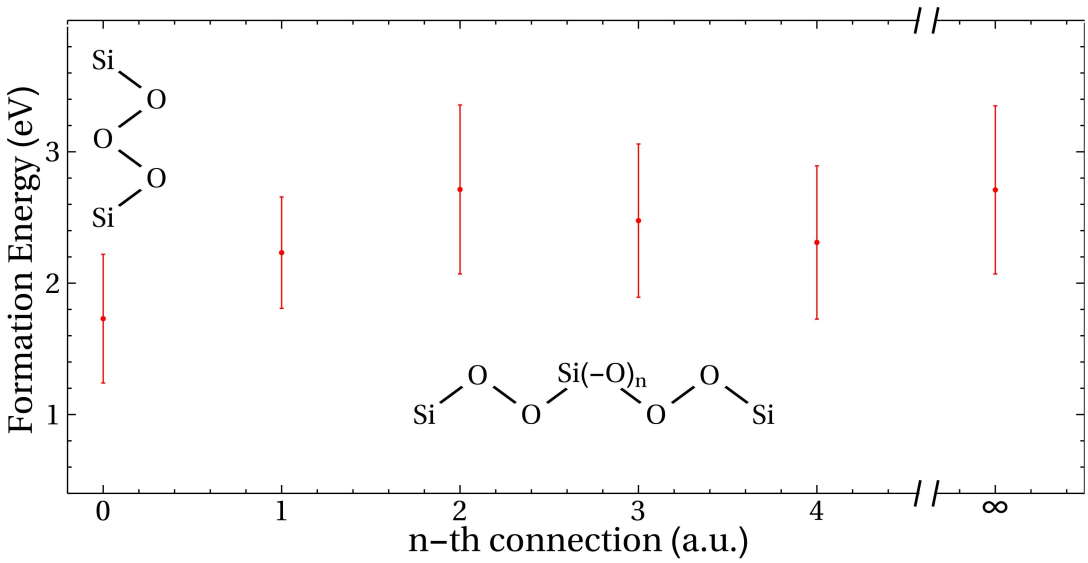

Figure 4.11 – Formation energy of two POL defects depending on number of non-defective sites between defects. Zero corresponds to no atom separating the POL, ie. ozonyl, 1 to adjacent POLs and so on. Values of single POL defect are used to describe "infinitely" separated POLs.

forces between defects. Indeed, defect clustering is a usual effect in many systems [147, 148].

Figure 4.11 shows variation of formation energy as a function of relative distance (in the terms of separating silicon atoms) for multiple peroxy defects. Zero corresponds to ozonyl (no Si-atoms separating two POLs), one to adjacent species (1 Si atom in between), two when there are two Si atoms (with linking oxygen atoms) and so on.

Results show that the formation energy of multiple POLs increases from 1.73(±0.49) eV for ozonyl to 2.66(±0.4) eV when two POLs are separated by a two non-defective sites. Formation energy decreases until 2.31(±0.58) eV which is the maximum separation the used model allows until distance becomes smaller than the periodic replica of said defect. E_f then starts increasing again as the distance between multiple POLs increases until in reaches 2.72(±0.64) eV when two peroxies become so far apart that there is no more any attractive or repulsive force (this is represented by double of formation energy and standard deviation for

single POL in the cell as presented in section 4.1.2 - while these configurations are not separated by infinite distance, there is no interaction between periodic replicas). According to results from [49] the POL defect incorporation strain decreases with the distance from site. Following this theory the formation energy should thus decrease with distance which is not the case. Reference study however describes only incorporation of a single defect. For multiple defects the behavior seems more complex as formation energy first increases for relatively nearby defects, then decreases as separation rises followed by another increase when possible interaction mechanisms between defects disappear. Combining present results with those of [49] it could be hypothesized that, in general two close defects behave as one and consequently induce less strain into network compared to two separate defects. The behavior at close distance is however not monotonous as the strain must first increase as two defects separate to explain the peak at 2.66 eV. The variations of formation energies are however within the error bars, which could also mean the fluctuations are caused be the structural disorder and there might not be any correlation between number of sites separating the defects and their respective formation energy. While in general there is no visible long range trend, short range fluctuations differences might be more important. In this scope creation of single defect has higher cost, as it requires distortion of the matrix while incorporation of subsequent defects has smaller effects of formation energy. It is important to note, that, in general, the absolute distance between defects is not directly linked with the number of "sites" between them, because "sites" is a topological label and does not define a metric.

Figure 4.12 shows formation energy of two peroxy bridges as a function of total distance between defects (measured from middle of O–O bond). Gray line represents least square fit while red point with error bar again represents formation energy of POL pair separated by infinite distance (double of single POL E_{f} as above). Fit basically shows that there is virtually no correlation between two quantities as represented by almost flat line. More importantly the error bar for configurations at infinite distance is greater that the data spread meaning that the structural disorder has stronger effect than any possible binding energy of neighboring defects. Within the perspective of inter-conversion mechanisms and diffusion, this later result indicates that jump directions would be un-correlated even when two defects are first-neighbors. In other words, POL clustering does not appear to be energetically favored.

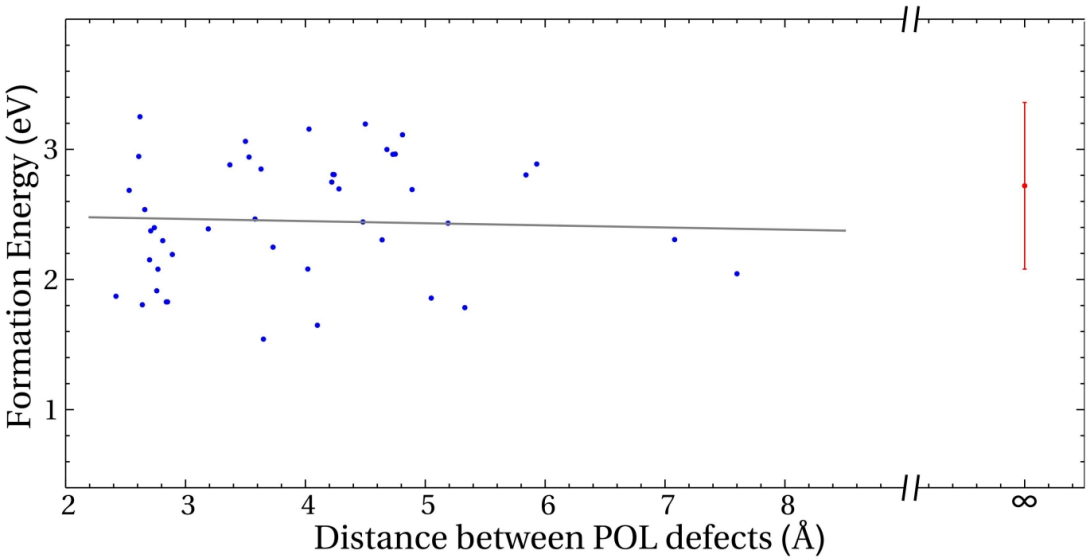

FIGURE 4.12 – Formation energy of two POL defects as a function of distance between defects. Red dot with error bar shows formation energy of single POL which represents two POLs separated by "infinite" distance (when there is no longer any interaction between periodic replicas of defects).

4.1.3 Ozonyl defect

Ozonyl was first proposed by [54] as an intermediate step for oxygen migration in α quartz. Authors proposed the migration model through the absorption of oxygen molecule forming interstitial ozone defect, also known as ozonyl, with the structure of Si–O–O–O–Si. In their model the formation energy of ozonyl is marginally lower compared to the peroxy linkage but more importantly this reaction does not require expensive dissociation of O–O bond (5.15 eV [5]). In his PhD Thesis T. Bakos [99] found that ozonyl is energetically favorable with respect to the gaseous O_2 molecule in amorphous silica. This finding is in direct disagreement with many experimental papers, that were able to detect presence of O_2 using its characteristic singlet→triplet PL band. On the other hand, ozonyl has never been directly detected by experiments (similarly to the POL). The simplest molecular model of ozonyl would be di-hydrogen trioxide (H–O–O–O–H), which is known to be stable at room temperature only under particular conditions [149, 150].

Creation and structure of ozonyl defect

In the case of ozonyl, not all the available precursor O sites were able to stabilize it. Indeed, in the case of oxygen sites belonging to three-fold rings (the smallest rings in silica), as locally the structure is denser, the insertion of two additional oxygen atoms sometimes created so much stress on the surrounding network that

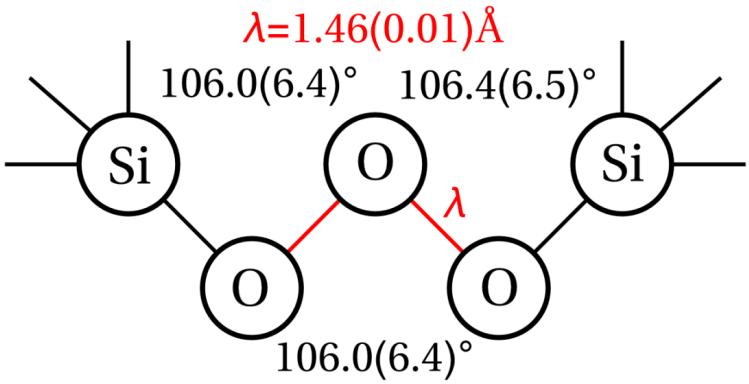

FIGURE 4.13 – Ozonyl defect with average angles and bonds lengths.

the ozonyl was not able to form and O_2 molecules were spontaneously released. In such cases final structure was stoichiometric silica with oxygen molecule trapped in one of the nearest cavities. This phenomena occurred in less than 5% of all configurations.

Figure 4.13 shows generic ozonyl defect structure with average geometry after the relaxation. Mean distance between oxygen atoms in ozonyl, for both sites, is 1.46(±0.01) Å, which is comparable with 1.428 Å of di-hydrogen trioxide [149, 150]. This distance is by 0.03 Å smaller compared to POL, but the spread is again very small and consistent with POL. Bond angle for all three oxygen atoms in ozonyl (two Si–O–O and O–O–O) is around 106(±6.4)°, which is again very close to structure of hydrogen trioxide, where H–O–O angle is 101.1°and O–O–O angle being 107.0°[149, 150].

Figure 4.14 shows distribution of E_f (a) and dihedral angles of Si–O–O–O (b). Formation energies (E_f) were calculated assuming reaction 2.4 with formula 4.3 where E_{ozonyl} is total energy of system containing ozonyl defect, E_{SiO_2} total energy of silica model and E_{O_2} total energy of isolated molecule in ground triplet state.

$$E_f = E_{ozonyl} - E_{SiO_2} - E_{O_2} \tag{4.3}$$

Average formation energy is 1.73(±0.49) eV with values ranging from 0.72 to 2.71 eV. As one could expect, this value is higher compared to POL (1.36±0.32 eV), but not by very large margin. Indeed one could expect to find both defects in real silica glass because the two distributions overlap with POL being more common. These findings further explain results described by [98, 99, 54] because some POL configurations with high E_f indeed have higher formation energy compared to ozonyls but in general, this is not the case. Comparing lowest formation energy configurations, which represent the system in thermodynamic equilibrium, the formation energies have values 0.56 eV and 0.72 eV for POL and ozonyl,

respectively, showing only a 0.16 eV difference.

Second part (b) of the figure 4.14 shows dihedral angle distribution because this property plays fundamental role in energy of the highest occupied states in O–O bond, as it has been shown in the case of POL. This histogram shows dihedral angles from both O–O bonds in ozonyl (Si–O–O–O and O–O–O–Si), therefore sampling number is double the number of configurations and consequently width of histogram bars is decreased to fit both distributions to the same scale. Dihedral angles vary from 5° to 175° with the average value of 82.0° and the standard deviation of 27.7°. Comparing the distribution with the POL, it can be observed that the ozonyl actually populates complete angular domain (between 0°and 180°). As it has been shown in figure 4.8, increasing the energy separation between highest occupied defect states should be symmetric with respect to the pivot where two states overlap, i.e. 90°. In this regard the ozonyl distribution across all possible angles actually seems to be more "natural". An anomaly is visible in the distribution between 110° and 120° with significantly lower number of configurations. The origin of this anomaly is unknown, however it has not been observed to have any effects on the further analyzed properties.

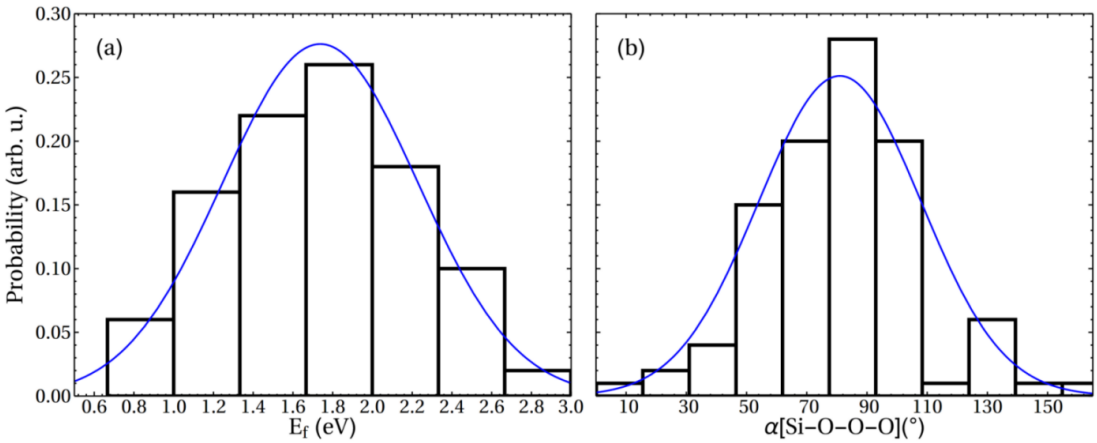

FIGURE 4.14 – Formation energy (E_f) and dihedral angle (α[Si–O–O–O] for both sides) distributions, respectively subfigures (a) and (b).

Electronic and optical properties

Because of relative structural similarity (multiple bonded oxygen atoms) between peroxy bridge and ozonyl defect electronic structure remains similar to some extent, primarily by highest/lowest states being combination of occupied π and empty σ non-bonding bonds.

Plots of electronic states are shown in figure 4.15. Similarly to POL the highest occupied and lowest empty states consist from 2 full and one empty 2p orbitals (p_x, p_y occupied and empty p_z), however they behave differently due to presence

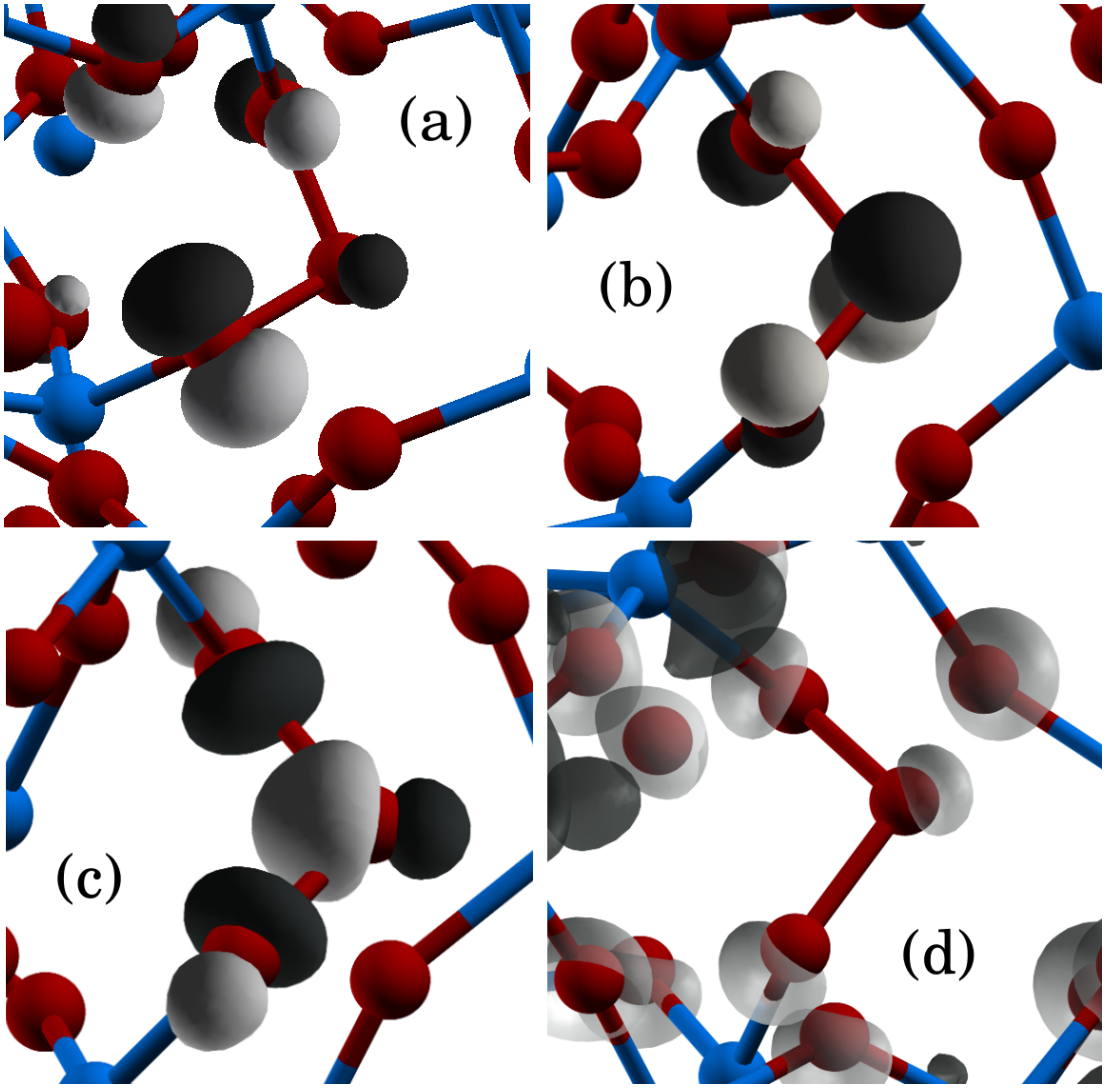

FIGURE 4.15 – Defect electronic states for the prototypical situation where two highest occupied defect states can be seen represented with letters (a) and (b), where the latter is HOMO with characteristic π^* shape. (c) and (d) represent σ^* shaped LUMO and BCB. Si and O atoms are represented in blue and red, respectively. Light and dark gray represent the + and - sign of the wave function respectively.

of additional oxygen atom and geometry. Highest occupied states are represented by letters (a) and (b). Very interestingly the shape of HOMO-1 is not consistent across the defect as it is more localized on particular outer atom. Compared to POL this state is also not pure defect state as it also shows signs of hybridization with network atoms. HOMO on the other hand is pure defect state with clear π^* nature only hindered slightly on outer atoms where little elongation can be observed towards bonding Si atoms. Panels (c) and (d) show empty states where the former shows LUMO and latter BCB. Combination of strong repulsive forces from σ^* bond and relatively sharp bond angles is responsible for complex shape of this state. In-plane shape of electronic states on all three atoms is typical for this bond (and very similar to POL), while lack of space on central atom pushes electrons outwards giving the state more π-like shape. Panel (d) shows oxygen 3s states, which are known to represent BCB [28]. Using DFT approach the gap has been again underestimated around 5 eV with empty defect state placed inside the gap.

Figure 4.16 shows projected density of states for different dihedral angles of Si–O–O–O. PDOS was again projected to orthogonalized p-states on oxygen atoms. Gray line represents average projection of TVB, blue, green, red and black are representations of the HOMO-1 with respect to different dihedral angles and the two sharp peaks just above 1 eV correspond to the projection of HOMO on the outer and inner O atoms in ozonyl defect. Energy position of the highest occupied states does not change significantly with respect to the dihedral angle, similar to the POL. Smaller peak (orange) is the projection on outer atoms in ozonyl bridge (atoms adjacent to the Si), while higher peak (purple) is the projection on central oxygen atoms in ozonyl bridge. Higher intensity of the latter shows that the oxygen 2-p state are much closer to the ideal p-states, while the p-states on outer atoms are affected by the vicinity of Si atoms as it can be seen in figure 4.15.

Looking at the energy position of the lower occupied defect state it can be again observed that the dihedral angle also controls the electronic structure of ozonyl defect. As it has been already described earlier, dihedral angle distribution of ozonyl spans angles between 5 and 175°with the mean value at 82°and the energy separation of HOMO and HOMO-1 is symmetric with respect to the origin, i.e. energy difference between the states is similar when dihedral angle increases or decreases by certain angle (for example 60° and 120°). Figure 4.16 only shows 4 configurations with change in dihedral angle of approximately 30°. Results are consistent with the electronic properties of POL, energy separation of two highest occupied states increases with dihedral angle. When the angle is close to 90° two states exhibit the smallest gap, which increases with the increase or decrease

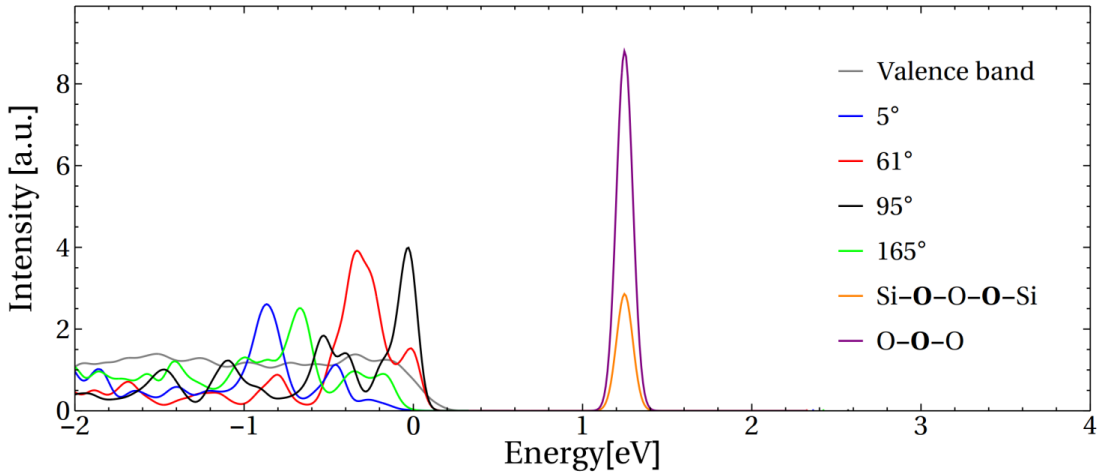

FIGURE 4.16 – Projected DOS on oxygen p state for highest occupied states in ozonyl for different dihedral angles. Gray line is average projection of TVB, blue, green, red and black are peaks of the HOMO-1 with respect to the dihedral angle and the two sharp peaks just above 1 eV correspond to the projection of HOMO on the outer and inner O atoms in ozonyl defect (oxygen atoms upon which DOS is projected are marked with bold O character).

of dihedral angle (due to symmetry). Contrary to the POL, two states exhibit minimum difference of about 1eV (in the case of POL the states overlap) which increases for approximately 1 eV with the change of dihedral angle by 90°. More importantly, the energy position of lower state is always within the valence band. It is safe to assume that this will result in optical behavior similar to the POL, when defect state is positioned within the TVB, contribution of delocalized valence band states will be higher than the contribution of defect states.

Figure 4.17 shows the density of states, calculated at the level of many body perturbation theory (GW approach), and corresponding optical absorption for the lowest formation energy configuration. Green dashed lines represent results from pure silica model while black lines are from model with the ozonyl defect. Electronic structure of occupied states is consistent with the DFT results. Electronic states are marked with lower-case letters, (a) is single occupied defect level positioned about 1 eV inside the gap,(b) is oxygen 3s, which represents BCB, and (c,d) being empty defect states. Again the position of BCB overlaps with the BCB of non-defective model confirming validity of used model. In the empty region, ozonyl defect induces two empty states with LUMO positioned just above 10 eV and additional defect level 1.5 eV higher. Again arrows are used to indicate lowest possible transitions with corresponding optical signatures shown on the graph in upper part of the image. Ozonyl induced two low energy excitations marked as A and B at 3.65 eV and 4.65 eV respectively. These are weak transitions from the highest occupied π^* like defect bonds into the σ non-bonding like orbitals within the conduction band.

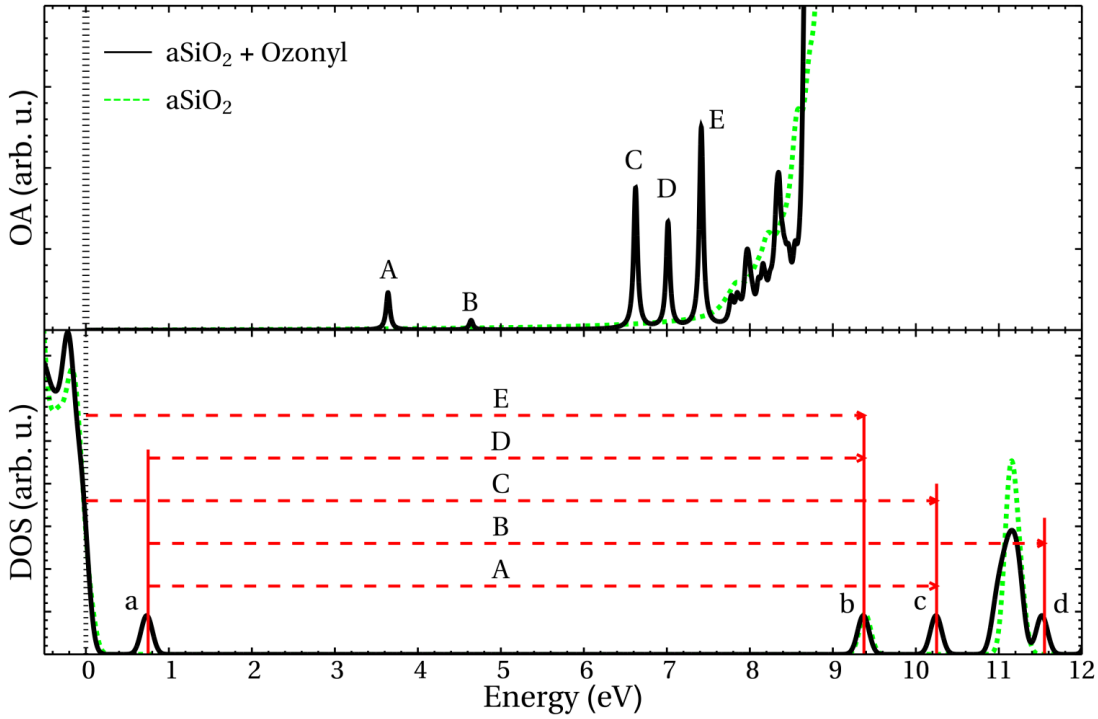

FIGURE 4.17 – Bottom : DOS of ozonyl defect in silica with four lowest allowed excitations marked on optical absorption spectra (on top). Transition A just below 3.4 eV is from HOMO to LUMO, B from HOMO to another molecular state within conduction band, C valence band to LUMO and D HOMO to conduction and E valence-conduction transition.

Intensity of the first peak is higher, however neither of oscillator strengths does not exceed 10^{-4}. Third peak (C) corresponds to transitions from the valence band to the LUMO, followed by transitions from HOMO to valence (D) and finally TVB→BCB excitation (E). It can be immediately observed that the probability of these transitions is noticeably higher, with the oscillator strength in the low 10^{-2} region meaning that this signature could be more probably observed in the optical absorption experiments (if not hidden by other optically more active defects). These values are surprisingly in a very good agreement with the experimental results presumably describing the POL defect [44], where absorption peak is clearly visible just above 7 eV. This discovery could lead to the assumption that ozonyl detection has been misplaced with more favorable POL (important notice that the defects were created by the irradiation at very high energy). Dihedral angles of presently analyzed lowest formation energy configuration for both Si–O–O–O bonds are very close to lowest energy separation (84°and 95°). This means the second highest occupied defect state is positioned relatively close to the TVB, however single particle decomposition of the excitonic structure involving TVB states reveals that the excitation consists in 80% from delocalized states of the valence band, confirming that dihedral angle has very small (if any) effect on the

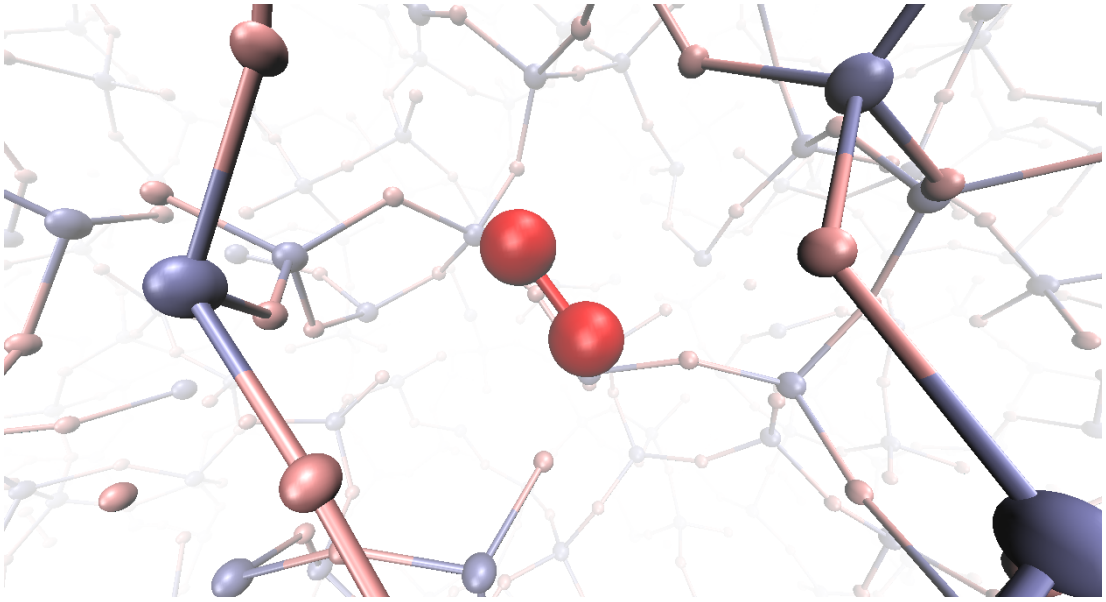

FIGURE 4.18 – Typical ball and stick image of oxygen molecule inside silica. Red balls represent oxygen atoms and blue balls silicon atoms.

optical properties of ozonyl.

4.1.4 Gaseous O_2

Molecular oxygen within bulk silica has been used with great success as a labeling tool in oxygen excess related experiments [2, 21, 60]. It has also been a subject of theoretical studies [57, 98, 99] which report that oxygen resides in ground triplet state of various sized cavities within the SiO_2 network. Incorporation energy of oxygen molecule has been shown to reduce as the volume of cavities increases [107]. O_2 molecules dissolved in silica could be precursors for POL and ozonyl bridges while their relation with creation of ozone molecules has been undoubtedly confirmed [59]. This subsection devoted on O_2, is meant to support comparisons and additional data for discussions. For a detailed study on O_2 formation and migration energies see reference [107].

Figure 4.18 shows typical position of oxygen molecule in the center of a cavity. Results agree with known literature [151, 98, 99] stating that ground state oxygen molecules is in triplet state. Simulations in triplet state have, on average, 0.70($\pm$0.21) eV lower formation energy compared to singlet state with values ranging from 0.13 eV to 0.87 eV.

More important though is the absolute formation energy calculated using equation similar to 4.3, where energy of silica model with interstitial molecular oxygen has been used as the first term. Sometimes identical initial configuration has been used however molecule has been then placed into different interstices which resulted in new unique configuration.

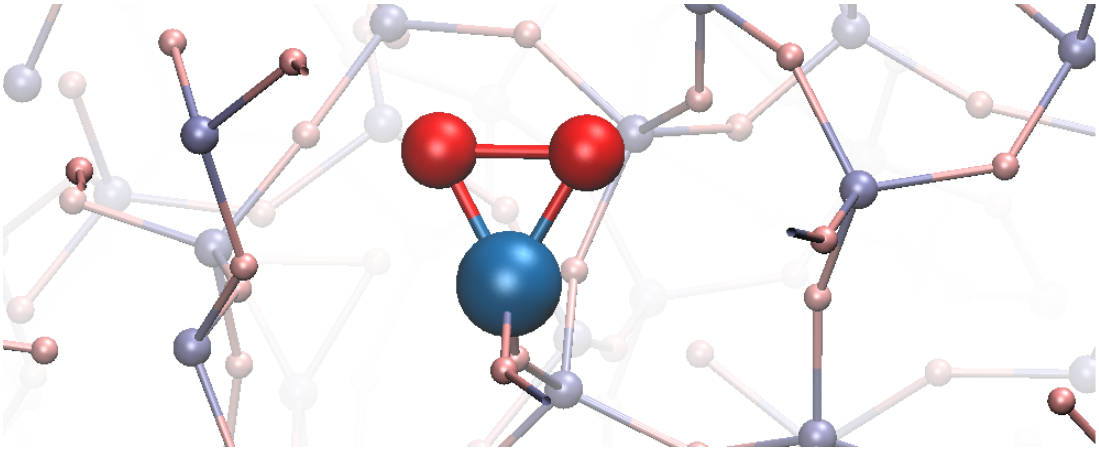

FIGURE 4.19 – Typical ball and point image of dioxasilirane defect. Red balls represent oxygen atoms and blue balls silicon atoms.

Results show that the formation energy (calculated using expression similar to equation 4.3 with first term replaced by $E_{SiO_2+O_2}$ spans from -0.20 eV to 0.50 eV with mean value of $0.05(\pm 0.23)$ eV. This means that, at thermodynamic equilibrium with an O_2 reservoir, for some of the cavities, it is favored to dissolve O_2 molecules. However, because of the high diffusion barriers (of the order of 1 eV [107]), the thermodynamic equilibrium condition is only valid at high temperatures for reachable timescales.

Presented results show that the molecular oxygen has by far the lowest formation energy when compared to other network defects. This agrees with the literature, not only on theoretical level but more importantly experimental side where molecular form of loaded oxygen is preserved. Only by further irradiations or thermal treatments signature of O_2 decomposition to form other network defects is observed [2, 21, 60]. These results also disagree with theoretical study in references [98, 99], where ozonyl is reported to have 0.23 eV lower formation energy compared to O_2 molecule, while results of this study show ozonyl has energy higher by almost 1.7 eV. The lack of statistical sampling in Ref. [98, 99], however, precludes a meaningful comparison.

4.1.5 Dioxasilirane

Dioxasilirane (DIOS) is a silicon analogy of dioxirane (which is very unstable at room temperature [152]), a compound where both atoms of oxygen molecule are bonded to single Si atoms as shown in figure 4.19. While dioxasilirane has been observed on silicon dioxide surfaces [69, 70] its existence has never been confirmed in amorphous silica [34]. In this part of research defects have been created in pure and Ge-doped silica (dioxagermirane - DIOG), where in the latter doping has been achieved by substitution of Si atom on which defect is localized.

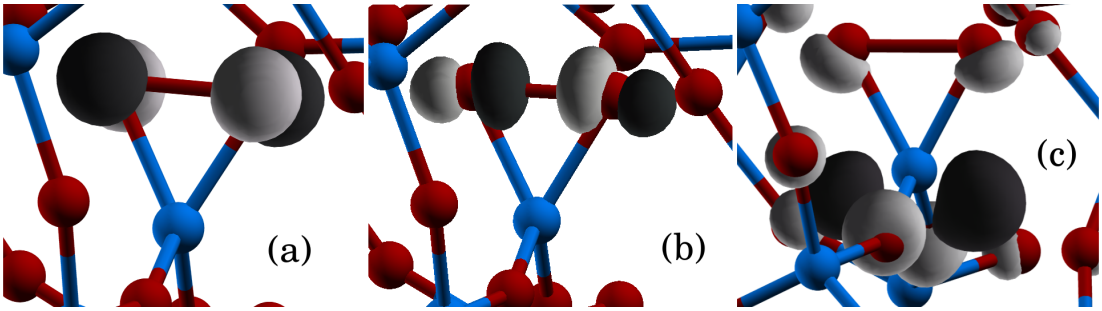

FIGURE 4.20 – Dioxasilirane defect electronic states around the band-gap:(a) HOMO π^* pair, (b) LUMO σ^* orbital and (c) LUMO+1 combination of Si3p and O 3s. Si and O atoms are represented in blue and red, respectively. Light and dark gray represent the + and - sign of the wave function respectively.

Dioxasilirane has been created by ad-hoc placement of oxygen molecule near the position of pre-existing Si-ODC(II)/GLPC and a further DFT full-relaxation. Additional information on modeling of ODC(II)/GLPC can be found in Ref. [30]. In this sense the DIOS can be considered as product of ODC(II)/GLPC passivation with oxygen.

Experimentally the signature of ODC(II)/GLPC passivation has been observed in oxygen loaded fibers [117, 153]. In the case of GLPC the O_2 loading suppress generation of defects under X-ray irradiation [117] however when irradiated by electrons at higher dose part of GLPC has been observed to recover [153]. The passivation mechanism is anyway still unknown.

The structure of DIOS is as follows : the two oxygen atoms are perpendicular to the bond between the silicon atom and the two neighboring network oxygens as it can be seen in figure 4.19. Average distances in defect are 1.67(± 0.03) Å for Si–O and 1.60(± 0.02) Å for O–O. This length is approximately 0.1 Å longer compared to POL defect, while the Si–O distance in defects is comparable to the length of this bond in network silica. Average O–Si–O angle in defect is 57.4(±1.85)°. The formation energy of 3.24(± 0.53) eV calculated as :

$$E_{\mathrm{f}}^{\mathrm{dios}} = E_{\mathrm{SiO_2}}^{\mathrm{dios}} - E_{\mathrm{SiO_2}} - \frac{1}{2}E_{\mathrm{O_2}} \tag{4.4}$$

is significantly lower than the 6.73(± 0.43) eV of SiODC(II) (calculated as $E_{\mathrm{f}}^{\mathrm{odc(II)}} = E_{\mathrm{SiO_2}}^{\mathrm{odc(II)}} - E_{\mathrm{SiO_2}} + \frac{1}{2}E_{\mathrm{O_2}}$, see reference [30]). This again shows the passivation is energetically favorable when O_2 molecules are available (as has been also confirmed by experiments [117, 153]).

Defect electronic states are presented in figure 4.20. Only highest occupied defect 2p oxygen state is visible as lower one is below the Top of the Valence Band. Lowest empty state is again 2p σ^* bond similar to other network defects, while second empty state is hybridized around 3p orbital of Si atom hosting the defect.

DIOG has been created by an interaction of oxygen with GLPC in Ge doped silica [117, 153]. Procedure for creation of DIOG on GLPC is identical to the ODC(II), in particular oxygen molecule is ad-hoc placed near pre-existing defect followed by a complete relaxation at DFT level. Larger dimensions of Ge atoms have important impact on geometry of DIOG defect, average Ge–O distance is 1.823(± 0.03) Å.

O–O distance is comparable with defect on silicon site at 1.61(± 0.01) Å meaning that extra Ge–O distance must be compensated with reduced O–Ge–O angle with mean of 52.3(± 1.0)°.

Formation energy of GLPC is again reduced with the absorption of oxygen molecule in the form of dioxagermirane. This decrease is however less significant compared to pure silica DIOS defect. Formation energies of Ge-DIOS are spread between 4.15 eV and 4.87 eV with mean value of 4.46 eV while average formation energy for GLPC is 5.19 eV [30]. This change is likely related to the different bonding with the germanium 4p orbitals as compared to 2p of silicon.

Overall these results show that the dioxasilirane defects might be a candidate for explaining the interaction of excess oxygen and lone pair defects (ODC-II/GLPC), which has been shown to completely annihilate these kinds of defects [117, 153]. On the other hand no experiments have been able to observe this defect in a-SiO_2, while it has been well characterized on SiO_2 surfaces [34]. While optical/emission or vibrational properties are not known at this time, it could be also possible that its concentration is low compared to other defects or that it might be converted into different species.

4.2 Defect formation mechanisms and oxygen exchange

Historically combinations of multiple spectroscopic techniques have been commonly used in order to identify the structure of oxygen excess defects in silica [2, 21, 36, 26, 34]. However this approach has often fall short due to low defect concentrations and weak spectroscopic signatures. Consequently some approaches have been developed to indirectly assess the presence of such defects. One particularly interesting approach is based on interconversion of defects. This technique is based on exposing samples to different conditions and treatments while measuring quantities of known defects. Through thermal treatments activation energies can be extracted and further exploited to extrapolate possible reaction mechanisms [44, 45].

Without the support of modeling it is however very difficult to reach a deep

atomic-scale knowledge.

This chapter presents and discusses first-principle modeling of different oxygen exchange and reaction guesses. The possibility to exchange via vacancies will be discussed with a section dedicated on the passivation of ODC(II) to form dioxasilirane. The spin state of O_2, and in particular, the conservation of spin, often neglected in theoretical studies [98, 99, 151], is addressed. On the basis of the results, previous models[44, 45, 102] for oxygen-related reactions are discussed and alternative models are proposed. Comparing results of this work with experiments, ozonyl bridges might be the key (as intermediate stage) in many oxygen-related reactions.

4.2.1 O_2 singlet to triplet treatments

The pre-requisite for addressing oxygen-related reactions is a deep knowledge on the O_2 molecule. Figure 4.21 shows ground state molecular orbital diagram of O_2 molecule. According to the molecular orbital theory six out of eight electrons from highest occupied 2p states of oxygen molecule form σ and two π states while the two remaining electrons remain unpaired in the same spin state. The two highest occupied states are therefore singly occupied molecular orbitals (SOMO), however in the discussion regarding oxygen exchange they will be referred to as HOMO for the sake of clarity. These two states are consequently degenerate in energy with total spin being 1, which, according to Hund's rule, means that the triplet state is energetically favorable. Therefore, the O_2 ground state is magnetic (spectroscopic notation $^3\Sigma_g^-$).

This electronic state induces two low energy excited states : The first, commonly referred to as singlet oxygen ($^1\Delta_g$) with an energy of approximately 0.97 eV (1272.2 nm) is responsible for radiative near-infrared photoluminescence at ambient conditions ($^1\Delta_g \rightarrow {}^3\Sigma_g$). In gas phase this state is extremely long lived (72 min), however interaction with solvents and catalysts reduces its lifetime down to nanoseconds [5]. Second state has 1.63 eV higher energy with lifetime of 11.8 s in gas phase. Again life time is reduced by interaction with solvents and catalysts. In some solvents this decay reduces to lower singlet $^1\Delta_g$ non-radiatively [154].

The emission related to the singlet-to-triplet transition (and vice versa for the excitation energy) has been also observed experimentally in oxygen exchange related reactions [44, 45] at low temperatures. As in the molecular case, the intensity of this emission decreases exponentially with increasing temperature.

This behavior is attributed to the opening of non-radiative decay channels [101, 103]. Previous studies that explicitly treat a triplet ground state for the oxygen in conjunction with exchange reactions [98, 99, 151] in silicon or silica

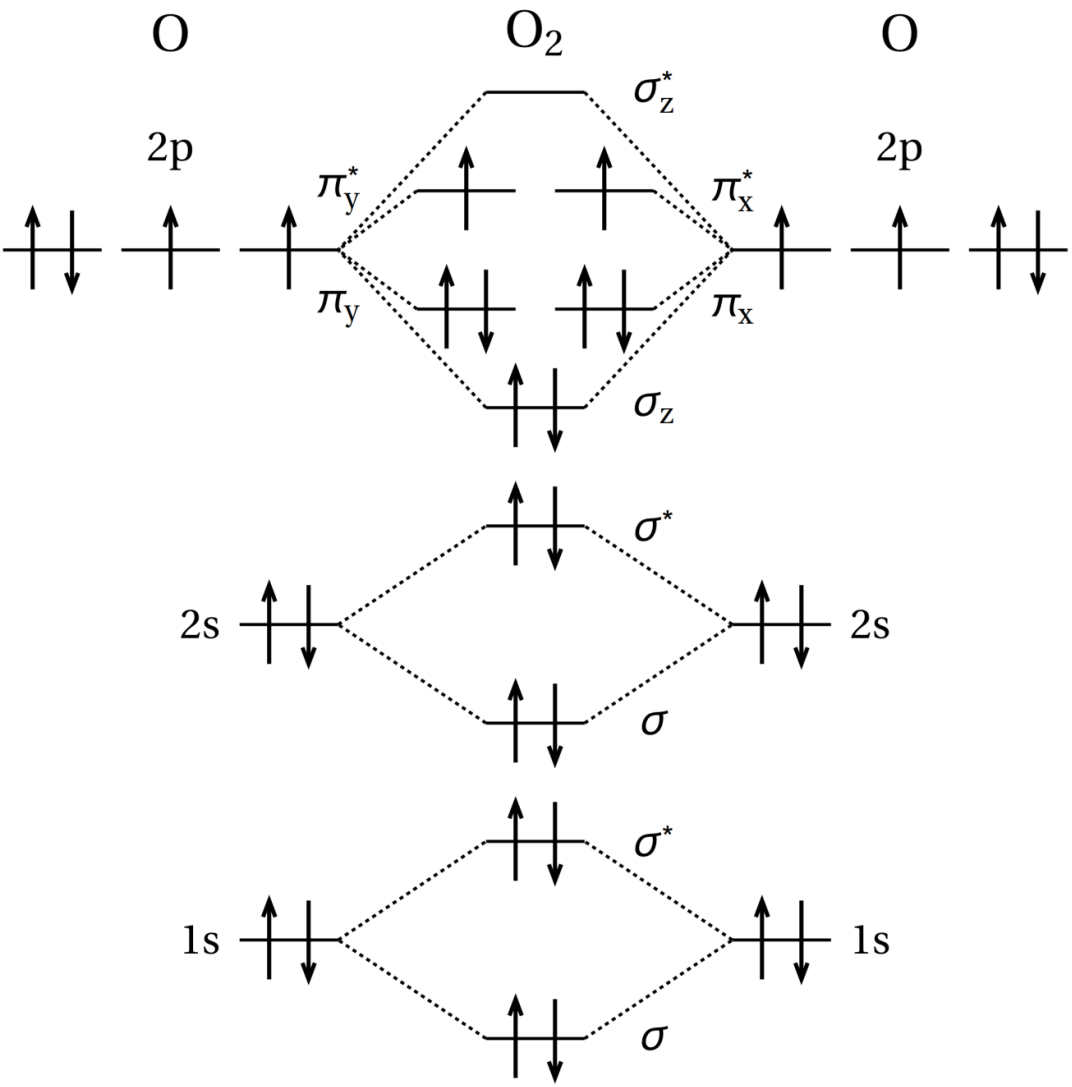

FIGURE 4.21 – Molecular orbital diagram of oxygen molecule in ground triplet state ($^3\sum_g^-$).

assume that the system changes from triplet to singlet state when the molecule reacts with the network bypassing completely the spin conservation selection rule. However, excluding Spin-Orbit interactions, the triplet ground state should prevent oxygen to react individually and directly with diamagnetic molecules or sites without the use of light or "catalysts", see for instance [155].

As many of the presumed reactions that O_2 might induce within the silica network, are assumed to be non-radiative, to involve a single O_2 molecule and to result in non-magnetic defect centers, a question naturally rise : if these reactions might occur, what carries the remaining spin ? Providing with the final answer is far beyond this work, as it would require a time-dependent full-relativistic non-adiabatic and non-collinear spin treatment, however, the following sections try to provide with some additional discussion elements. Indeed, an oxygen molecule

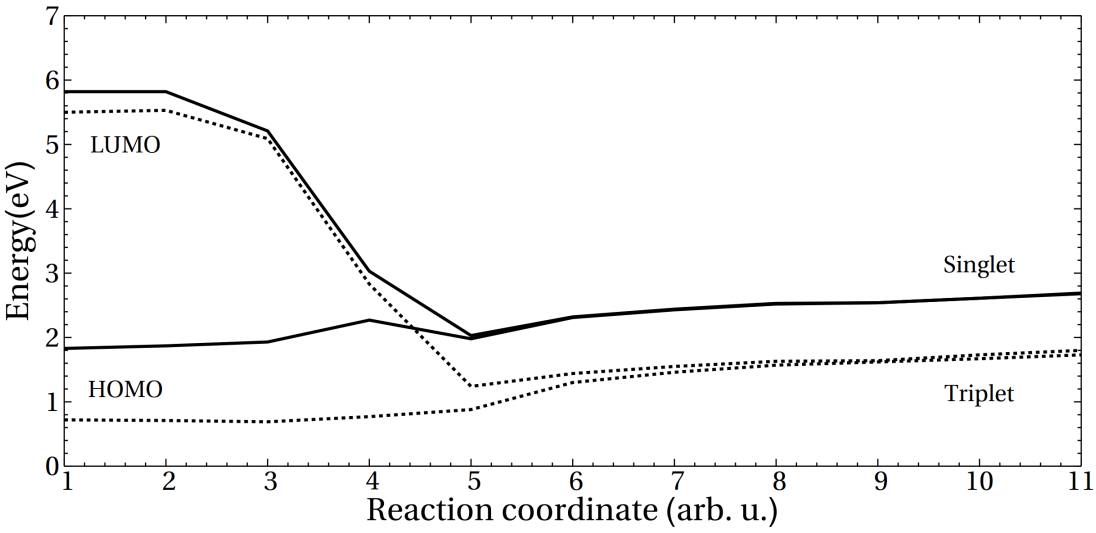

FIGURE 4.22 – Energies of HOMO and LUMO through the typical reaction involving release of oxygen from network which undergoes singlet to triplet transition. Continuous line represents results from singlet calculations and dashed results with triplet (spin up) from spin polarized calculations.

in its ground state (triplet) do not oxidize reactants in singlet state due to the spin conservation and a lot of effort is still devoted to finding new conversion routes (chemically, enzymatically, or photochemically) [156, 157].

To properly identify the spin state change the electronic structure has been explicitly analyzed in the exchange reactions. Results are presented in figure 4.22 on prototypical example describing release of oxygen from ozonyl defect which will be thoroughly described in following section.

This figure shows energies of 2p HOMO/LUMO states during the release of oxygen molecule from network (ozonyl defect). Continuous line represents results for singlet calculations and dashed line for triplet from spin polarized calculations. Calculations of triplet state have been performed on a constrained system meaning that each image from calculations in singlet state has been recalculated in triplet without the relaxation. This ensures the reaction path remains the same allowing direct comparison. Relaxation of oxygen molecule in singlet or triplet state yields structure with negligible difference further proving the validity of the approach. When molecule is incorporated in the network the two states are separated by a gap as it can be seen for coordinates from 1 to 3. Energy gap is clearly underestimated with values below 4 eV for singlet and approximately 5 eV for triplet because the calculations were performed on a DFT level. Frames 4 and 5 correspond to the saddle point of reaction where molecule breaks off the network. This is evident by two states becoming degenerate in agreement with electronic structure of oxygen molecule (figure 4.21).

Frame 4 exactly shows why spin degree of freedom must be analyzed explicitly.

In the singlet state the energy difference between the two states is relatively small around 0.7 eV while the results for triplet state show energy difference of about 2.3 eV. This means the molecule in this step has not yet reached ground triplet state as two states are not yet degenerate. If calculations would have been performed in singlet state, it could be possible to estimate that the ground state has already been reached because the energy difference is smaller than the lowest possible excited state ($^1\Delta_g$).

Two states become completely degenerate in the next step (coordinate 5), when the molecule is completely released from the network. After release (coordinate 5) the two states remain degenerate until the end of reaction, with the energy of singlet calculation being higher by approx. 1 eV. This value is in very good agreement with the known energy difference of 0.97 eV [5, 61].

In principle, a full-relativistic calculation with the Spin-Orbit coupling will prevent the two energy surface to cross, thus opening an energy gap. The probability to cross the gap, will depend on the matrix elements of the Spin-Orbit interaction that allows non-radiative spin flipping (Intersystem Crossing). Whether the system decay non-radiatively or radiatively depends however on the relative non-radiative versus radiative transition probabilities. An other non-radiative path that could be envisaged is the coupling of two molecules. Indeed, if two O_2 molecules are correlated (close enough) the ground state is of spin=0 (non-magnetic) thus allowing for a reaction resulting in a non-magnetic state.

4.2.2 Oxygen excess centers

Direct oxygen exchange through ozonyl

Release of oxygen from ozonyl has been already studied to some extent [98, 99]. These studies however report ozonyl as the lowest energy configuration, with energy being 0.23 eV lower compared to O_2 molecule trapped in interstices. This means that in equilibrium ozonyl would be preferred as the most common network oxygen excess defect. However ozonyl has not yet been experimentally confirmed while many studies reported gaseous oxygen in silica exists also after different treatments [21, 60, 58]. These studies also reports a barrier for release of O_2 molecule from ozonyl with value around 2.5 eV, with barrier for forming ozonyl of 2.4 eV. Authors concluded that these activation energies are way above the migration barrier for oxygen in silica, which should dominate the O_2 exchange. Another important comment of said study is the treatment of singlet network to triplet molecular ground state of oxygen. Simulations were performed by allowing the software to automatically select between two states based on lower energy. Authors reported that the system switches between two states at the saddle point

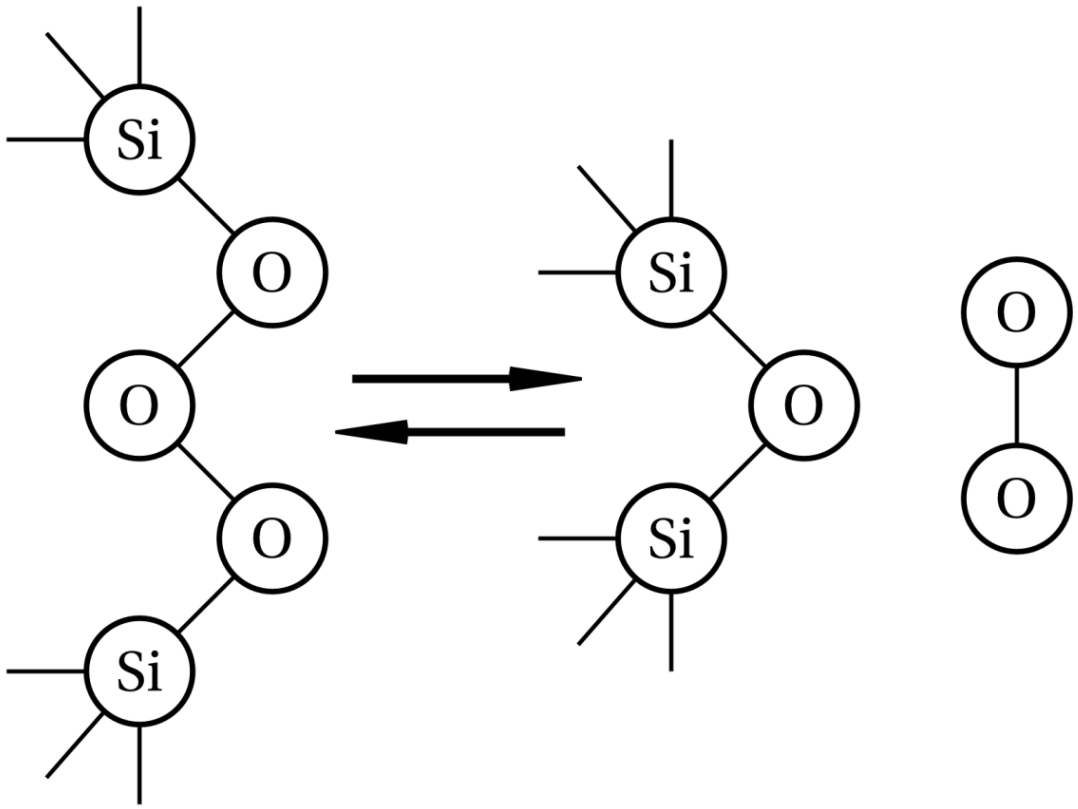

FIGURE 4.23 – Schematic representation of direct O_2 release from ozonyl defect.

when the molecule, which is in this state bonded to silicon atom as peroxy radical (Si–O–O·), bonds with the non bridging oxygen atom (Si–O·) that had broken off the same silicon in the previous step. Release of oxygen from the neutral network species however requires radiative singlet to triplet transition with characteristic photo-luminescent emission at 1270 nm as described by [60, 58] but approach used in reference [98, 99] does not predict this emission.

Again statistical approach is required because of site-to-site disorder in amorphous materials. Nine configurations have been selected according to their formation energy, five sample mid range while two representatives have been selected for both high and low parts of the formation energy distribution. This number is not, by any means, large enough to provide proper statistical analysis of the reaction path however it lays reasonable foundation for comparison with experiments. Main reason is that while NEB simulations are not computationally most challenging (one NEB optimization consisting of N images translates into N geometry relaxations at DFT level) they can be quite lengthy, which is the main obstacle in calculation of statistically meaningful set of reaction barriers. Formation of dissolved oxygen in silica models has been described in section 4.1.4. A number of tests have been performed by moving oxygen atoms into different interstices surrounding ozonyl defects and results show that the barrier increases

noticeably as soon as there are other atoms obscuring the path.

Consequently only the optimal paths have been studied. The results from sections 4.1.3 and 4.1.4 are compared to show the configurations with O_2 molecules in triplet ground state have on average 1.68 eV lower formation energy compared to ozonyl (1.73 eV for ozonyl and 0.05 eV for oxygen molecule respectively).

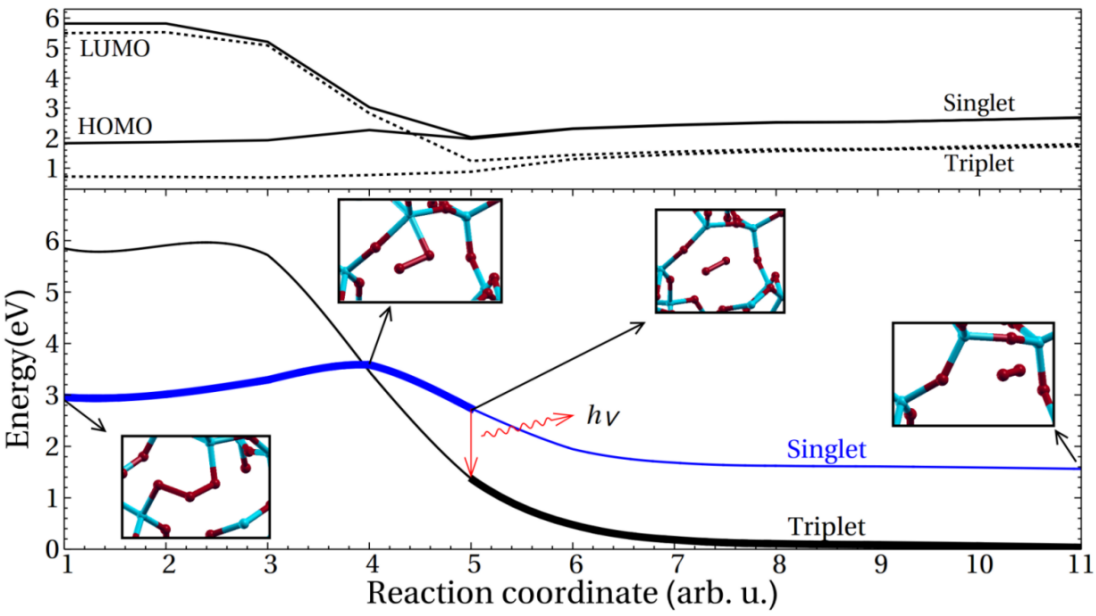

FIGURE 4.24 – Typical reaction barrier for oxygen exchange between ozonyl defect and molecular oxygen with inset images of the reaction. Thicker lines are used to represent actual reaction path with red arrow marking characteristic oxygen singlet to triplet relaxation with emission of photoluminescence.

Activation barriers (E_a) for release of oxygen molecule from ozonyl defect range from 0.44 eV to 1.35 eV with mean activation energy of 0.90 eV, while activation energies for reverse reaction (formation of ozonyl through absorption of O_2) span between 1.08 eV and 2.43 eV with average of 1.87 eV. Typical reaction barrier can be seen in figure 4.24, where blue line represents results from spin non-polarized, i.e. singlet state, calculations and black line shows spin polarization which describes triplet state. Y axis is presented as formation energy (equation 4.3 for the case of ozonyl) in all plots of reaction barriers so the starting values are different for various defects.

Reaction starts by movement of two oxygen atoms towards the vacant space creating strain in the ozonyl defect. This movement of oxygen atoms drags two silicon atoms toward each others until distance is small enough that oxygen atom which remains in the network can bond with the second silicon atom, i.e. the reconstruction of stoichiometric network.

Because the breaking of Si–O bond is energetically most unfavorable, the release of O_2 molecule and recombination of network occurs simultaneously, i.e. in

the saddle point (step number 4). As it can be seen on the second inset image of figure 4.24 oxygen remains relatively close (represented with a bond) to the Si atom meaning that the total energy remains pretty high. Since the distance to nearest silicon atom is relatively small this might imply there remains some weak bonding and the oxygen molecule might have not yet reached its ground state. In the next step (reaction step 5) the molecule becomes completely released from the network followed by a migration towards the center of void and relaxation of the network.

Black line represents same reaction calculated using fixed spin charge (triplet state). In this case the initial energy is much higher as can be expected considering the ground state is singlet. However as the reaction progresses with the release of oxygen and the triplet state total energy becomes smaller. Considering only total energy difference intersection between singlet and triplet occurs near the saddle point, as has been also stated by earlier studies [151, 98, 99].

Analyzing the energies of defect states surrounding the gap (HOMO and LUMO) however shows that the two states are not yet degenerate in the saddle point (coordinate 4) as they should be in the oxygen molecule. This indeed confirms that O_2 molecule is at this point still bonded to network and its electronic structure has not yet relaxed into ground triplet state. Lines representing singlet and triplet levels intersect between points 4 and 5 clearly indicating the ground state is reached after molecule has been released from the network. Vertical red arrow represents characteristic singlet to triplet relaxation of oxygen molecule (PL active at 1270 nm/0.97 eV), which occurs after the molecule completely breaks of the network. This result does not agree with previous studies [151, 98, 99] where singlet to triplet transition is predicted in saddle point, clearly showing shortcomings of automated determination of spin state, especially if it is based only on total energy.

In comparison with previously calculated barrier from references [98, 99], results of this work show average barrier is approximately 60% lower (0.9 eV from this work compared to 2.4 eV from references [98, 99]). Reaction path described in these references is very similar with major difference regarding the value of barrier and singlet to triplet transition. Average activation barrier for release of oxygen from the ozonyl defect is approximately 0.5 eV lower than activation barrier for oxygen migration which has been placed between 1.12 eV and 1.70 eV [57, 106, 107, 108, 109, 110]. However as stated earlier, activation energies range from 0.44 to 1.35 eV while the sampling set is not sufficient for proper statistical representation.

Experimental data shows that oxygen singlet to triplet characteristic PL emission can be clearly observed at low temperatures [45, 60] while its intensity

is reduced at higher temperatures [103, 104]. The experimental evidence for the characteristic PL oxygen singlet-to-triplet transition at low temperatures [45, 60] might be consistent with our proposed release of O_2 from ozonyl. Because of the quenching of O_2 PL as a function of temperature, it would be very difficult experimentally to verify if the release of O_2 by two adjacent POL pass through an ozonyl intermediate stage.

The described O_2 triplet to singlet transition requires additional "activation" conditions for O_2 reactions in silica, for example the incorporation of oxygen molecule into ozonyl defect would require promotion of molecule from ground triplet state to excited singlet. In majority of experiments this has been achieved through photo activation [2, 45, 60, 106, 110]. Photo activation is allowed within LS coupling selection rules [158].

Oxidation of silicon surfaces for commercial purposes is generally performed at temperatures between 800 °C and 1200 °C which might be high enough for thermally activated triplet to singlet transition [2, 102]. Temperatures around 500 °C, which are commonly used for diffusion based experimental loading of SiO_2 with excess oxygen, on the other hand appears too low in order to promote integration of oxygen into the network [45, 60, 101] and a subsequent photo-activation/photolysis is needed.

Oxygen release from multiple peroxy defects

In the past studies [98, 99] two peroxies have been found to have formation energy 0.92 eV higher compared to the gaseous molecule. Two main arguments not favoring two peroxy bridges compared to the ozonyl is higher formation energy (2.53±0.44 eV for two peroxies compared to 1.73±0.49 eV of ozonyl) and energetically expensive dissociation of oxygen molecule (5.15 eV). However as described in 4.1.2 creation of two peroxies is highly plausible with the dissociation of oxygen in harsh environments like under irradiation (laser, X-ray, neutron) or at high temperatures.

Again standard approach has been used to model the release of O_2 molecule from two peroxy links meaning that oxygen atoms have been displaced into interstice followed by a full relaxation of the structure and finally NEB has been performed using 11 reaction steps.

In comparison with previously analyzed reactions, release from two peroxies turned out to be computationally a much more complex problem. Both adjacent and non-adjacent configurations (described in section 4.1.2) were calculated and analyzed however it turned out that NB with 11 steps is only able to describe release of oxygen from adjacent peroxy sites while non-adjacent configurations turned out to be too complex problem for this approach.

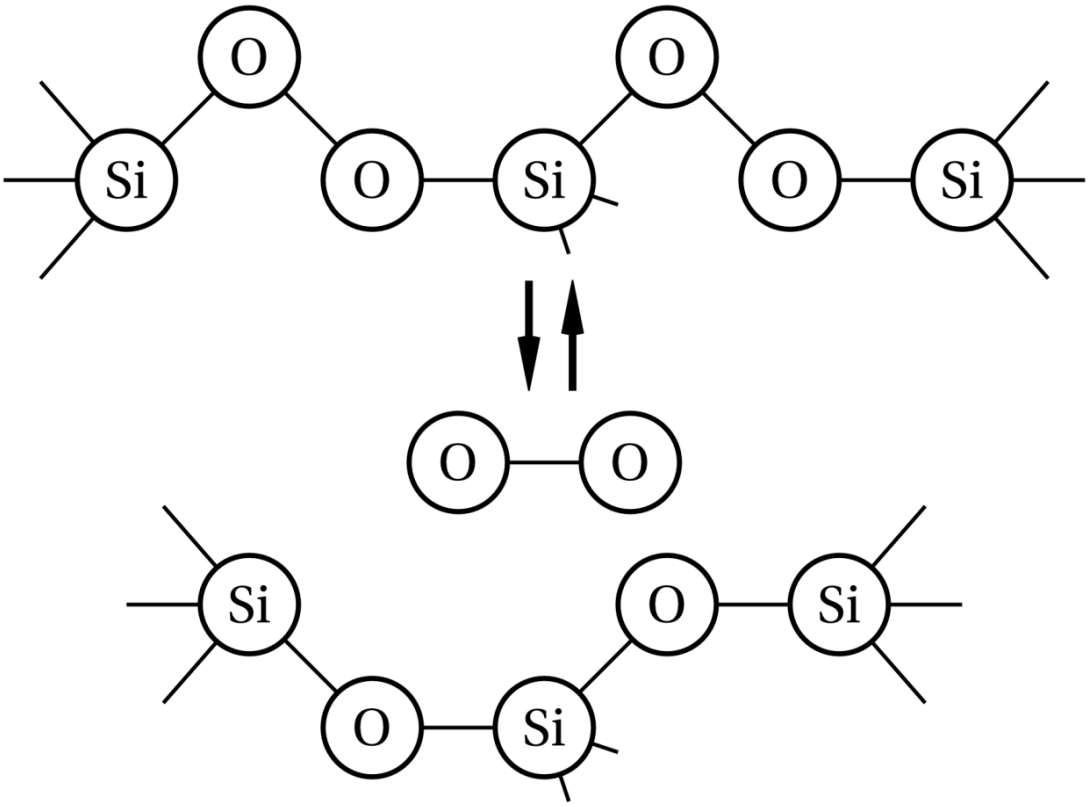

FIGURE 4.25 – Schematic representation of O_2 release from a pair of adjacent peroxy link defects.

Typical reaction barrier for adjacent sites is shown in the figure 4.26. Double peak of the graph means that this reaction occurs in two steps, which is the main reason for increased complexity of the simulations. Large gap separating two barriers also indicates that the migration of two steps is more unlikely to occur simultaneously and the separate migrations are favorable. Consequently the reaction path is longer.

First step corresponds to the migration of a peroxy into the position of another peroxy which results in the formation of ozonyl defect followed by a release of oxygen (second peak). Later reaction is identical to release of oxygen from ozonyl described in the section 4.2.2. Energies of defect states near gap are not shown, as system remains in singlet state until the release of oxygen from network as also described above.

Oxygen migration between adjacent sites is characterized by relatively small barrier ranging from 0.05 and 0.4 eV with mean of 0.13 eV. Such low reaction barrier might indicate that this kind of defect is kinetically unstable and can readily migrate into more stable form, ozonyl. Results of formation energies presented in section 4.1.2 show that while adjacent configurations have, on average, lower formation energies compared to the non-adjacent sites this trend seems completely randomized as the function of distance.

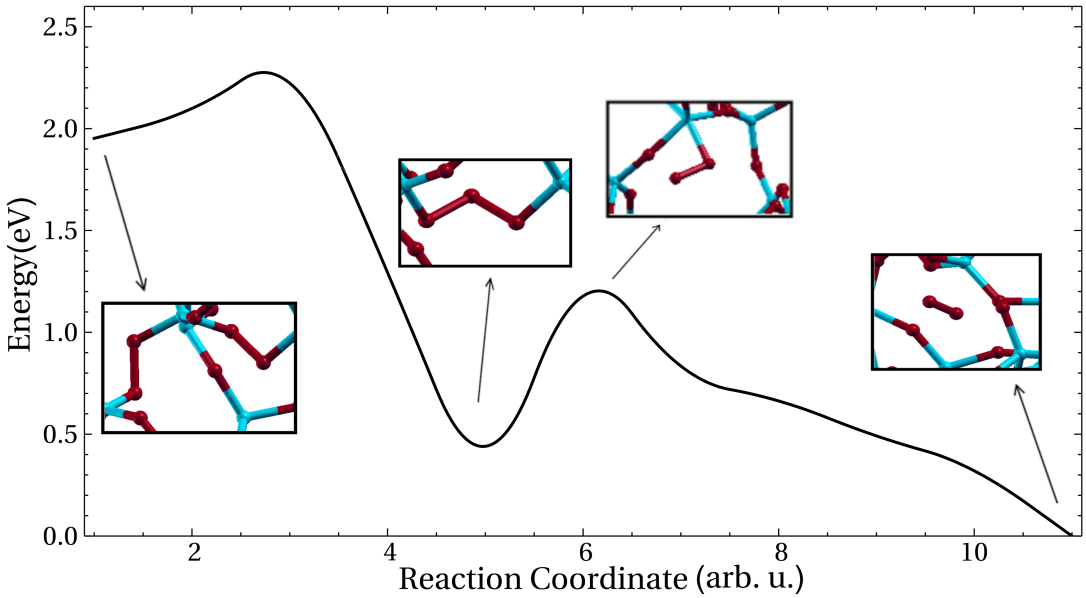

FIGURE 4.26 – Typical reaction barrier for the release of oxygen from two POLs. First peak represents migration of one POL and formation of ozonyl, from which oxygen molecule is then released (second peak). Silicon is represented by blue and oxygen by red spheres.

Older studies place the activation barrier for oxygen migration between 1.12 eV and 1.70 eV [55, 57, 106, 107, 108, 109, 110], however present study appears to be the first where multiple interstitial defects are placed at the distance where they could interact. Small reaction barrier might be a sign that there still exists an attractive force between defects, however its contribution to total energy would not be large enough to make this trend visible among the effects of structural disorder. Barrier for reverse reaction ranges from 1.6 to 2.2 eV without the inclusion of oxygen triplet to singlet excitation.

As mentioned earlier, release of oxygen from multiple non-adjacent peroxy configurations turned out to be computationally too complex problem for used approach. Proper description of such complex process would require more NEB steps which would however make simulations computationally too expensive. Nevertheless a number of preliminary studies have been performed using lower accuracy criteria with the purpose of observing main patterns of the process. Results show that this process would require multiple migrations of peroxies resulting in the formation of ozonyl and finally the release of oxygen molecule from the network. Because of lower criteria numerical results like activation energies cannot be considered to be accurate but qualitatively combination of results for adjacent and non-adjacent sites show the most important properties of the process. Release of oxygen molecule from multiple peroxies does not occur via direct release but through oxygen migration until ozonyl is formed followed by a release of

molecule. To simplify the problem both reactions can be analyzed separately.

Release of oxygen from ozonyl has been already described in the section 4.2.2 of this work where activation barriers between 0.44 eV to 1.35 eV have been reported. Second barrier from the figure 4.26 describes identical reaction with barriers spanning between 0.53 and 0.74 eV. These results are consistent with data from section 4.2.2 which describe identical reaction in different circumstances.

First part of the reaction, oxygen migration in SiO_2, remains one of the most controversial topics in the field even after numerous years and studies devoted to it. This work however only addresses particular case of 2 peroxies migrating toward each other. Multiple generic cases of non adjacent peroxies have been considered. In the first stage peroxies migrated towards each other until ozonyl has been created in the final step.

Table 4.6 – Migration energy of different configurations involving two peroxy defects. Average POL values represent mean of combined adjacent and non-adjacent configurations.

Formed species	E_a (eV)	Average E_a (eV)
Adjacent POL	1.46 - 1.74	1.61
Non-adjacent POL	1.61 - 1.93	1.77
Average (POL)	1.46 - 1.93	1.64
Ozonyl	1.00 - 1.52	1.19

Table 4.6 shows reaction barriers for different POL migration configurations. Values for migration of single peroxy species range from 1.46 to 1.93 eV with mean value of 1.64 eV. These results are once again within known migration barriers of oxygen (1.12 - 1.70 eV) [55, 57, 106, 107, 108, 109, 110]. Separating the barriers for adjacent and non-adjacent species shows that activation barrier is lower when two peroxies are closer to each other. In this configuration there was initially a single non defective site between two peroxies into which an oxygen atom migrated resulting in the adjacent peroxy species. Activation energy for this reaction ranges from 1.47 eV to 1.74 eV with average value of 1.61 eV. When migration of peroxies ends with non-adjacent species mean activation energy is slightly higher at 1.77 eV with values spreading from 1.61 eV and 1.93 eV.

Activation energy is lower for defects that are closer to each other, i.e. adjacent species, which might again indicate the existence of attractive force between defects. This is most evident in the final step of migrating oxygens, where adjacent peroxy migrates into neighboring peroxy forming an ozonyl. Activation energy for this reaction spans from 1.00 to 1.52 eV with mean of 1.19 eV which is on average 0.5 eV lower when compared to migration of two POLs for both adjacent

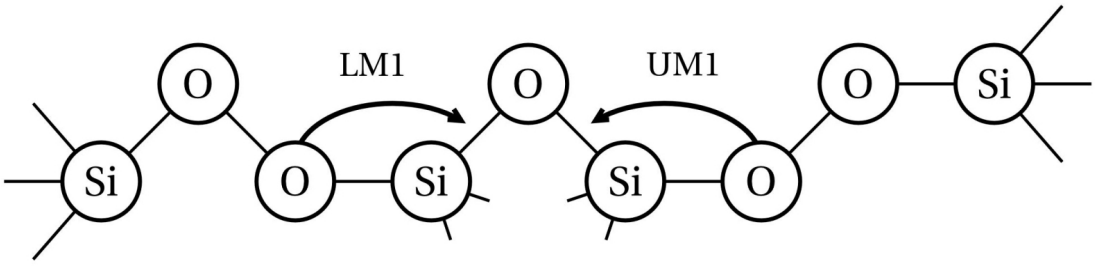

FIGURE 4.27 – Schematic representation of simulated two POL migrations.

and non-adjacent species. Combination of these results with formation energies presented in section 4.1.3 indicates that ozonyl should be favorable configuration over two network oxygen atoms in relative vicinity.

However large difference between the results for combined or separated migration and oxygen release needs to be addressed. Figure 4.27 shows a case when pair of non-adjacent peroxies separated by a single non defective site are migrating toward each other. Migration from the left hand side to right will be denoted as "lm1" while migration from right towards left "um1" as it can be seen in figure 4.27.

Comparison of activation barriers for simultaneous migration of two peroxy links is shown in figure 4.28. Upper barrier represents preliminary migration of both sites (lm1 and um1) in the same calculation that results in the formation of ozonyl. It can be seen that the reaction is pretty complex with three distinct peaks. Better description could have been achieved by using multiple climbing images however this might lead to loss of some information because 11 discretization steps are not enough to describe such complex reaction. Consequently reaction has been separated into two parts, which effectively doubled the number of reaction steps.

In the preliminary calculations (upper figure) first peak corresponds to the migration of site lm1 while second peak to the um1. A small peak at coordinate 5 corresponds to small rotation of peroxy at site lm1 and does not represent any significant structural change. Final peak describes the migration of um1 site POL and creation of ozonyl defect.

When two sites are analyzed separately it can be observed that the migration of both site is comparable between both approaches, however values of barriers are not completely identical, which can be expected as both are now allowed to climb independently due to climbing image technique. Activation barrier has value of only 0.27 eV between steps 8 and 9 in upper figure while in separate calculation (lower figure) it has value of 1.14 eV. This implies that a great care needs to be considered when calculating complex multi-step reactions, especially with regards to the number of path discretization points and use of climbing image technique. In this case it can be again confirmed that use of 11 reaction steps with single CI

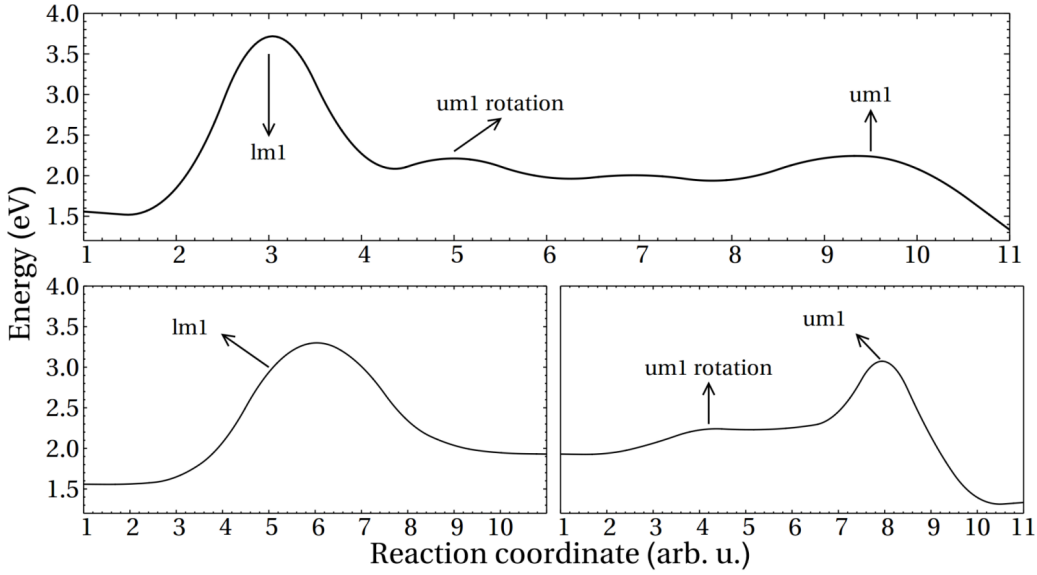

FIGURE 4.28 – Two POL simultaneous migration (upper image) compared to the same reaction performed separately (bottom image).

is clearly not adequate resulting in different barriers for reactions. This shows that results presented in the beginning of this chapter where migration and release has been performed in single calculation with standard 11 NEB reaction steps is probably not adequate to properly describe the release of oxygen in complex multi step reactions (like migration of POL and release of oxygen molecule) and consequently does not provide accurate values for the activation barriers.

Another consideration regarding the effect of local structure and energy on migration of multiple peroxies is provided by figure 4.29. In this case both barriers represent migration from um1 initial site into neighboring site as shown in schematic figure 4.27. Only difference is the state into incorporation site, which is in the first case (upper plot) non-defective while in the second plot already contains POL defect as a result of lm1 site migration (lower plot). This means the site of origin is identical in both barriers, however the total energy of the system and structural surrounding of the defect have changed. Consequently the migration behavior of oxygen atoms changes. In the first figure, migration is characterized by two peaks, first small with E_a of 0.43 eV which corresponds to first migration into another neighboring site followed by a second peak with height of 1.47 eV representing final migration toward the designated site. In the second plot the target site is already hosting a POL defect. This barrier is characterized by a broad plateau before the migration, which corresponds to a rotation of um1 POL before the migration with a barrier of 1.14 eV and a formation of ozonyl. In both cases the activation energies are consistent with previous findings. This analysis again highlights that care is needed when analyzing complex migration phenomena as final results might depend on initial local structure.

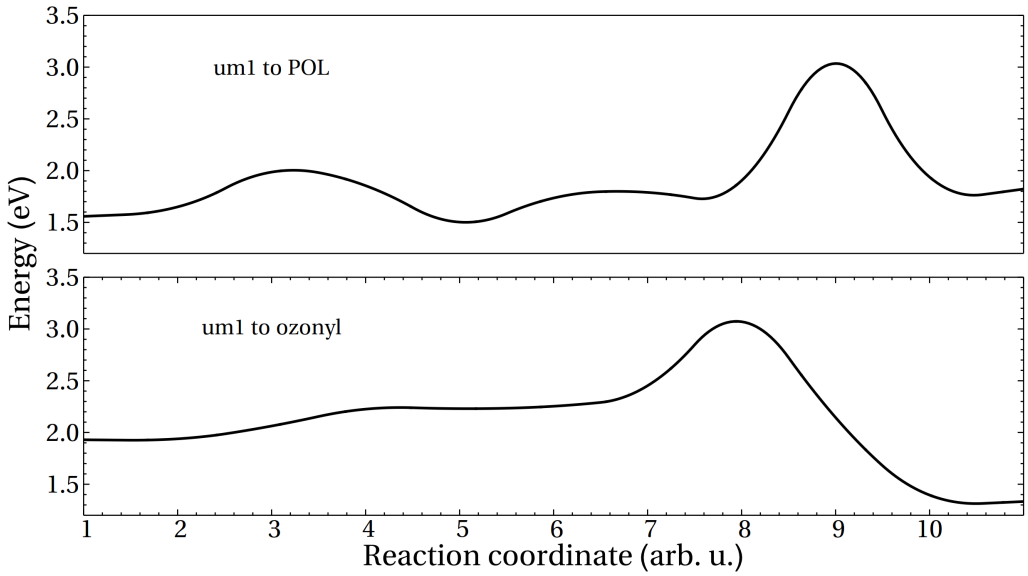

FIGURE 4.29 – Comparison of activation barriers from same initial position into neighboring site, which is in first (upper plot) case non-defective while in second case (lower plot) already contains POL defect.

Overall these results indicate that oxygen release from silica network is favorable through ozonyl defect. In agreement with reference [54] incorporation of oxygen in the form of ozonyl (which does not require breaking of oxygen molecule) is more probable than multiple peroxies. This does however depend on environment because the exposure to irradiation with energy above the dissociation energy of O_2 molecule would greatly change the reaction conditions, in this case each oxygen ion might incorporate into network as POL.

4.2.3 Oxygen deficient centers

ODC(I)

The idea of oxygen molecule being released from peroxy with the formation of vacancy is not new and has been already studied to some extent [98, 99], where barrier of 5.4 eV is reported for release and 0.3 eV for incorporation. As mentioned earlier in reference [27], formation energy of oxygen molecule and two vacancies is 12 eV rendering reaction highly unfavorable.

Configurations have been created with the manual displacement of atoms from peroxy bridge to free gaseous form in adjacent pore (without any obstruction between two configurations) followed by a full relaxation of the cell. Creations of di-atomic vacancies induced varying amounts of the stress depending on the local arrangements of disordered structure, ie. in some cases it creates surprisingly small strain which results only in reconstruction of first few neighboring rings while in other cases it might affect full 108 atom model. In total 5 different configurations

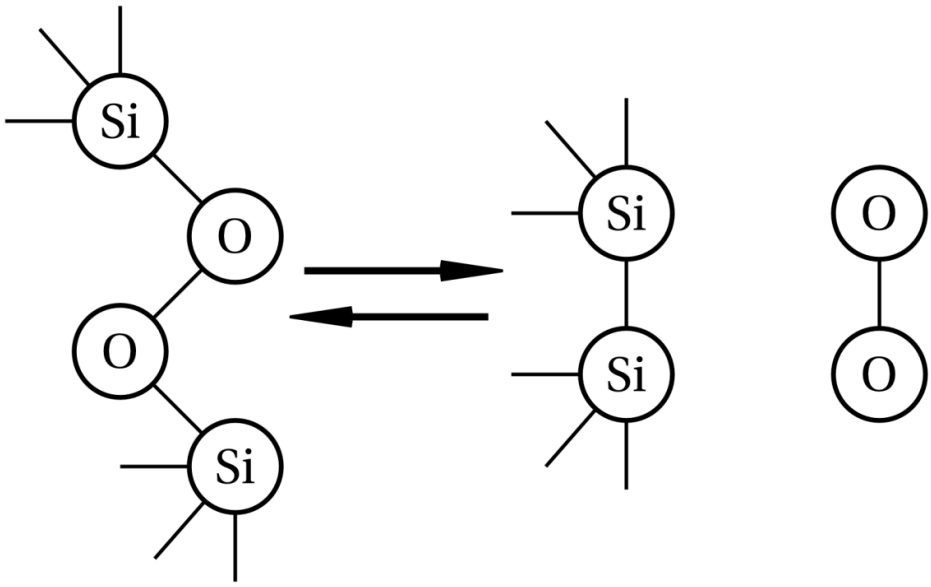

FIGURE 4.30 – Schematic representation of O_2 release from POL defect.

have been analyzed. While this number of defects is not as large as in the case of POL and ozonyl, main goal was to analyze related reactions, and because of high computation costs of NEB approach this number can be considered sufficient. Also static properties (structure, electronic, optical and other) of both defects have already been studied extensively [28, 98, 159].

Results show that formation energy of oxygen molecule released from POL ranges from 5.54 eV to 6.49 eV with average value of 5.97 eV, which is 4.6 eV higher compared to the peroxy defect. Mean Si–Si distance is 2.37 Å, with values ranging from 2.32 to 2.45 Å, which agrees very well with study based on similar approach [51]. Figure 4.31 shows typical reaction barrier for the conversion between POL and O_2 molecule. Reaction path of the release starts with the movement of local defects that increases strain (steps 1-4), which eventually results in cleveage of the first bond (step 6) and then the other (step 7) followed by migration of the molecule and simultaneous relaxation of the network (steps 8-11). Reaction barrier ranges from 3.95 eV to 6.28 eV with mean value of 4.89($\pm$ 0.88) eV. Blue line shows results for barrier simulated without spin polarization, i.e. singlet state, while black line represents results including triplet states. Final energy difference between two states is just above 1eV which provides excellent match with 0.98 eV of excited O_2 molecule in singlet state.

Singlet$\rightarrow$triplet relaxation is again expected to occur with the separation of oxygen molecule from the network in reaction step 7, which in this case corresponds to the singlet saddle point.

However similar reactions have been already described for the cases of quartz and smaller amorphous silica models as described in references [98, 99, 151].

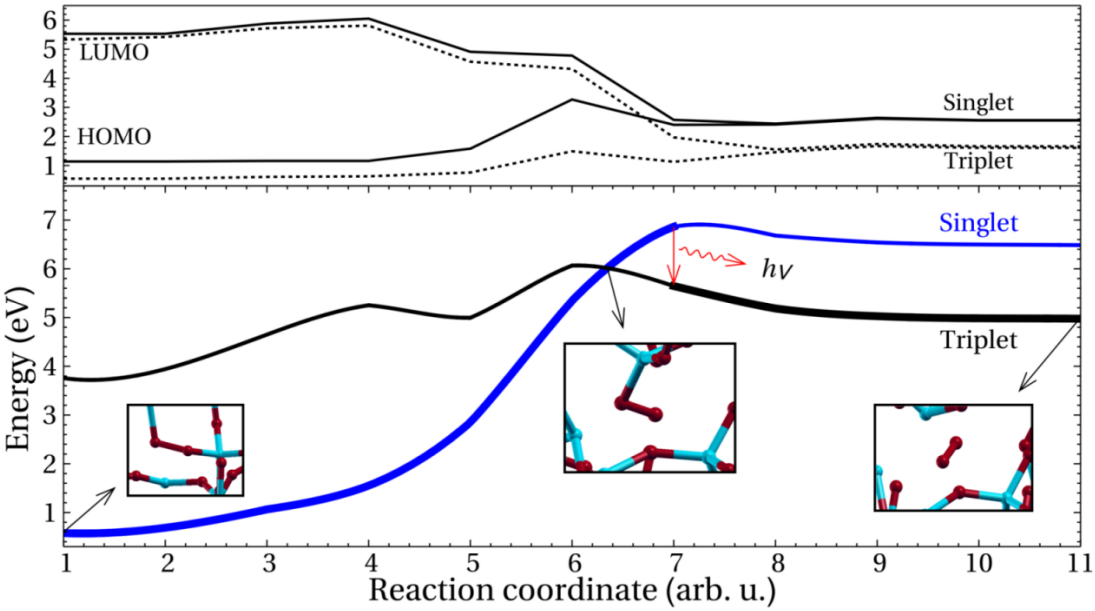

FIGURE 4.31 – Typical energy barrier shape for release of oxygen molecule from peroxy defect. Blue line represents calculations in singlet state and black line in triplet state. Upper part of the image shows energies of HOMO/LUMO states.

Authors report that system switches to triplet state as soon as oxygen bond is broken, which is again proven wrong by the analysis of the electronic structure. Activation energy of this reaction is very high and considering oxygen migration with activation energy below 1.5 eV corresponds to temperatures around 400 °C [2, 55, 57, 106, 107] it is safe to assume this reaction should not produce any light emission because the singlet to triplet relaxation is non radiative as described in the literature [103, 104].

Triplet curve is also not smooth just below the saddle point (depression involving reaction coordinates 4, 5, 6), however because the triplet behavior of network oxygen defects is purely artificial this does not affect any important properties. Results concerning activation energies for this reaction are in fairly good agreement with the references [98, 99].

Activation energies for reverse reaction of O_2 passivating oxygen vacancy using singlet state range from 0.19 to 0.38 eV with mean of 0.28 eV. As in the case of release, incorporation of oxygen must involve switching from ground triplet to excited singlet state. This process is thoroughly described in reference [151], where it is also stated that this is thermally activated process in the case of silicon surface oxidation. However the activation energy of this reaction is very low when the molecule is excited into the singlet state so this reaction should be also photo activated. Oxygen loading of silica samples is usually based on diffusion mechanisms with loading temperatures between 300°C and 500°C, which means the oxygen deficiency defects would become passivated during the loading

experiments.

Results presented in this work show approximately 0.5 eV lower average barrier for release and 0.1eV for incorporation of O_2 molecule compared to [98, 99] (reference studies were performed on a single example). This discrepancy could just be a consequence of sampling size because the values from references lie well within the presented distribution. This again shows importance of statistical approach when modeling amorphous materials.

Large difference in the activation energies has significant implications in the use of excess oxygen in the SiO_2 bases devices. It has been already described that oxygen loading greatly reduces the concentration of oxygen vacancies (both ODC(I) and ODC(II)), which can be expected behavior considering very small barrier [34, 113, 120, 153]. Much larger barrier for breaking of POL into O_2 means that the reaction is unfavorable and the filled vacancy is not only highly stable but also that the another occurrence of similar defect in this position is as likely as any neighboring sites, meaning that with the filling of vacancy short-range local history of defect is lost (assuming local structure is uniform and does not contain any local perturbations).

Formation of dioxagermirane from GLPC

DFT results presented earlier show that dioxasilirane/dioxagermirane defects are stable and total energy of the system containing preexisting ODC(II)/GLPC defect is reduced with the absorption of oxygen molecule and formation of DIOS/DIOG. In this case the NEB simulations have not been performed on typical pure silica model but on Ge-doped silica (1 Si atom has been substituted by Ge atom), where DIOG defect and lone pair have been positioned on germanium atom.

Main interest explaining that this reaction has been studied on Ge-doped model is its greater technological relevance [160] and some very recent theoretical studies on effect of oxygen loading on Ge-doped fibers [113, 153]. As presented in section 4.1.5 the formation energy change between DIOG and GLPC is less than 1 eV, significantly lower compared to $\sim$ 3.5 eV for ODC(II) defect.

Typical reaction barrier is presented in figure 4.32. As it can be seen from the inset images, the reaction starts by rotation of DIOG defect. Two oxygen atoms rotate for approximately 60° before one of the bonds breaks and oxygen becomes briefly bonded in the form of peroxy radical. This rotation of DIOG defects is interestingly compensated by rotation of hosting Ge atom, however after one of the bonds related to defect is broken it starts moving back into its original position. Oxygen remains bonded to the network for two reaction coordinates (6,7) followed by a release from network at the coordinate 8. This can be again

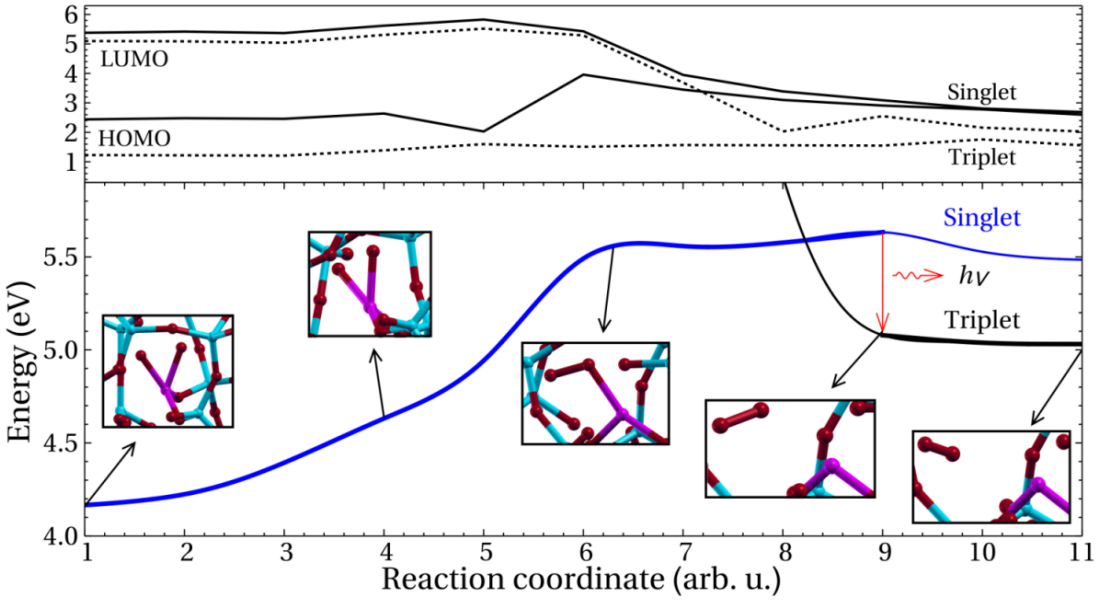

FIGURE 4.32 – Typical energy barrier shape for release of oxygen molecule from dioxagermirane. Blue line represents calculations in singlet state and black in triplet state. Upper part of the image shows energies of HOMO/LUMO states. Blue balls represent Si atoms, purple Ge atoms and red O atoms.

confirmed by analyzing the energies of electronic states visible in the upper part of the figure. Oxygen triplet ground state is identified by degeneracy of highest occupied electronic state. It can be however observed that the states are not completely degenerate, as for example in the case of release from ozonyl (figure 4.24). This can most probably be attributed to the placement of oxygen molecule into smaller interstice, as it has been already proven that the incorporation energy increases for smaller size of pores [107]. Reaction finishes with the relaxation of oxygen molecule into ideal position inside the interstice.

Activation energies for this reaction span from 1.01 to 1.58 eV with average value around 1.3 eV. This activation energy overlaps with known energy required for migration of oxygen in silica [108, 109, 110, 57, 109, 110, 106, 107, 55]. Reverse reaction, which corresponds to the passivation of GLPC with oxygen, has activation energy of just about 0.2 eV (with values spanning from 0.01 eV to 0.6 eV), excluding the oxygen triplet to singlet excitation. Neglecting the excitation energy of oxygen molecule, these results show that DIOG could be readily formed with the presence of oxygen molecule near the GLPC. It should be again noted that only a limited set of configurations has been calculated and this set is not large enough to provide statistically meaningful analysis.

It is generally known that oxygen efficiently passivates GLPC defects [113, 117]. As the experimental loading with oxygen has been based on diffusion processes this means the available energy at that temperature is more than enough for

creation of dioxasilirane. Whether this energy is sufficient for thermal excitation of oxygen into singlet state however remains unknown. For example experimental loading described in ref. [113] has been performed in completely sealed metallic container where no light has been available for photo activated excitation into singlet state, however the GLPC was still completely passivated. On the other hand if the this would be the case two processes (creation of DIOG and release of O_2) could be competing at that temperature, meaning that all of GLPC should not be destroyed.

According to recent studies, the concentration of GLPC in oxygen loaded Ge-doped optical fiber however increases following the electron irradiation, while no such effects have been observed in non-loaded fibers [153]. This clearly shows conversion mechanism of various oxygen species that have reacted with GLPC. Important notation is that these experiments have been performed inside a vacuum chamber in complete absence of light, which can in combination with present results explain why oxygen could not have been re-absorbed into GLPC. Combination of experimental knowledge with new results may be used to design new experiments able to indirectly confirm existence of dioxasilirane.

If DIOG is indeed formed, it should be also noted that at this level no data indicates any reconstruction of network, which could imply that the incorporation might promote system into much more stable configurations, i.e. formation of DIOG preserves the "memory" of defect.

DIOG as intermediate step of network reconstruction

Final reaction presented in this work features previously not known mechanism describing molecular oxygen interaction with GLPC resulting in reconstruction of network.

Experimental data clearly shows the oxygen loading is able to completely annihilate lone pair centers, however actual processes behind these mechanisms remain completely unknown [113, 117]. Dioxasilirane/dioxagermirane is one of the most obvious candidates and it has been already shown that it can be easily formed when oxygen interacts with GLPC/ODC(II). Recent theoretical study has however shown that ODC(II) and GLPC are not actually double oxygen vacancies (usual historical depiction of these defects) but rather different forms of oxygen mono-vacancies [30]. As the oxygen loading has been performed using diffusion mechanisms at temperatures around 500 °C, it can be assumed that combination of excess oxygen and temperature should be able to reconstruct the network, similarly to how oxygen molecule can easily passivate vacancy and form peroxy defect (section 4.2.3). This reaction should however be more complex as GLPC generation has been shown to involve advanced "rotation" and "puckering"

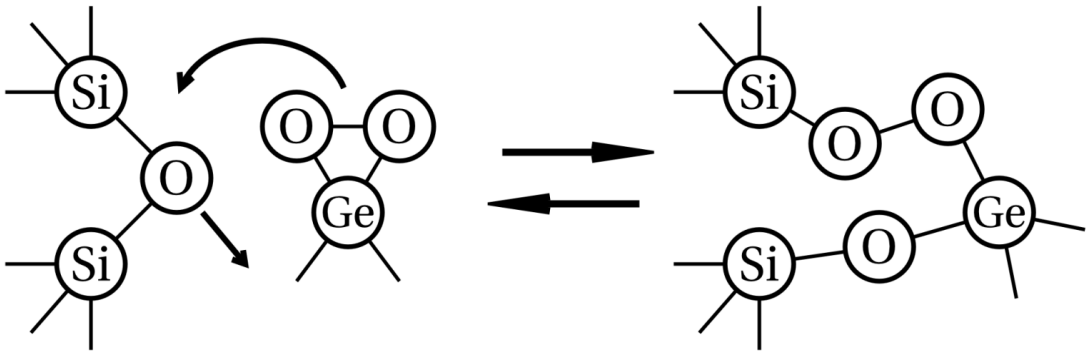

FIGURE 4.33 – Schematic representation of network reconstruction after the passivation of a GLPC by an oxygen molecule (with the intermediate formation of a dioxasilirane) and further relaxation.

mechanisms.

Relevance of network reconstruction mechanism following interaction between O_2 molecule and GLPC is highlighted by the fact that multiple approaches, specifically structural relaxation of DIOG and NEB simulation of oxygen release from DIOG, have both been able to independently produce reconstruction of the network. In some cases (around 15%) DIOG could not be even formed as structural optimization directly resulted in network reconstruction. Comparing the formation energies between reconstructed network configurations and their corresponding DIOG configurations shows that the latter have, on average, 1.5 eV higher formation energy, with values ranging from 1.03 and 2.05 eV. Formation energies have been simply calculated as a difference between total energies of both configurations.

Schematic representation of this reaction can be seen in figure 4.33. Reconstruction mechanism is in principle very similar to proposed ODC(I) and ODC(II) conversion channel presented in reference [30]. Oxygen bond from Si–O–Si breaks and bonds with the neighboring GLPC site, while two oxygen atoms forming dioxasilirane fill the created gap with the formation of peroxy bridge.

Contrary to other presented mechanisms, dynamics of this reaction have unfortunately not been properly addressed. Preliminary calculations (not shown) however indicate the activation barrier should be lower than 1 eV, which is easily accessible with diffusion based oxygen loading [113, 117]. Moreover this mechanism should be able to completely remedy structural memory of pre-existing GLPC defect so any further treatments would not be able to regenerate it, similarly to what has been observed in irradiated oxygen loaded Ge-doped fibers [113, 117]. Latest experimental studies also indicate that the oxygen is most probably incorporated into network in the form of peroxy bridges [45].

4.2.4 Comparison with available experiments

The results of the presented study on the activation barriers for various oxygen excess related defects could be used for better understanding of relevant experimental data. One of most suitable experiments has been performed by Skuja *et al.* and is thoroughly described in reference [44]. This article describes experiment where oxygen rich bulk silica sample was initially irradiated with UV laser ($h\nu$=7.9 eV) at low temperature (80 K) and then annealed at different temperatures while measuring intensity of O_2 photoluminescence, from which the concentration of molecular oxygen was calculated. During subsequent annealing the authors observed that the initial oxygen concentration was restored in three steps. In the first step between 80 K and 180 K 3% of initial concentration has been restored. This recovery has been accompanied by a strong PL emission at 1272 nm, which is the well known oxygen singlet-to-triplet transition band. Majority (85%) of initial oxygen concentration has been restored in a second step between 470 and 670 K while the remaining 10% were restored between 870 and 1070 K. All of the annealing times at higher temperatures were performed for 15 min, however no data is unfortunately presented for the first observed reaction at 180 K.

A combination of experimental data and calculated activation energies could be used to accurately assign chemical reactions to different steps of the experiments. In order to properly understand the dynamics first order rate equation have been considered in combination with Arrhenius law describing the relation between reaction rate and activation energy [5]. Application of Arrhenius law for reactions involving solid state reactants has been widely debated [161]. While many derivations exist for solid state problems, they are primarily focused on the surface reactions. In this regard general Arrhenius law appears more pertinent for the case of reactions involving oxygen molecules diluted in the solid matter.

First order rate equations are only able to describe reactions with one reactant, ie. no back conversion mechanisms are considered.

$$\frac{\mathrm{d}C_{\mathrm{defect}}}{\mathrm{d}t} = -kC_{\mathrm{defect}} \tag{4.5}$$

with k being the reaction rate coefficient and C_{defect} the concentration of the defects. Solution has the form of exponential decay equation :

$$\frac{C_{\mathrm{defect}}(t)}{C_{\mathrm{defect}}(0)} = e^{-kt} \tag{4.6}$$

with k defined by Arrhenius law :

$$k = \Gamma e^{-E_a/k_b T} \tag{4.7}$$

Γ is the Arrhenius pre-exponential factor, E_a the activation energy, k_b the Boltzmann constant and T the temperature. Value Γ is probably the most debated parameter of Arrhenius equation describing solid state reactions, as it is known to spread wide range of values (10^7-10^{14}) with more dominant region between 10^{11}-10^{13} [162]. In this work a value of $5 \cdot 10^{13}$ s^{-1} has been adopted, as it has been shown to describe reactions in silica with moderate success [163].

During the first step of referential experiment [44] approximately 3% of oxygen concentration has been restored at 180 K. Unfortunately the time of this temperature step was not specified, however considering the whole experiment it can be considered that all of the treatments were isochronal at 900 s. Nevertheless various times have been used for better representation of the data. Figure 4.34 shows concentration of unknown network oxygen specie that was released at 180 K following the 7.9 eV laser irradiation at 80 K as a function of activation energy. Considering that no change has been observed when temperature has been further increased it is clear that all of these species have been destroyed at this temperature. This means the activation energy of this reaction can be safely assumed to be below 0.55 eV. If this temperature has been preserved for less than other annealing steps, the activation energy should be lower, approximately 0.52 eV for annealing time of 60 s and 0.45 eV for 1 s, however this annealing time appears unrealistic for such experiment. Finally the effects of different pre-exponential factors are considered. Dashed lines show that changing this factor by an order of magnitude has minor effects resulting in shifts of activation energy by approximately 0.02 eV.

Activation energy for release of oxygen molecule from ozonyl bridge presented in this work spans between 0.44 eV and 1.35 eV. As it has already been stated, length of calculations resulted in a limited set of activation barriers, which are not able to accurately describe a distribution, however these barriers can be used to estimate the magnitude of E_a. In this case the lower activation energies for release of oxygen from ozonyl are the only candidate for this reaction. Experimental data also show that only 3% of oxygen was incorporated in the form of ozonyl defect. This is a reasonable observation considering that the formation energy of ozonyl is higher than presumably most common oxygen excess network defect, POL. Another important observation is that this activation energy implies that ozonyl defect is not stable at room temperature. This can be supported by the fact that its existence has not been confirmed by any experimental data, i.e if the experiments are performed at room temperature the ozonyl cannot be detected as it has already

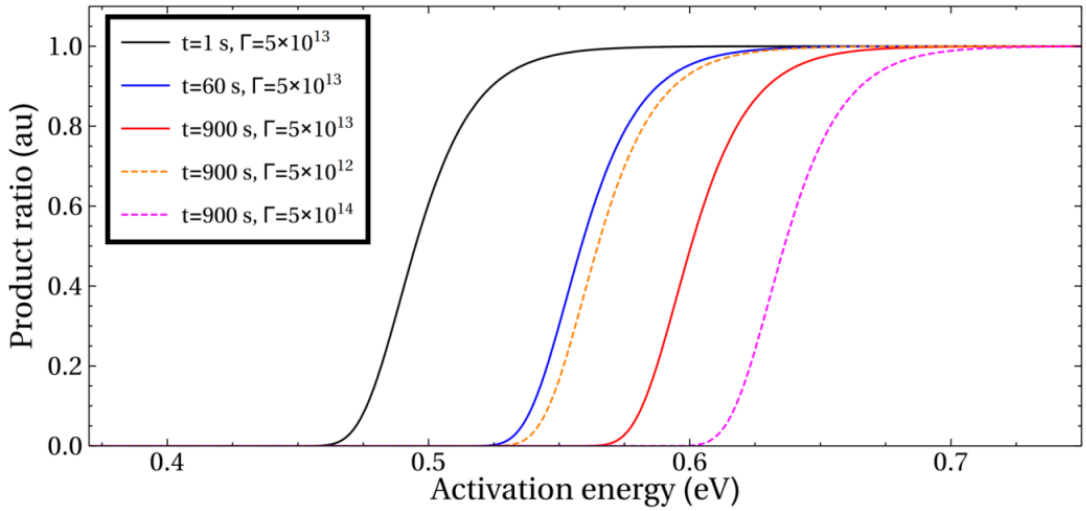

FIGURE 4.34 – Concentration of network oxygen species that were released at 180 K following the F_2 laser irradiation at 80 K (as described in reference [44]) as a function of reaction's activation energy.

been dissolved. On the other hand its first proposition as intermediate step in oxygen exchange reactions appears correct [54]. Finally, results from simulations are able to accurately predict the oxygen singlet to triplet relaxation following the release from the network in agreement with the experiments.

In the second step of the experiment, 900 s long annealing at 670 K resulted in almost complete recovery of oxygen [44]. Authors concluded the major contributing reaction was the diffusion of interstitial oxygen atoms, most probably in the form of peroxy bridges. Assuming diffusion parameters of molecular oxygen the activation energy has been estimated to around 1.3 eV in good agreement with the literature.

With known annealing time the activation energy of this reaction can be again calculated. Results show the activation energy for this reaction should be lower than 2.1 eV (figure not shown, very similar to figure 4.34). Considering that no oxygen has been recovered during annealing at 200 °C (470 K), a lower limit for this reaction can be determined at 1.6 eV. No luminescence has been observed during these annealings, however intensity of PL emission has been observed to decrease with temperature and becomes practically invisible above 300 °C [61, 104].

Considering that oxygen has been irradiated with F_2 excimer laser at temperatures much lower than diffusion barrier (activation barrier above 1.3 eV corresponds to temperatures higher than 470K [34, 44], it can be assumed oxygen has incorporated into vacant sites. Results for diffusion of near peroxy bridges show the activation energies range from 1.46 to 1.93 eV, which is again in good agreement with experimental data. Using the oxygen molecule diffusion parameters yielded smaller activation energies (around 1.3 eV). Migration energy for diffusion

Table 4.7 – Comparison of experimental data from reference [44] and calculated activation energies using first order rate equations and Arrhenius law for activation energy.

Measured O_2 concentration	Temperature (K)	Activation energy (eV)
2%	80	/
≈5%	180	< 0.55
90%	670	1.6 -2.1
100%	870-1070	3.0 - 3.5

of molecular oxygen based on first principles methods has been estimated to around 1.1 eV [107]. Combination of these results show that migration through interstitial species is energetically less favorable compared to O_2, however it should be considered an important mechanism following the irradiation treatments of oxygen rich samples.

Last step, in which the final 10% of initial oxygen is recovered, occurs after a 15 min annealing at 800 °C. Considering no recovery has been observed prior, activation energy of this process can be estimated between 3.0 and 3.5 eV. Origin of this reaction does not only remain unknown but there are also no candidate defects. It appears to be generated following the radiation induced dissociation of oxygen molecules.

Finally, data from experiments [44] is summarized in table 4.7 for better representation.

More recent similar study provides more accurate data regarding oxygen excess processes in silica [45]. Dynamics were studied on higher level thanks to loading with isotope labeled oxygen which granted further insight to exchange processes. Additionally, concentrations of radicals have been measured thanks to the use of EPR. This study not only reports that ozone is created following the irradiation at 77 K (irradiation parameters have been deliberately chosen to maximize production of ozone while minimizing the generation of NBOHC) but also that it remains stable until the temperature above 100 °C after which it dissociates. This result is not in absolute agreement with previous work where no oxygen recovery has been observed at such temperatures. Results regarding the diffusion of interstitial species remains constant with previous experiments and consequently this work. Interestingly the oxygen exchange reactions between gaseous and network species is reported for much lower temperatures in irradiated samples (200-500 °C) compared to non-irradiated silica ($<$ 700 °C). Furthermore, initial oxygen recovery process is reported to complete around 500 °C and there are no indications for any recovery at higher temperatures as reported in first

experimental study. Exchange reactions between network and gaseous oxygen is nevertheless still considered to occur through the ozonyl defects.

4.3 Experimental measurements on O_2 loaded fibers

The Last section of this work is dedicated to the presentation of experimental results on oxygen loaded optical fibers by comparison to their non-treated counterparts. All of the work presented has been performed in the Laboratory Hubert Curien of University Jean Monnet in Saint-Étienne, France.

Experiments have been performed on oxygen loaded optical fibers irradiated at different temperatures in order to characterize their responses and identify some of the created defects. Main characteristics of tested samples have already been summarized in the table 3.1.

In all experiments pristine and oxygen loaded fibers have been placed alongside (separated by approximately 1 cm which changed dose rate by less than 1%) at a distance of approximately 28 cm from Moperix X-ray source resulting in absorbed dose of ∼4.15 Gy(SiO_2)/s at room temperature (23-25 °C) and at high temperature (∼300 °C) for 7200 seconds resulting in total absorbed dose of 30 kGy. Temperature of heating plate varied by ± 5 °C while temperature inside irradiation chamber increased from 23 °C to 27 °C at the end of irradiation and returned to initial temperature approx. 2 hours after the experiment.

Radial distribution of defects has been studied using CML experiments. Oxygen loaded fibers have been compared to unloaded reference fibers for all treatments which include combinations of irradiation at room/high(300 °C), temperature and heating.

4.3.1 Pure silica fibers

Fiber with pure silica core and F doped cladding (titled SiD1) has been studied first as its radiation response is expected to be dominated by well known defects [160]. Length of irradiated fibers was 133 mm and 103 mm for pristine and O_2 loaded fiber respectively.

Figure 4.35 shows radiation response at different doses for pristine (left) and oxygen loaded fiber (right). In both samples RIA is characterized by clear peak around 2 eV and stronger absorption in UV region. It appears the radiation response is more linear for pristine fiber, while oxygen loaded fiber starts showing signs of defect growth saturation above 10 kGy. Kinetics of defects under irradiation are controlled by two competing mechanisms, formation generation and bleaching.

High temperature is more likely to affect the bleaching mechanisms. It has been shown in previous section (4.2.4) increased temperature corresponds to higher activation energy and faster reaction rates of reactions, which would both increase the speed of recovery [160].

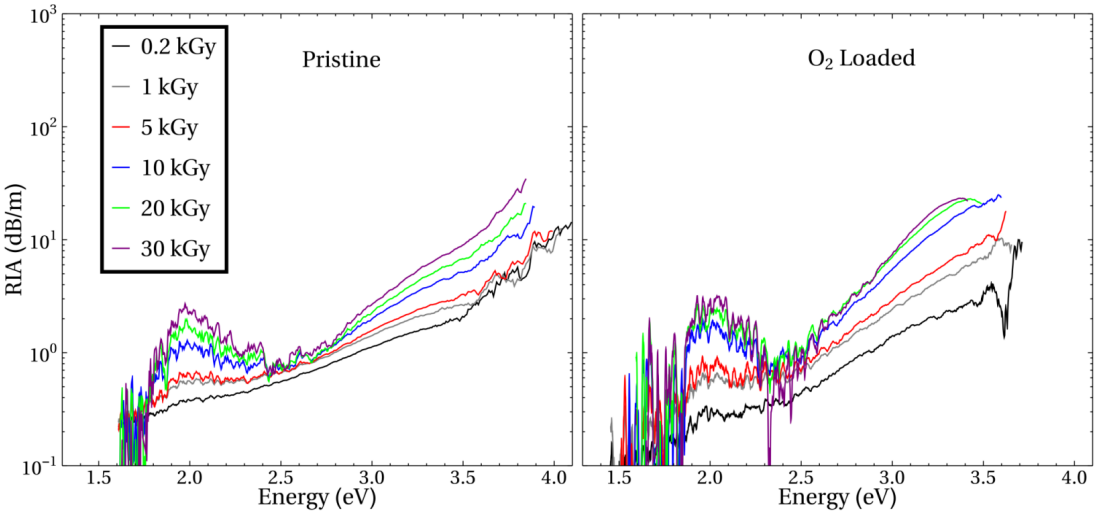

FIGURE 4.35 – Radiation induced attenuation of pristine/O_2 loaded SiD1 OF under X-ray irradiation at several doses at ∼300 °C. Dose rate is 4.15 Gy/s.

First feature is clearly visible peak with energy around 2 eV. Intensity of this peak appears to be pretty similar in both pristine and oxygen loaded sample.

According to present literature [2, 21, 34, 160] main optical absorbers in this domain are NBOHC (2 eV) and presumably POR (1.97 eV). Since the intensities of this peak are similar in both pristine and loaded fibers, this hints its origin is more probably NBOHC because the contribution of POR in loaded fiber would probably be stronger (if this band is indeed related to POR).

For both cases the strongest response is observed above 3 eV. According to older study performed on similar samples at room temperature [164] this peak can be attributed to presence of chlorine impurities and tails of stronger ODC(II)/NBOHC absorptions. NBOHC is one of the characteristic oxygen excess defects so its concentration is expected to be higher in oxygen rich fiber [77, 78, 79], however the similar intensity of 2 eV peak does not support this statement. This feature however clearly shows stronger attenuation in oxygen loaded fiber with all light being absorbed above 3.5 eV. Previous results show that the NBOHC concentration of $\sim 5 \cdot 10^{16}$ correspond to the losses of approx. 2 dB/m [2, 160]

Both of these defects are undoubtedly connected to irradiation [78, 113, 164]. Figure 4.36 shows the growth kinetics of the RIA at two particular energies 3.25 eV and 1.96 eV as a function of the deposited dose in pristine and O_2 loaded fibers. These wavelengths have been chosen to highlight the NBOHC behavior (probed by 1.96 eV band) and the mixed contribution of defects absorbing in the

UV (NBOHC and chlorine related species). For both energies initial attenuation is stronger in pristine fiber, however after absorbed dose in order of few hundred Gy the attenuation becomes stronger in O_2 loaded fiber. Two growth rates can be observed for the 1.96 eV band of NBOHC in pristine fiber : First regime is characterized by slower growth up to ∼6 kGy after which the generation rate increases. In the case O_2 loaded fiber this behavior cannot be so clearly identified as the growth becomes more distorted after ∼6 kGy. Overall the NBOHC induced attenuation only increases by ∼30% in loaded fiber when compared to pristine fiber.

Initial attenuation at 3.25 eV behaves similarly to NBOHC (highlighting that this defect has probably a major contribution to the RIA in this spectral domain and at this dose range). Up to absorbed dose of ∼100 Gy the losses are smaller in loaded fiber followed by an inversion after which attenuation in loaded OF becomes stronger. Overall the radiation response of this band is much more intense in oxygen loaded fiber (by ∼3×) and the growth rate appears constant regardless of absorbed dose. Low initial attenuations for both analyzed bands in the loaded fiber could indicate that oxygen efficiently bleaches pre-existing defects related to those bands.

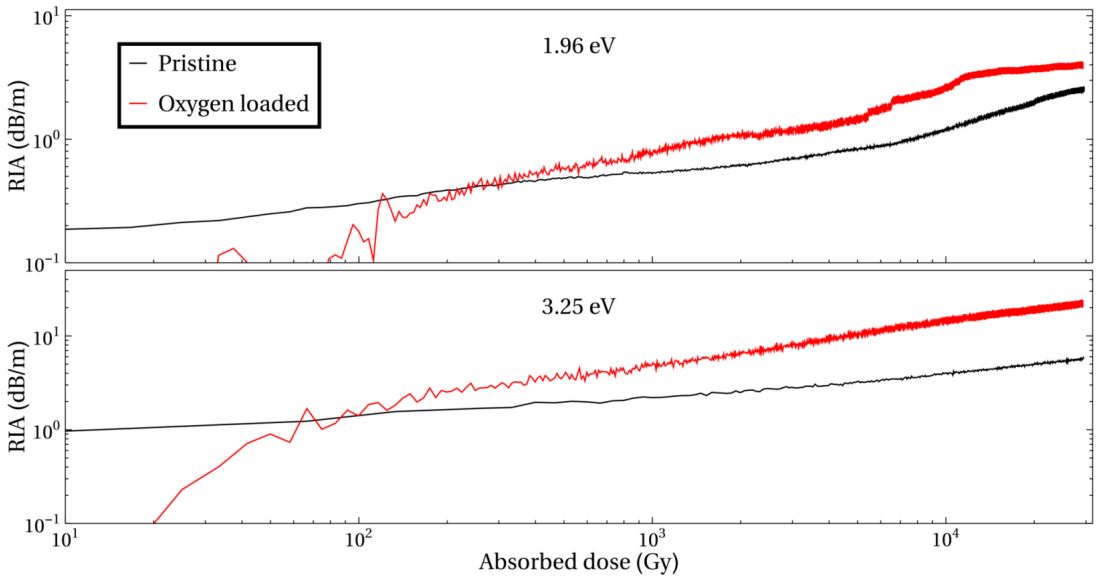

FIGURE 4.36 – Radiation induced attenuation growth at 1.96 eV and 3.25 eV of pristine/O_2 loaded SiD1 OF as a function of absorbed dose at ∼300 °C. Dose rate is 4.15 Gy/s.

Figure 4.37 shows the decrease of radiation induced attenuation after the irradiation (commonly referred to as recovery) as the temperature of fiber decreases from 300 °C to room temperature. Overall this figure shows that the absorbed dose of 30 kGy at 300 °C is followed by weak recovery without particular characteristic features. Recovery appears more evident in oxygen loaded fiber, however at this

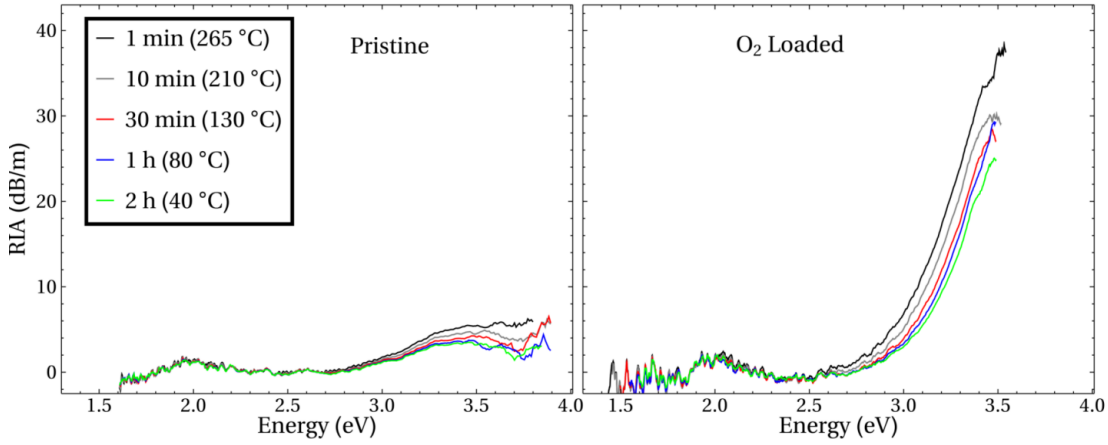

FIGURE 4.37 – SiD1 OF recovery from 300 °C to room temperature (approximately 2 hours) after 30 kGy irradiation at 300 °C.

point it is practically impossible to decompose recovery into contribution from actual radiation damage recovery and change of fiber guide losses as a function of temperature [1].

Radial distribution of defects has been studied using CML experiments and the results are presented in figure 4.38. Only concentration of NBOHC defect can be measured in pure silica fiber in this region thanks to its strong PL emission band at 1.91 eV.

Vertical dashed line indicates interface of core and cladding. Results show that concentration of NBOHC is very low for all non-irradiated samples, ie. not only untreated pristine and oxygen loaded fibers but also samples that were heated to 300 °C. It should be noted that the oxygen loading has been performed at even higher temperature (∼500 °C) so another heating to 300 °C is not expected to activate any further defect generation and conversion mechanisms. Pure silica fibers are known to exhibit strong radiation resistance [2, 34, 160] as the concentration of NBOHC in irradiated fibers remains relatively low and is actually comparable to non-irradiated samples even at high temperatures [165, 166]. Most changes can be observed in irradiated O_2 loaded fibers. In the case of loaded fiber irradiated at room temperature the increase of NBOHC concentration can be observed in the outer core (10-30 µm from the center) while in the central part of the core it remains low.

Combination of high temperature and irradiation promotes NBOHC formation the most. In the case of pristine fiber irradiated at high temperature concentration of defects appears to be relatively stable in the cladding while it slowly increases towards the center of the fiber. Higher concentration of NBOHC is created in loaded fiber irradiated at high temperature. Compared to fiber irradiated at room temperature there is noticeably stronger generation in the central part of the

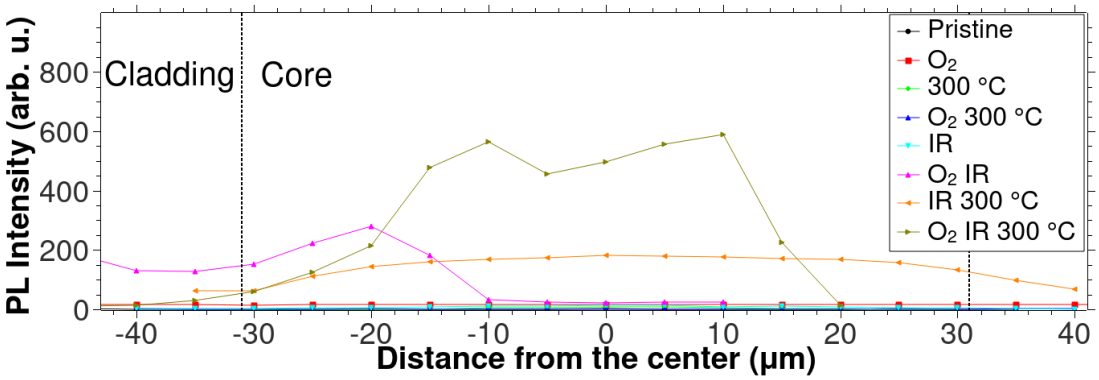

FIGURE 4.38 – CML cartographies of NBOHC emission at 1.9 eV in SiD1 OF after various treatments. Vertical dashed lines indicate interface between core and cladding.

core (±15 µm from the center) while concentration quickly decreases towards the cladding. These results show relatively small increase of NBOHC PL band intensity in oxygen loaded fiber compared to pristine fiber, which can be also observed on the RIA spectra (figure 4.35). In the case of oxygen loaded fiber irradiated at high temperature a small decrease of NBOHC emission can be observed in the center of the fiber core. This is probably related to the presence of small amount of fluorine in this region as shown for this fiber in reference [167]. Interestingly the spatial distribution of NBOHC does not follow the general core/cladding structure. One explanation of this behavior could be stepped core/cladding interface, however chemical analysis had shown that this is not the case as core/cladding are separated by sharp increase of F-doping in the cladding. As such behavior is more obvious in oxygen loading fibers it would be also possible that the oxygen concentration is not uniform, but this has been already shown to not be the case [113]. Observed degradation of NBOHC might be related to the strain distribution in the optical fiber, with a noticeable contribution of NBOHC generated from strained Si–O–Si bonds as discussed in [168].

4.3.2 P-doped fibers

PD1 OF has two step P-doped core and pure silica cladding (7.6 and 3.0 wt% for inner/outer core respectively as presented in table 3.1). Its RIA response is shown in the lower part of figure 4.39 while the upper part represents kinetics of 2.25 eV band. Length of irradiated sample was 180 mm for pristine and 162mm for oxygen loaded fiber. Similarly to related study performed at room temperature [113] it is characterized by strong radiation induced absorption between 3.1 eV and 1.8 eV. According to reference study [113] these peaks are caused by stable (2.25 eV) and metastable (3 eV) POHC defects with some contribution from oxygen

excess related defects. Regarding the defect creation kinetics it can be observed that the growths for pristine and oxygen loaded fiber is practically identical at lower doses after which the RIA becomes stronger in loaded fiber leading to the saturation. For oxygen loaded fiber the defects seem to be created at much faster rate as the signal pretty much diminishes at 1 kGy with the exception of small peak just above 2.5 eV. At higher doses radiation induced defects absorb all light with energy higher than 1.9 eV. It should also be noted that the irradiated samples were relatively long. Oxygen loading however appears to have positive effect on absorption tail around 1.5 eV, where absorption seems to be stronger in pristine OF. Upper part of the figure shows kinetics of 2.25 eV band origin from POHC defect [113]. Concentration of this defect is initially lower in O_2 loaded fiber but after absorbed dose just below ∼1 kGy RIA becomes stronger compared to pristine fiber. Growth appears to saturate above 1 kGy for both loaded and pristine fiber. Such behavior has been already observed for the pristine fiber [113].

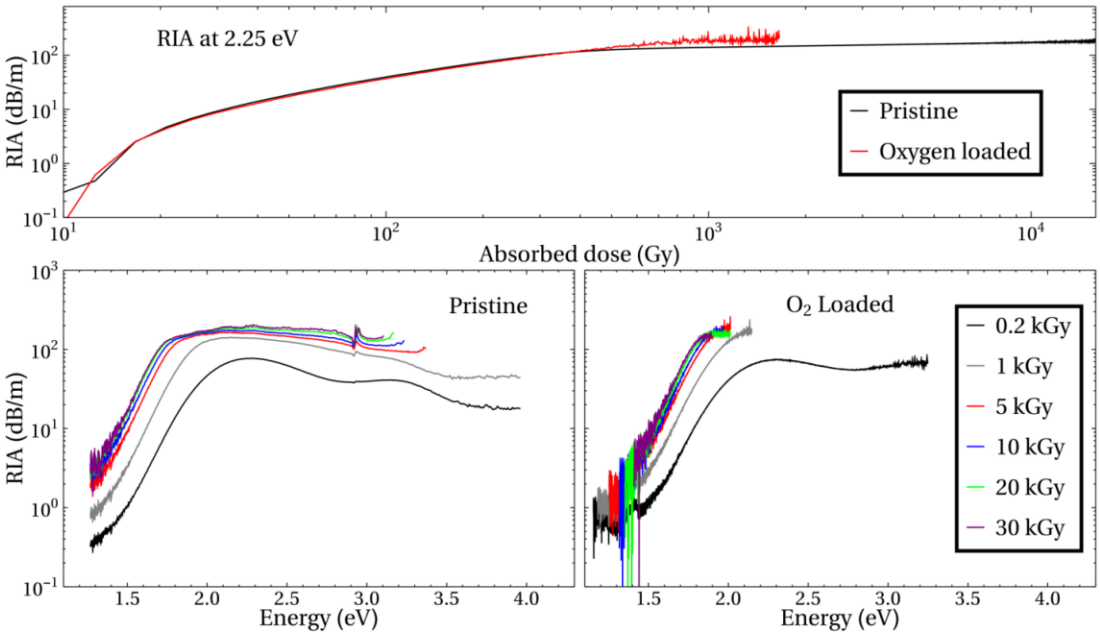

FIGURE 4.39 – RIA of PD1 OF under X-ray irradiation at several doses at ∼300 °C. Dose rate is 4.15 Gy/s.

Comparison with the study in reference [113] shows that the overall trend of defect generation is pretty similar with the higher temperature used in present study greatly promoting defect generation ratio. For example, reference study shows signs of defect growth saturation at approximately 130 kGy for pristine fibers while at high temperature similar phenomena can be already observed at 5 kGy. At room temperature generation rate difference between pristine and loaded fibers seems rather small (mostly related to excess oxygen defects) [113], however at high temperatures the generation rate of defects in loaded fibers is much higher.

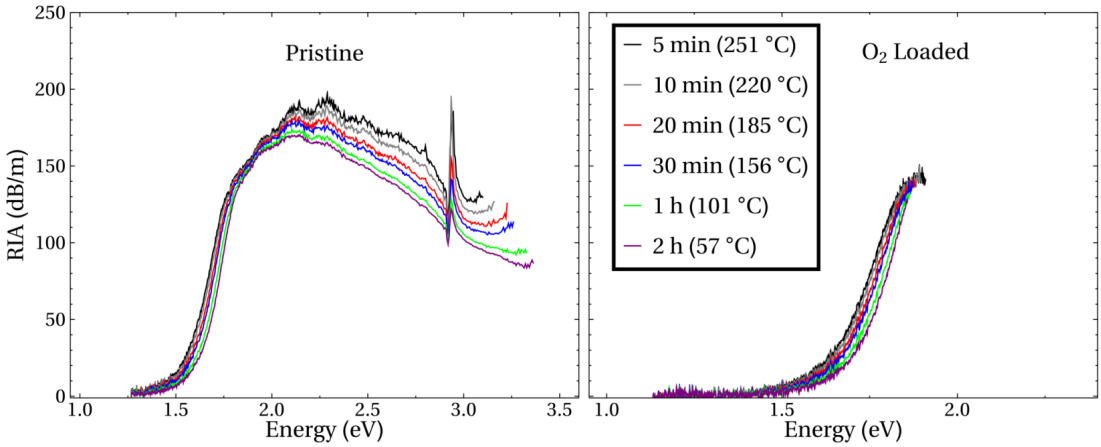

FIGURE 4.40 – Recovery from radiation induced damage in PD1 fiber after being irradiated with dose of 30 kGy.

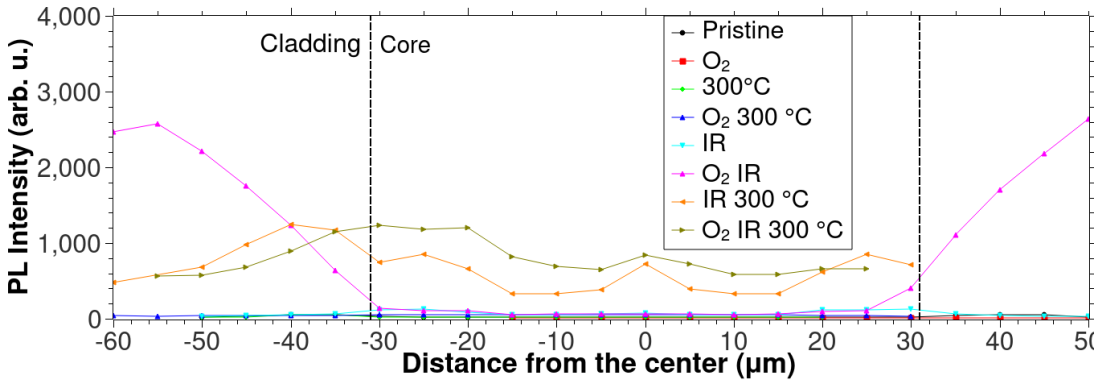

FIGURE 4.41 – CML cartographies of NBOHC emission at 1.9 eV in PD1 OF after various treatments.

Radiation damage recovery dynamics are presented in figure 4.40. Similarly to ref. [113] pristine fiber shows two areas of recovery, weak around 2.5 eV domain and stronger in the absorption tail between 1.7 eV and 1.5 eV which again points out different dynamics of stable and meta stable POHC defects. Due to the absence of signal at lower wavelengths only second domain is observed in the loaded fiber. Recovery appears to be affected by two mechanisms, actual defect recombination and temperature effects on waveguide.

PL study of NBOHC distribution after different treatments is presented in figure 4.41. Similarly to study [113] only very narrow peak around 1.9 eV has been included in the results. In agreement with present knowledge [9, 160] the NBOHC concentration is pretty low in un-irradiated fibers. In the case of fiber irradiated at room temperature only a small increase can be observed at the core/cladding interface. Similarly to pure silica core fiber (figure 4.38), when oxygen loaded fiber is irradiated at room temperature the concentration of NBOHC greatly increases in the cladding This is particularly interesting as SiD1 fiber has F doped cladding and pure SiO_2 core, while P doped fiber has pure silica cladding

but the behavior appears to be very similar. Most NBOHC defects are again created under irradiation at high temperatures. It appears that most NBOHC defects are generated on the core/cladding interface, however in the case of oxygen loaded fiber defects are generated more towards the core while pristine fiber favors generation of defects towards the cladding. In both cases there is a small peak visible directly in the center of fiber, where, according to electron micro probe analysis (EMPA) [113], the concentration of P is lower. In general it appears that P-doping suppresses generation of NBOHC [153, 169].

4.3.3 GeCe doped fibers

Core of GeCeD1 fiber is Ge doped with Ce as co-dopant while the cladding is pure silica. RIA and kinetics of 1.7 eV band measured at 300 °C for this fiber are shown in figure 4.42. Length of irradiated samples were 140 mm and 101 mm for pristine and O_2 loaded samples respectively. First observation, which has also been described in reference [113], is that the Ce doping greatly increases optical absorption in visible/UV domain meaning no light is transmitted above 2.75 eV in pristine and 2.1 eV in O_2 loaded fiber. In this sample presence of oxygen excess increases attenuation across whole measured domain including the IR region. Again the RIA growth appears to be linear for lower doses (up to 10 kGy) after which signs of defect formation saturation become evident. Comparison with RIA experiments at room temperature [113] shows that high temperature significantly promotes the defect generation rate. Recovery after irradiation is not visualized as both pristine and oxygen loaded fiber are characterized by weak linear recovery across whole measured spectral domain. Growth of RIA at 1.7 eV is uniform for both fibers with the oxygen loaded being approximately an order of magnitude higher. At doses above 10 kGy the pristine fiber shows clear signs of growth saturation, however the RIA in loaded fiber continues to increase until light is no longer transmitted at this energy around 20 kGy.

Results from CML study of 3.4 eV PL peak associated with Ce^{3+} emission center are presented in figure 4.43. Most important observation concerns oxygen loading for which it can be seen that it completely bleaches out Ce^{3+} emission centers. Rare earth co-dopants are particularly interesting in technological applications because of their strong emission characteristic, which are obviously destroyed by introduction of oxygen molecules. When oxygen is not present these centers show relatively strong resistance to irradiation, for example absorbed dose of 30 kGy at room temperature annihilates approximately 10% of centers while additional ∼10% are destroyed when irradiated at 300 °C with the same dose.

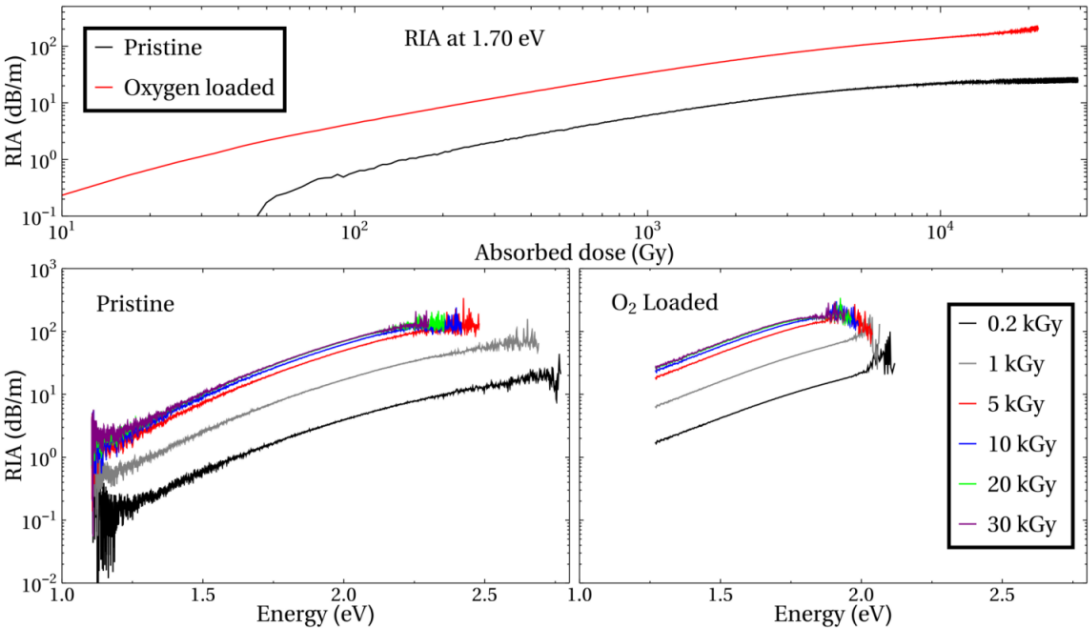

FIGURE 4.42 – RIA of GeCe doped optical fiber under X-ray irradiation at several doses at ∼300 °C. Dose rate is 4.15 Gy/s.

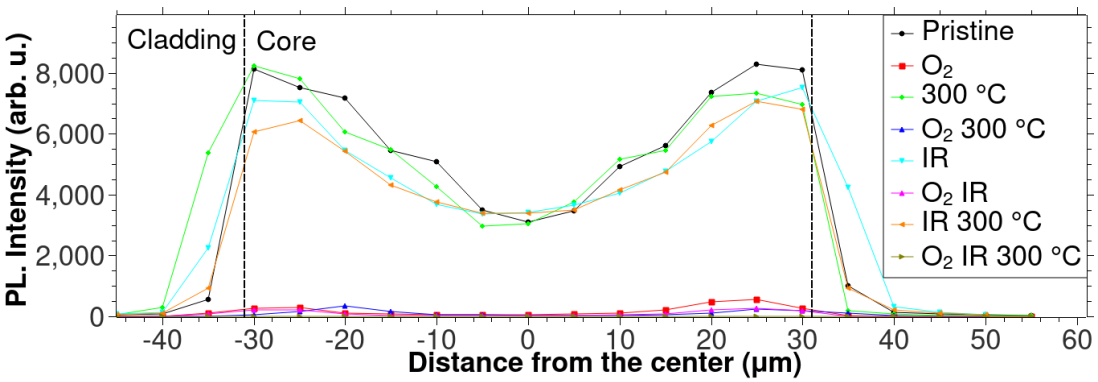

FIGURE 4.43 – CML cartographies of Ce^{3+} emission at 3.4 eV in GeCe OF after various treatments.

4.3.4 PCe doped fibers

Room temperature

While the optical response of irradiated PCe pristine fiber has already been published [113], no such study exist for fiber loaded with oxygen. Lengths of irradiated samples were 61 mm for pristine and 56 mm for loaded fiber. RIAs of PCe fibers are presented in figure 4.44. Again presence of Ce ions is responsible for strong absorption in UV/visible domain. Results for non-loaded fiber are consistent with literature (reference [113]), which show linear growth even for high doses. Oxygen loading seems to have two effects on RIA, first the attenuation appears to be lower. This is relatively surprising effect as presence of oxygen generally appears to have negative effect on radiation resistance of fibers. Secondly, the growth rate at higher doses slows down meaning that excess O_2 appears to be responsible for faster saturation of defect growth rate. Results for recovery after irradiation are not shown as this fiber shows no sign of recovery in observed spectral domain. RIA growth of 2.25 eV (POHC center) shows almost identical growth for both fibers, however light with this energy is no longer transmitted at doses close to 10 kGy.

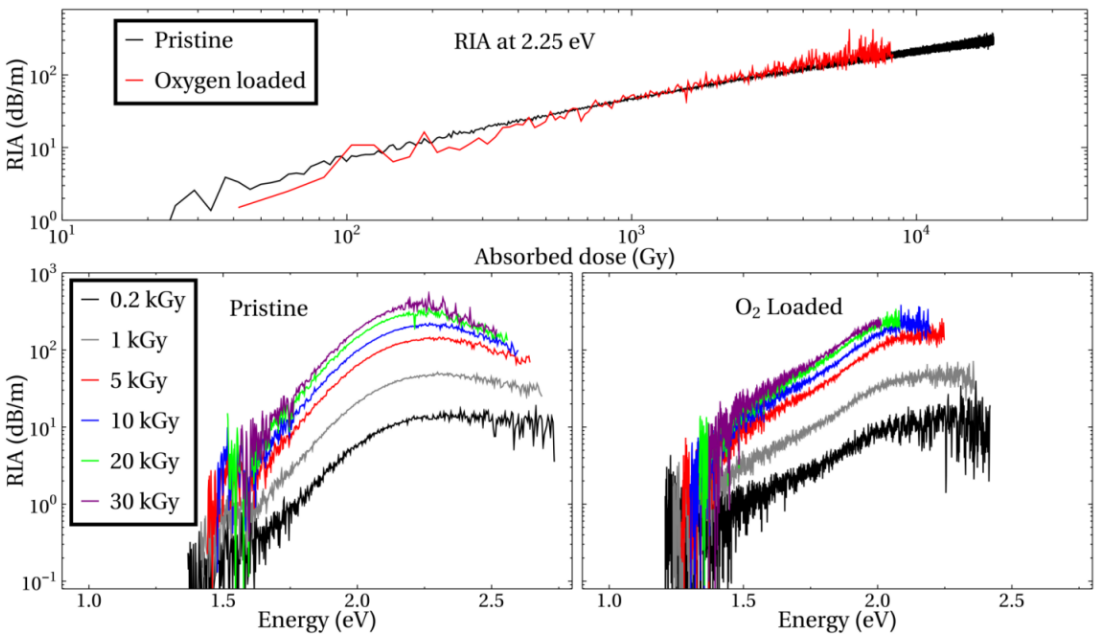

FIGURE 4.44 – RIA of PCe doped optical fiber under X-ray irradiation at several doses at room temperature (∼23 °C). Dose rate is 4.15 Gy/s.

High temperature

Radiation response of PCe fibers at high temperature has been measured on 102 mm pristine sample and 81 mm long oxygen loaded fiber. This OF exhibits

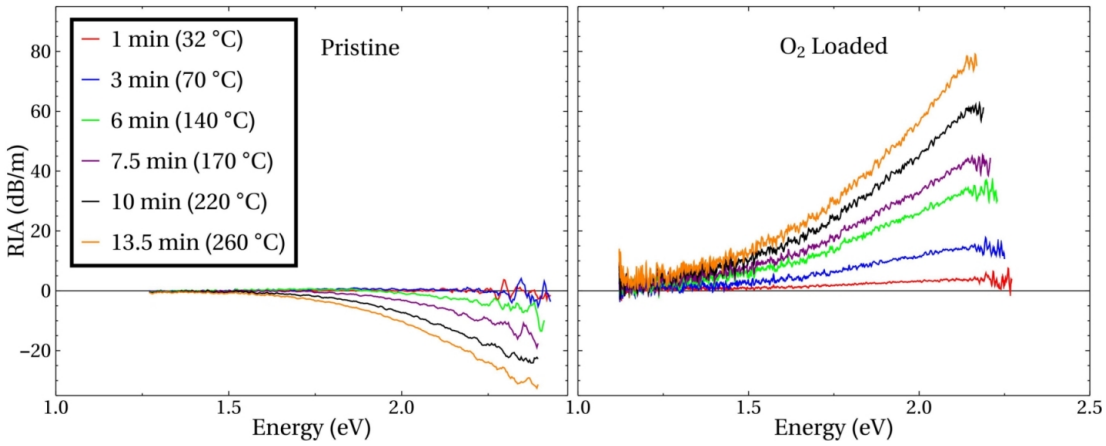

FIGURE 4.45 – Change of transmittance in PCe optical fiber during heating from room temperature (∼23 °C) to 300 °C.

very unusual behavior which could have already been observed during the heating to 300 °C. Figure 4.45 shows how transmissivity changed at different temperatures. Most surprising observation is that pristine and oxygen loaded fiber behave completely differently. Pristine fiber is characterized by increased attenuation while transmissivity of oxygen loaded fiber is actually increased. In both cases change of attenuation has been calculated using formula 3.85, which is normally applied to RIA measurements.

Variation of temperature is expected to induce small changes of transmissivity in most optical fibers via various contributions like changes of refractive index, defect conversion and others [1]. Increase of attenuation is most likely linked to oxygen loading however exact mechanism remains unknown as there is currently no literature describing such phenomena.

Radiation response is presented in figure 4.46. Results for non-loaded fiber show that RIA linearly increases up to absorbed dose of 20 kGy, after which growth speed reduces. Comparison with the results of irradiation at room temperature [113], where growth appears linear even at much greater doses, shows that at 300 °C growth again appears to become saturated at lower doses.

Contrary to previously described fibers it appears that oxygen loading has positive effects on radiation resistance of PCe fiber with lower growth speed of defects and characteristic red shift caused by oxygen loading. This can be seen in the upper part of the figure showing the kinetics of 2.0 eV band. Initially RIA at this energy is stronger in loaded fiber however at the doses above ∼10 kGy RIA starts to saturate, while the growth in pristine fiber remains constant.

Effects of recovery during the cooling of fibers are presented in figure 4.47. Recovery in pristine fiber can be barely observed while relatively strong relaxation is present in oxygen loaded fiber. This trend is very similar to the increase of

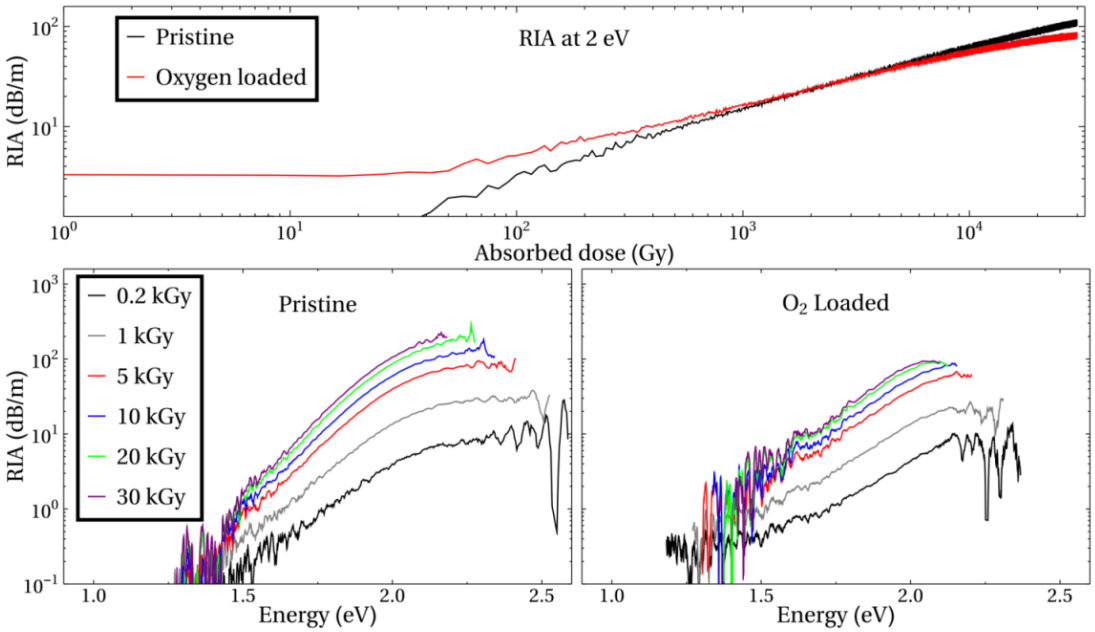

FIGURE 4.46 – RIA of PCe doped optical fiber under X-ray irradiation at several doses at ∼300 °C). Dose rate is 4.15 Gy/s.

attenuation during the heating so it is probable that the relaxation consists of two mechanisms, change of transmissivity as a function of temperature and actual recovery of created defects. On similar notice pristine fiber exhibited increase of transmissivity while heating, hence during cooling these phenomena might be reversed meaning the recovery now appears weaker. Further work would be required for accurate description of observed mechanisms. Overall behavior of PCe fiber irradiated at high temperature is fairly consistent with irradiation at room temperature.

CML studies of PCe fiber were performed using two excitation wavelengths, 1.9 eV aimed at detection of silica network related NBOHC defect shown in figure 4.48 and 3.4 eV which allowed observation of Ce^{3+} emission centers.

Results show that the overall concentration of NBOHC in fiber's core is very low regardless of treatments, similarly to PD1 fiber (concentration of P is 5 wt% higher in PCe fiber). Dynamics are more interesting in cladding, where various treatments appear to induce different quantities of defects. Again the strongest emission can be observed towards the outer edges of oxygen loaded fiber irradiated at room temperature like in P doped fiber (PD1, figure 4.41). Sharp peak can be also observed near core-cladding interface for oxygen loaded fiber irradiated at high temperature, but this feature loses intensity outwards indicating is most likely related to interface effects. Core cladding interface appears to be particularly interesting in this fiber as similar, although weaker, phenomenon can be also observed for non loaded fibers (pristine, heated and irradiated at high

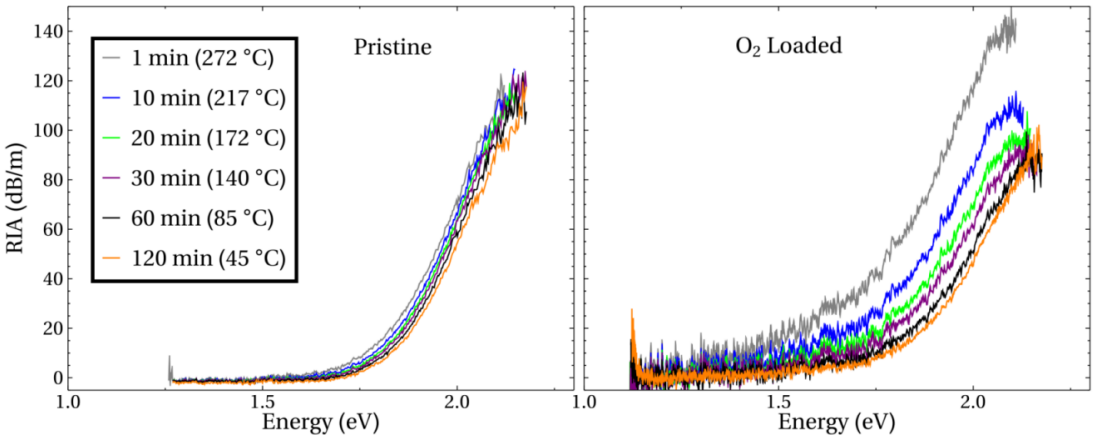

FIGURE 4.47 – Recovery from radiation induced damage in PCe fiber during cooling from 300 °C to room temperature (∼23 °C) after being irradiated with dose of 30 kGy.

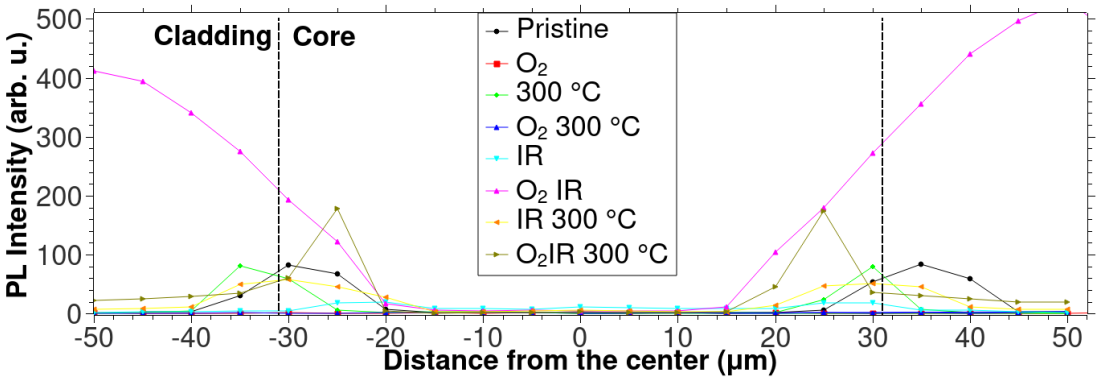

FIGURE 4.48 – CML cartographies of NBOHC emission at 649 nm in PCe OF after various treatments.

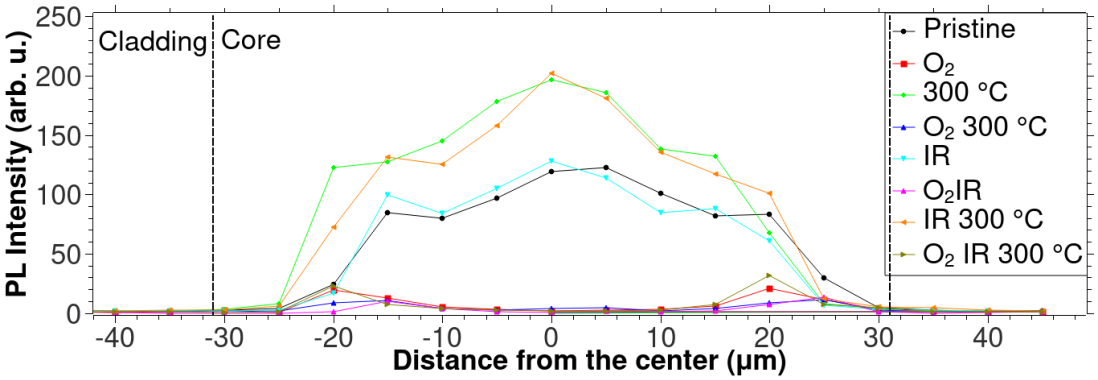

FIGURE 4.49 – CML cartographies of Ce^{3+} emission at 3.4 eV in PCe OF after various treatments.

temperature). It should be noted that there is preexisting NBOHC present in this fiber which remains preserved after high temperature treatment. Surprisingly the concentration of NBOHC does not seem to increase after irradiation at high temperature while concentration after irradiation appears to be significantly lower.

Results for CML study of Ce^{3+} concentrations in PCe fibers are fairly consistent with results of GeCeD1 fiber. Oxygen loading again almost completely saturates presence of Ce ions with the exception of area near core/cladding interface. Comparison of intensities from non-treated fibers yields interesting results. Compared to pristine fiber, intensity of Ce PL from fiber irradiated at room temperature appears to be unaffected by irradiation. Heating PCe fibers to high temperature seems to have positive effect on concentration of Ce^{3+} centers as the intensity is almost doubled. Again the center appears to be radiation resistant as there is virtually no difference with fiber that has not been irradiated.

4.3.5 Fujikura RRMMA fiber

This is the only commercially available optical fiber studied in this work. It has pure silica core ($d = 50$ µm) and F-doped cladding ($d = 125$ µm). This fiber has only been studied at the room temperature.

Radiation response of pristine and oxygen loaded fibers is presented in figure 4.50. Unloaded fiber exhibits really good radiation resistance across IR, visible and near UV domain. At smaller doses the growth in UV region around 6.2 eV, which is likely to origin from E', appears linear, however above 10 kGy a distinct shoulder becomes visible just below the 300 nm. This peak is most likely related to the formation of NBOHC and ODC(II) centers which are known to exist in irradiated pure silica [2, 24, 113]. Signatures of very weak absorption around 1.9 eV associated with NBOHC can be observed as well (not to be mistaken by sharp peak just below, which originates from instrumental setup).

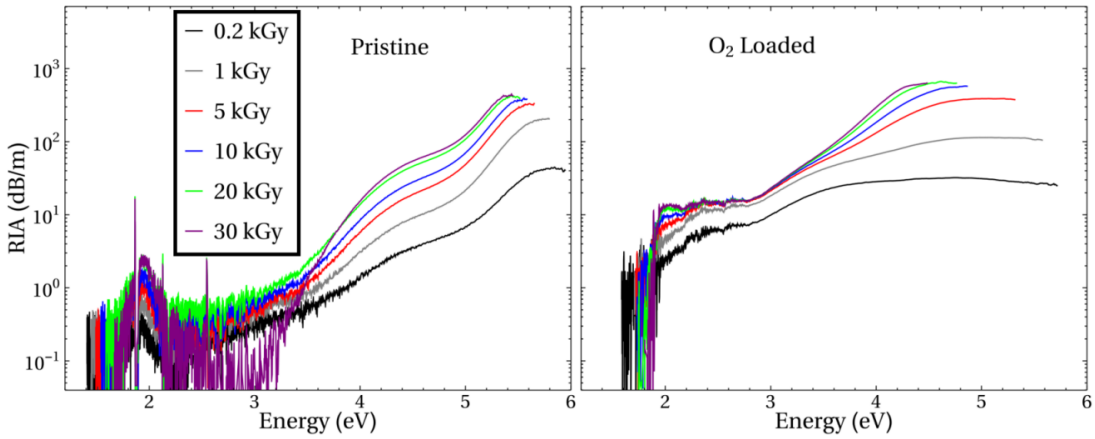

FIGURE 4.50 – Radiation induced attenuation of Fujikura RRMMA OF under X-ray irradiation at several doses at room temperature. Dose rate is 4.15 Gy/s.

Radiation response of oxygen loaded fiber appears to be more intense. Radiation resistance in the IR/Visible domain is preserved, however much stronger response to radiation induced attenuation can be seen in UV domain. According to similar study on different types of pure silica fiber [113] this increase can be mainly attributed to formation of ozone and much faster generation of NBOHC defect. Kinetics of 4.8 eV (NBOHC) and 5.6 eV (to probe the E' centers and their associated OA band at 5.8 eV) bands are shown in figure 4.51. NBOHC concentration in loaded fiber is higher by approximately an order of magnitude, however growth rates are similar in both pristine and loaded fibers. Similarly to pure silica core SiD1 fiber a change in growth rate can be observed after absorbed dose of $\sim$ 10 kGy, however in this fiber the change is less obvious. Initial concentration of E' is almost identical in both fibers. Initially this band appears to grow faster in pristine fiber, maybe due to oxygen passivation, but after $\sim$ 5 kGy the RIA in loaded fiber becomes stronger.

Figure 4.52 shows the post-mortem analysis of NBOHC concentration after different treatments using PL spectroscopy. Results show that very small quantities of NBOHC are present in non-irradiated fibers. As already evident from the RIA experiment, this fiber exhibits very good radiation resistance as demonstrated by the small increase of NBOHC signal. Oxygen loaded fiber irradiated at the room temperature on the other hand shows greatest intensity of NBOHC signal. Concentration of NBOHC appears to be the lowest at the core/cladding interface after which it increases drastically again as in most previously analyzed fibers.

While this fiber has not been studied using RIA technique at high temperature, post-mortem analysis of NBOHC concentration can yield some information regarding its temperature resistance. Surprisingly, high temperature appears to reduce overall concentration of NBOHC in loaded and non-loaded fibers. In pris-

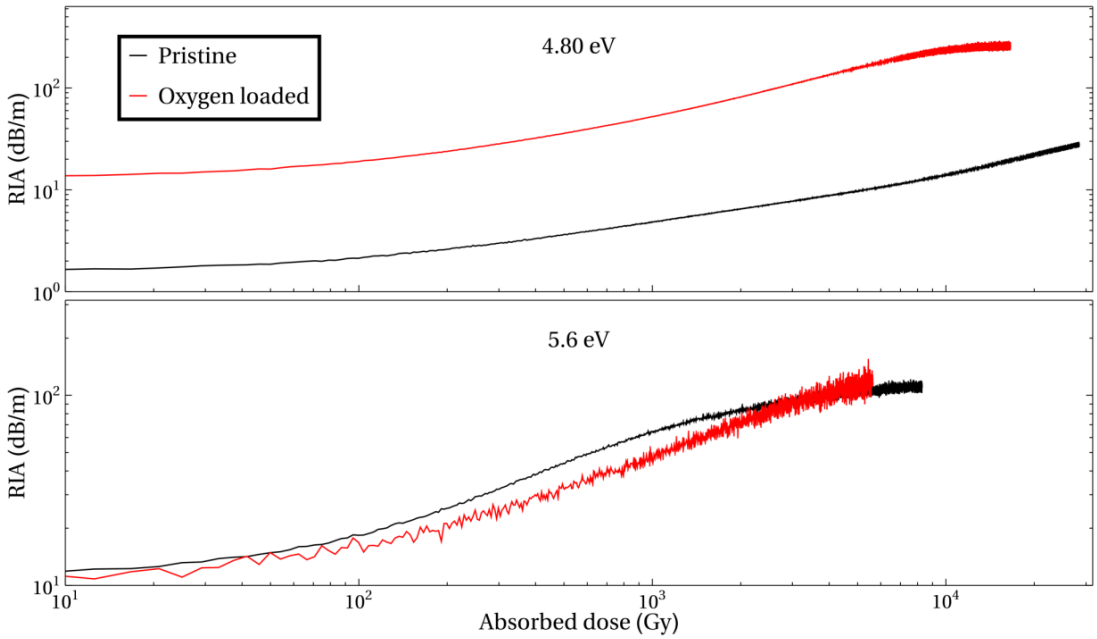

FIGURE 4.51 – Radiation induced attenuation growth at 4.8 eV and 5.6 eV of pristine/O_2 loaded Fujikura RRMMA OF as a function of absorbed dose at ∼300 °C. Dose rate is 4.15 Gy/s.

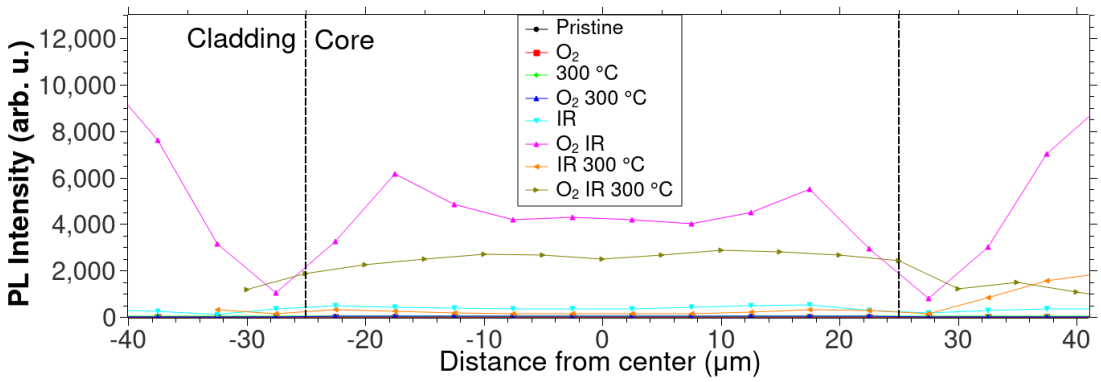

FIGURE 4.52 – CML cartographies of NBOHC emission at 1.9 eV in Fujkura RRMMA OF after various treatments.

tine fiber increased concentration of NBOHC is evident in the cladding, while in the core PL emission of NBOHC appears approximately 4× smaller compared to fibers irradiated at room temperature. Fiber irradiated with 30 kGy at high temperature exhibits on average ∼30-40% smaller emission in the core compared to fiber irradiated at room temperature. Kinetics of defects under irradiation are controlled by two competing mechanisms, formation generation and bleaching. High temperature is more likely to affect the bleaching mechanisms which result in speeding up the recovery. It has been already shown that in high grade fibers with pure silica cores radiation attenuation has been reduced when irradiated at high temperatures [160, 165, 166].

Conclusions

This research combined first principle theoretical approaches with experimental techniques in order to improve our knowledge regarding oxygen excess-related defects in amorphous silica.

In the first part of theoretical work, combination of DFT and many body perturbation theory approaches has been used in order to characterize structural, electronic and optical properties of various diamagnetic oxygen excess defects.

The first, and probably the most important, part deals with the optical signature of peroxy bridge defect. It has been widely considered as the main neutral oxygen excess defect in silica, however, its existence has never been directly confirmed. One of the most important questions concerns its optical signature. Results show that POL is characterized by a series of weak absorption peaks spanning between 3 and 6 eV. Combination of results from simplified hydrogen peroxide molecule representing POL defect and a wide selection of configurations, needed for statistical approach, has shown that structural disorder is directly responsible for the dispersion of POL's optical absorption. Combination of dispersion and overall low oscillator strength have been considered as the main reasons why this defect is optically invisible. Finally multiple peroxides have been considered, separated by small distances. Such configurations might be important following irradiation treatments where oxygen molecule becomes dissociated and its atoms incorporate into neighboring matrix. Surprisingly, no correlations have been found between formation energy and distance separating two interstitials.

Historically, ozonyl defect has been only marginally investigated, most noticeably in references [54, 99], which proposed that ozonyl could act as an intermediate stage in oxygen diffusion in quartz. According to the more extended investigation performed in the present work, the calculated mean formation energy of ozonyl is slightly higher ($\sim$0.3 eV) than the mean formation energy of POL. The overlap between two formation energy distributions confirms that both defects could co-exist in oxygen rich conditions. Electronic structure and optical bands of ozonyl are very similar to POL, with the main difference that in the case of ozonyl HOMO-1 is found to be always below the Top of the Valence Band. Therefore, the energy range of the optical transitions will not be affected by the dihedral angle (as in the case of POL). As such, the absorption bands will be poorly affected by site-to-site disorder. It induces weak absorption bands in the lower UV domain ($\sim$4 eV) but it should be clearly visible with strong absorption around 7 eV.

Investigating passivation mechanism between ODCs with oxygen molecule it

has been found that in some cases the network losses the memory of the pre-existing defect (ODC(I) and for some ODC(II) - ones which are able to reconstruct) sites while in other cases the reaction leads to the reversible formation of dioxasilirane-like groups. In particular, the stability (lower formation energy) of dioxasilirane-like groups is higher than GLPC/ODC(II) defects. On average the formation energy of dioxasilirane/dioxagermirane is lower by 3.5 eV than Si-ODC(II), and lower by 0.8 eV than its respective GLPC.

Regarding oxygen exchange mechanisms, past studies have already proposed different reactions with O_2 molecule, for which the need for explicit treatment of spin state of oxygen molecule has been completely overseen. In this PhD work it has been shown that oxygen singlet to triplet transition of O_2 molecule (radiative or not) is most probable to occur after the release of molecule from the network, when the electronic configuration reaches ground state characterized by two π orbitals being degenerate. This configuration does not necessarily occur at the saddle point as assumed in references [98, 99]. As a prospect it would be very interesting to investigate such process by optimizing existing approaches or developing new ones able to tackle radiative and non-radiative spin flipping in such a complex system from first-principles. Several reactions have been considered in this work. The first studied reaction was the release of oxygen molecule from ozonyl defect, as it has been predicted that it might be a favorable configuration in network oxygen migration [54]. Results show that the activation energy for this reaction ranges from 0.44 eV to 1.35 eV, while the energy barrier for reverse reaction has an average value of around 1.9 eV excluding the excitation of the oxygen molecule to the first excited singlet state. It is worth to note that, because of spin conservation, an oxygen molecule in its ground state (triplet) does not oxidize reactants in singlet state [156]. Indeed a large amount of chemical research is devoted to find conversion routes (chemically, enzymatically, or photochemically) [157]. Comparison with the activation energies derived from experimental data [44] shows that this reaction might occur at temperatures as low as 180 K. At room temperature, however, it is expected that all ozonyl groups have released the corresponding O_2 molecules, i.e. the defect is not stable.

The study of ozonyl groups as intermediate step [54] has further confirmed its major role in oxygen exchange. Indeed the release of O_2 by two POLs requires the intermediate formation of an ozonyl group, and vice-versa for the formation of two POLs from an oxygen molecule, contrary to the commonly assumed direct formation of POL.

In agreement with previous work [107] the migration energies of POLs have been found to be higher compared to oxygen molecule, with values spanning between 1.46 and 1.93 eV while the last step, in which the ozonyl is formed has

lower barrier (1.0-1.5 eV).

Oxygen molecule has also been shown to readily passivate vacancy sites in agreement with literature [113, 117, 120]. Barrier for this reaction has values between 0.2 and 0.4 eV excluding the triplet to singlet excitation of oxygen molecule. The creation of vacancy site following the release of molecule from peroxy defect however has very high activation energy ($\sim$ 4 - 6.3 eV) which should, according to experimental data, correspond to temperatures above 1000 °C.

When oxygen interacts with GLPC, it can readily form dioxagermirane with small barrier (0.01-0.6 eV) excluding the excitation of oxygen into singlet state while the energy required for the release of oxygen from dioxasilirane ranges between 1.0 and 1.60 eV. This energy agrees well with the known oxygen migration barrier in silica meaning this release reaction could be also happening alongside already described release of interstitials oxygens via ozonyl. Finally studies of dioxasilirane dynamics lead to the discovery of a new mechanism describing the interaction of GLPC and oxygen molecule, where dioxasilirane acts as intermediate step. This mechanism is conceptually similar to the rotation of ODC(I) responsible for the creation of ODC(II) [30], as the dioxasilirane transforms into perfectly coordinated network.

Experimental characterization of temperature and irradiation effects of oxygen loaded optical fibers have been studied using on-line RIA and post-mortem PL techniques. In agreement with previous similar study [113] radiation response has been found to depend strongly on the dopants. Effects of the oxygen loading are not uniform, i.e. in some fibers it has been shown to increase the radiation resistance while in some others it leads to its decrease. Results of PL studies have revealed that oxygen loading completely quenches radiative centers in rare earth doped fibers.

Overall the theoretical work might provide some new insights into atomic scale phenomena in oxygen rich silica materials. In order to properly understand oxygen related reactions further improvements of theoretical methods are needed to address spin flipping mechanisms, as stated before. Another important issue that remains in the field of theoretical predictions is the efficient (computationally affordable) mapping of the energy surface, i.e. the search for all possible local/global minimum and their corresponding saddle points in complex materials such as SiO_2. In this context, maybe machine learning based approaches would provide with some additional insights.

On the experimental side, oxygen loading has been shown to improve radiation resistance in combination with some dopants [113, 120], however the exact mechanisms of interaction remain relatively poorly understood. One of the main perspectives in this field might be a further coupling of specifically designed

experiments with theoretical studies.

Scientific contributions

Original research papers

Blaž Winkler, Layla Martin-Samos, Nicolas Richard, Luigi Giacomazzi, Antonino Alessi, Sylvain Girard, Aziz Boukenter, Youcef Ouerdane, and Matjaz Valant. Correlations between Structural and Optical Properties of Peroxy Bridges from First Principles, *Journal of Physical Chemistry C*, 121 : 4002-4010, 2017.

Sylvain Girard, Adriana Morana, Antonino Alessi, Aziz Boukenter, Blaž Winkler, Diego Di Francesca, Iméne Reghioua, Layla Martin-Samos, Luigi Giacomazzi, Marco Cannas, Nicolas Richard, Philippe Paillet, Simonpietro Agnello, Thierry Robin, Vincenzo De Michele, Youcef Ouerdane. Overview of radiation induced point defects in silica-based optical fibers, submitted to *Reviews in physics*.

Imene Reghioua, Antonino Alessi, Diego Di Francesca, Sylvain Girard, Layla Martin-Samos, Blaž Winkler, Luigi Giacomazzi, Mattia Fanetti, Nicola Richard, Philippe Paillet , Mélani Raine, Simonpietro Agnello, Aziz Boukenter, Youcef Ouerdane. O_2 loading of germanosilicate optical fibers : *Ab initio* simulation study and experimental in-situ investigation of GLPC evolution under irradiation, in preparation.

Conference presentations

Blaž Winkler, Layla Martin-Samos, Nicolas Richard, Sylvain Girard. *Ab-initio* modeling of peroxy bridge defect in amorphous silica. 17th International Workshop on Computational Physics and Materials Science : Total Energy and Force Methods. 15-17 January 2015, Trieste, Italy.

Blaž Winkler, Layla Martin-Samos, Nicolas Richard, Luigi Giacomazzi, Antonino Alessi, Sylvain Girard, Aziz Boukenter, Youcef Ouerdane, and Matjaz Valant. Optical properties of peroxy link defects from first principles. 11th International Symposium on SiO_2, Advanced Dielectrics and Related Devices, 13-15 June 2016, Nice, France.

Blaž Winkler, Layla Martin-Samos, Nicolas Richard, Luigi Giacomazzi, Antonino

Alessi, Sylvain Girard, Aziz Boukenter, Youcef Ouerdane, and Matjaz Valant. Correlations between structural and optical properties of peroxy bridges from first principles. 4th conference on Physical and theoretical chemistry, 18-19 September 2017, Dublin, Ireland.

Blaž Winkler, Layla Martin-Samos, Nicolas Richard, Luigi Giacomazzi, Antonino Alessi, Sylvain Girard, Aziz Boukenter, Youcef Ouerdane, and Matjaz Valant. Correlations between structural and optical properties of peroxy bridges from first principles. FisMat 2017, 1-5 October, 2017, Trieste, Italy.

Bibliographie

[1] G. P. Agrawal. *Fiber-Optic Communications Systems.* John Wiley and Sons, New York, 2002.

[2] G. Pacchioni, D. L. Griscom, and L. Skuja, editors. *Defects in SiO_2 and Related Dielectrics : Science and Technology.* NATO Science Ser. II, Vol. 2 (Kluwer Academic Publishers), Dordrecht-Boston-London, 2000.

[3] CRC Handbook. *CRC Handbook of Chemistry and Physics, 88th Edition.* CRC Press, 2007.

[4] Julius Scherzer. Dealuminated faujasite-type structures with $SiO_2Al_2O_3$ ratios over 100. *Journal of Catalysis*, 54:285 – 288, 1978.

[5] Peter Atkins and Julio de Paula. *Atkins' Physical Chemistry.* Oxford University Press, Great Clarendon Street, Oxford, 2010.

[6] K.T.V. Grattan and T. Sun. Fiber optic sensor technology : an overview. *Sensors and Actuators A : Physical*, 82:40 – 61, 2000.

[7] J. Hansryd, P. A. Andrekson, M. Westlund, Jie Li, and P. Hedekvist. Fiber-based optical parametric amplifiers and their applications. *IEEE Journal of Selected Topics in Quantum Electronics*, 8:506–520, 2002.

[8] Sergei Popov. Fiber laser overview and medical applications. In *Tunable Laser Applications*, pages 197–226. 2008.

[9] Sylvain Girard, Adriana Morana, Ayoub Ladaci, Thierry Robin, Luciano Mescia, Jean-Jacques Bonnefois, Mathieu Boutillier, Julien Mekki, Armelle Paveau, Benoît Cadier, Emmanuel Marin, Youcef Ouerdane, and Aziz Boukenter. Recent advances in radiation-hardened fiber-based technologies for space applications. *Journal of Optics*, 20:093001, 2018.

[10] John W. Berthold. Overview of prototype fiber optic sensors for future application in nuclear environments, 1994.

[11] W. D. Callister and D. G. Rethwisch. *Fundamentals of materials science and engineering, 3rd edition.* John Wiley and sons inc., Hoboken, 2008.

[12] J.A. Erwin Desa, Adrian C. Wright, Joe Wong, and Roger N. Sinclair. A neutron diffraction investigation of the structure of vitreous zinc chloride. *Journal of Non-Crystalline Solids*, 51:57 – 86, 1982.

[13] Xavier Gonze, Douglas C. Allan, and Michael P. Teter. Dielectric tensor, effective charges, and phonons in α-quartz by variational density-functional perturbation theory. *Physical Review Letters*, 68:3603–3606, 1992.

[14] W. H. Zachariasen. The atomic arrangement in glass. *Journal of the American Chemical Society*, 54:3841–3851, 1932.

[15] Jörg Neuefeind and K.-D. Liss. Bond angle distribution in amorphous germania and silica. *Berichte der Bunsengesellschaft für physikalische Chemie*, 100:1341–1349, 1996.

[16] Kurt Binder and Walter Kob. *Glassy Materials and Disordered Solids*. World Scientific, Singapore, 2011.

[17] Alfredo Pasquarello and Roberto Car. Identification of raman defect lines as signatures of ring structures in vitreous silica. *Physical Review Letters*, 80:5145–5147, 1998.

[18] P. Umari, Xavier Gonze, and Alfredo Pasquarello. Concentration of small ring structures in vitreous silica from a first-principles analysis of the Raman spectrum. *Physical Review Letters*, 90.

[19] Abdelali Rahmani, Magali Benoit, and Claude Benoit. Signature of small rings in the Raman spectra of normal and compressed amorphous silica : A combined classical and ab initio study. *Physical Review B*, 68:184202, 2003.

[20] Panayiotis A. Varotsos and Kessar D. Alexopoulos, editors. *Thermodynamics of Point Defects and Their Relation with Bulk Properties*. Elsevier, New York, 1986.

[21] L. Skuja, M. Hirano, H. Hosono, and K. Kajihara. Defects in oxide glasses. *Physica Status Solidi*, 2:15–24, 2005.

[22] B.J. Isherwood and C.A. Wallace. X-ray diffraction studies of defects in crystals. *Physics in Technology*, 5:244, 1974.

[23] P. H. Gaskell and Society of Glass Technology. *The Structure of non-crystalline materials : proceedings of the symposium held in Cambridge, England on 20-23 September 1976 / edited by P. H. Gaskell*. Taylor and Francis [for] the Society of Glass Technology, 1977.

[24] Linards Skuja. Optically active oxygen-deficiency-related centers in amorphous silicon dioxide. *Journal of Non-Crystalline Solids*, 239(1-3):16–48, 1998.

[25] Gianpiero Buscarino. *Experimental investigation on the microscopic structure of intrinsic paramagnetic point defects in amorphous silicon dioxide*. PhD thesis, Universitá degli Studi di Palermo, 2006.

[26] David L. Griscom. Nature of defects and defect generation in optical glasses. *Proceedings of the Society of Photo-Optical Instrumentation Engineers*, 0541:0541 – 0541 – 22, 1985.

[27] G. Pacchioni and G. Ierano. Ab initio theory of optical transitions of point defects in SiO_2. *Physical Review B*, 57:818–831, 1998.

[28] N. Richard, L. Martin-Samos, S. Girard, A. Ruini, A. Boukenter, Y. Ouerdane, and J-P. Meunier. Oxygen deficient centers in silica : optical properties within many-body perturbation theory. *Journal of Physics : Condensed Matter*, 25:1–8, 2013.

[29] S. Girard, N. Richard, Y. Ouerdane, G. Origlio, A. Boukenter, L. Martin-Samos, P. Paillet, J. . Meunier, J. Baggio, M. Cannas, and R. Boscaino. Radiation effects on silica-based preforms and optical fibers-ii : Coupling ab initio simulations and experiments. *IEEE Transactions on Nuclear Science*, 55:3508–3514, 2008.

[30] Luigi Giacomazzi, L. Martin-Samos, A. Boukenter, Y. Ouerdane, S. Girard, A. Alessi, S. de Gironcoli, and N. Richard. Photoactivated processes in optical fibers : generation and conversion mechanisms of twofold coordinated Si and Ge atoms. *Nanotechnology*, 28:195202, 2017.

[31] L.N. Skuja, A.N. Streletsky, and A.B. Pakovich. A new intrinsic defect in amorphous SiO_2 : Twofold coordinated silicon. *Solid State Communications*, 50(12):1069 – 1072, 1984.

[32] Marion A. Stevens-Kalceff. Cathodoluminescence microanalysis of silica and amorphized quartz. *Mineralogy and Petrology*, 107:455–469, 2013.

[33] Linards Skuja. Isoelectronic series of twofold coordinated Si, Ge, and Sn atoms in glassy SiO_2 : a luminescence study. *Journal of Non-Crystalline Solids*, 149:77 – 95, 1992.

[34] L. Skuja, K. Kajihara, M. Hirano, and H. Hosono. Oxygen-excess-related point defects in glassy/amorphous SiO_2 and related materials. *Nuclear Instruments and Methods in Physics Research Section B : Beam Interactions with Materials and Atoms*, 286:159 – 168, 2012.

[35] E. J. Friebele, D. L. Griscom, M. Stapelbroek, and R. A. Weeks. Fundamental defect centers is glass : the peroxy radical in irradiated, high-purity, fused silica. *Physical Review Letters*, 42:1346–1349, 1979.

[36] D.L. Griscom. Electron spin resonance in glasses. *Journal of Non-Crystalline Solids*, 40:211 – 272, 1980.

[37] H. Nishikawa, R. Tahmon, Y. Ohki, K. Nagasawa, and Q. Hama. Defects and optical absorption bands induced by surplus oxygen in high purity synthetic silica. *Journal of Applied Physics*, 65:4672–4678, 1989.

[38] K. Awazu, H. Kawazoe, K. Muta, T. Ibuki, K. Tabayashi, and K. Shobatake. Characterization of silica glasses sintered under Cl_2 ambients. *Journal of Applied Physics*, 69:1849–1853, 1991.

[39] K. Awazu, K. Harada, H. Kawazoe, and K. Muta. Structural imperfections in silica glasses with an optical absorption peak at 3.8 ev. *Journal of Applied Physics*, 72:4696–4699, 1992.

[40] H. Imai, K. Arai, H. Hosono, Y. Abe, T. Arai, and H. Imagawa. Dependence of defects induced by excimer laser on intrinsic structural defects in synthetic silica glasses. *Physical Review B*, 44:1812–1818, 1991.

[41] H. Imai, K. Arai, T. Saito, S. Ichimura, H. Nonaka, J. P. Vigouroux, H. Hosono, Y. Abe, and H. Imagawa. *The Physics and Technology of Amorphous SiO_2*, page 153. New York, 1988.

[42] E. Vella, R. Boscaino, and G. Navarra. Vacuum-ultraviolet absorption of amorphous SiO_2 : Intrinsic contribution and role of silanol groups. *Physical Review B*, 77:165203, 2008.

[43] Y. Sakurai. Correlation between the 1.5 eV photoluminescence band and peroxy linkage in silica glass. *Journal of Non-Crystalline Solids*, 276:159–162, 2000.

[44] L. Skuja, K. Kajihara, T. Kinoshita, M. Hirano, and H. Hosono. The behavior of interstitial oxygen atoms induced by F_2 laser irradiation of oxygen-rich glassy SiO_2. *Nuclear Instruments and Methods in Physics Research B*, 191:127–130, 2002.

[45] K. Kajihara, L. Skuja, and H. Hosono. Diffusion and reactions of photoinduced interstitial oxygen atoms in amorphous SiO_2 impregnated with ^{18}O-labeled interstitial oxygen molecules. *Journal of Physical Chemistry C*, 118:4282–4286, 2014.

[46] A. Mehonic, M. Buckwell, L. Montesi, L. Garnett, S. Hudziak, S. Fearn, R. Chater, D. McPhail, and A. J. Kenyon. Structural changes and conductance thresholds in metal-free intrinsic SiO_x resistive random access memory. *Journal of Applied Physics*, 117:124505, 2015.

[47] E. O'Reilly and J. Robertson. Theory of defects in vitreous silicon dioxide. *Physical Review B*, 27:3780–3795, 1983.

[48] B. B. Stefanov and K. Raghavachari. Photoabsorption of the peroxide linkage defect in silicate glasses. *Journal of Chemical Physics*, 111:8039–8042, 1999.

[49] M. A. Szymanski, A. L. Shluger, and A. M. Stoneham. Role of disorder in incorporation energies of oxygen atoms in amorphous silica. *Physical Review B*, 63:224207, 2001.

[50] D. Ricci, G. Pacchioni, M. A. Szymanski, A. L. Shluger, and A. M. Stoneham. Modeling disorder in amorphous silica with embedded clusters : The peroxy bridge defect center. *Physical Review B*, 64:224104, 2001.

[51] L. Martin-Samos, Y. Limoge, J.-P. Crocombette, and G. Roma. Neutral self-defects in a silica model : A first-principles study. *Physical Review B*, 71:014166, 2005.

[52] Y. Cheng, D. Ren, H. Zhang, and X. Cheng. First-principle study of the structural, electronic and optical properties of defected amorphous silica. *Journal of Non-Crystalline Solids*, 416:36–43, 2015.

[53] W. Wang, P. Lu, L. Han, C. Zhang, L. Wu, P. Guan, R. Su, and J. Chen. Structural and electronic properties of peroxy linkage defect and its interconversion in fused silica. *Journal of Non-Crystalline Solids*, 434:96–101, 2016.

[54] J. R. Chelikowsky, D. J. Chadi, and N. Binggeli. Oxygen configurations in silica. *Physical Review B*, 62:2251–2254, 2000.

[55] Angelo Bongiorno and Alfredo Pasquarello. Oxygen diffusion through the disordered oxide network during silicon oxidation. *Physical Review Letters*, 88:125901, 2002.

[56] D. R. Hamann. Diffusion of atomic oxygen in SiO_2. *Physical Review Letters*, 81:3447, 1998.

[57] G. Roma, Y. Limoge, and S. Baroni. Oxygen self-diffusion in alpha-quartz. *Physical Review Letters*, 86:4564–4567, 2001.

[58] L. Skuja, B. Güttler, D. Schiel, and A. R. Silin. Infrared photoluminescence of preexisting or irradiation-induced interstitial oxygen molecules in glassy SiO_2 and α-quartz. *Physical Review B*, 84:14296, 1998.

[59] L. Skuja, M. Hirano, and H. Hosono. Oxygen-related intrinsic defects in glassy SiO_2 : Interstitial ozone molecules. *Physical Review Letters*, 84:302–5, 2000.

[60] L. Skuja and B. Güttler. Detection of interstitial oxygen molecules in SiO_2 glass by a direct photoexcitation of the infrared luminescence of singlet O_2. *Physical Review Letters*, 77:2094, 1996.

[61] S. Agnello, M. Cannas, L. Vaccaro, G. Vaccaro, F. M. Gelardi, M. Leone, V. Militello, and R. Boscaino. Near-infrared emission of O_2 embedded in amorphous SiO_2 nanoparticles. *The Journal of Physical Chemistry C*, 115:12831–12835, 2011.

[62] D. L. Baulch, R. A. Cox, R. F. Hampson, J. A. Kerr, J. Troe, and R. T. Watson. Evaluated kinetic and photochemical data for atmospheric chemistry : Supplement II. CODATA task group on gas phase chemical kinetics. *Journal of Physical and Chemical Reference Data*, 13:1259–1380, 1984.

[63] Koichi Awazu and Hiroshi Kawazoe. O_2 molecules dissolved in synthetic silica glasses and their photochemical reactions induced by ArF excimer laser radiation. *Journal of Applied Physics*, 68:3584–3591, 1990.

[64] David L. Griscom. Optical properties and structure of defects in silica glass. *Journal of the Ceramic Society of Japan*, 99:923–942, 1991.

[65] Linards Skuja, Toshio Suzuki, and Katsumi Tanimura. Site-selective laser-spectroscopy studies of the intrinsic 1.9-eV luminescence center in glassy sio_2. *Physical Review B*, 52:15208–15216, 1995.

[66] Koichi Kajihara, Linards Skuja, Masahiro Hirano, and Hideo Hosono. Formation and decay of nonbridging oxygen hole centers in SiO_2 glasses induced by F_2 laser irradiation : In situ observation using a pump and probe technique. *Applied Physics Letters*, 79:1757–1759, 2001.

[67] M. Cannas and F. M. Gelardi. Vacuum ultraviolet excitation of the 1.9-ev emission band related to nonbridging oxygen hole centers in silica. *Physical Review B*, 69:153201, 2004.

[68] V.A. Radzig. Chapter 7 point defects on the silica surface : Structure and reactivity. In Leonid I. Trakhtenberg, Sheng H. Lin, and Olusegun J. Ilegbusi, editors, *Physico-Chemical Phenomena in Thin Films and at Solid Surfaces*, volume 34, pages 231 – 345. 2007.

[69] Lavinia Vaccaro, Adriana Morana, Viktor Radzig, and Marco Cannas. Bright visible luminescence in silica nanoparticles. *The Journal of Physical Chemistry C*, 115(40):19476–19481, 2011.

[70] Takashi Uchino, Naoko Kurumoto, and Natsuko Sagawa. Structure and formation mechanism of blue-light-emitting centers in silicon and silica-based nanostructured materials. *Physical Review B*, 73:233203, 2006.

[71] R. A. Weeks. Paramagnetic resonance of lattice defects in irradiated quartz. *Journal of Applied Physics*, 27:1376–1381, 1956.

[72] David L. Griscom. Characterization of three E'-center variants in X- and γ-irradiated high purity a-SiO_2. *Nuclear Instruments and Methods in Physics Research Section B : Beam Interactions with Materials and Atoms*, 1:481 – 488, 1984.

[73] S. Agnello, G. Buscarino, F. M. Gelardi, and R. Boscaino. Optical absorption band at 5.8 eV associated with the E'_γ centers in amorphous silicon dioxide : Optical absorption and EPR measurements. *Physical Review B*, 77:195206, 2008.

[74] S. Agnello, R. Boscaino, G. Buscarino, M. Cannas, and F. M. Gelardi. Structural relaxation of E'_γ centers in amorphous silica. *Physical Review B*, 66:113201, 2002.

[75] G. Buscarino, S. Agnello, and F. M. Gelardi. Delocalized nature of the E'_δ center in amorphous silicon dioxide. *Physical Review Letters*, 94:125501, 2005.

[76] G. Buscarino, S. Agnello, and F. M. Gelardi. Hyperfine structure of the E' γ centre in amorphous silicon dioxide. *Journal of Physics : Condensed Matter*, 18:5213, 2006.

[77] L. Skuja and A. Naber. Site-selective luminescence study of defects in gamma-irradiated glassy germanium dioxide. *Nuclear Instruments and Methods in Physics Research Section B : Beam Interactions with Materials and Atoms*, 116:549 – 553, 1996.

[78] Linards Skuja, Hideo Hosono, and Masahiro Hirano. Laser-induced color centers in silica. *Proceedings of the Society of Photo-Optical Instrumentation Engineers*, 4347:4347 – 4347 – 14, 2001.

[79] Hideo Hosono, Koichi Kajihara, Takenobu Suzuki, Yoshiaki Ikuta, Linards Skuja, and Masahiro Hirano. Vacuum ultraviolet optical absorption band of non-bridging oxygen hole centers in SiO_2 glass. *Solid State Communications*, 122:117 – 120, 2002.

[80] Linards Skuja, Koichi Kajihara, Masahiro Hirano, and Hideo Hosono. Visible to vacuum-uv range optical absorption of oxygen dangling bonds in amorphous SiO_2. *Physical Review B*, 84:205206, 2011.

[81] M. Cannas, L. Vaccaro, and B. Boizot. Spectroscopic parameters related to non-bridging oxygen hole centers in amorphous-SiO_2. *Journal of non-crystalline solids*, 352:203–208, 2006.

[82] L. Skuja, K. Tanimura, and N. Itoh. Correlation between the radiation induced intrinsic 4.8 eV optical absorption and 1.9 eV photoluminescence bands in glassy SiO_2. *Journal of Applied Physics*, 80:3518–3525, 1996.

[83] L. Vaccaro, M. Cannas, and R. Boscaino. Luminescence features of nonbridging oxygen hole centres in silica probed by site-selective excitation with tunable laser. *Solid State Communications*, 146:148 – 151, 2008.

[84] R. A. B. Devine and J. Arndt. Defect pair creation through ultraviolet radiation in dense, amorphous $\mathsf{sio_2}$. *Physical Review B*, 42:2617–2620, 1990.

[85] David L. Griscom. Thermal bleaching of X-ray-induced defect centers in high purity fused silica by diffusion of radiolytic molecular hydrogen. *Journal of Non-Crystalline Solids*, 68:301 – 325, 1984.

[86] Shuji Munekuni, Nobuyuki Dohguchi, Hiroyuki Nishikawa, Yoshimichi Ohki, Kaya Nagasawa, and Yoshimasa Hama. SiOSi strained bond and paramagnetic defect centers induced by mechanical fracturing in amorphous SiO_2. *Journal of Applied Physics*, 70:5054–5062, 1991.

[87] T. Bakos, S. N. Rashkeev, and S. T. Pantelides. Optically active defects in $\mathsf{Sio_2}$: The nonbridging oxygen center and the interstitial OH molecule. *Physical Review B*, 70:075203, 2004.

[88] Shuji Munekuni, Toshihisa Yamanaka, Yasushi Shimogaichi, Ryoichi Tohmon, Yoshimichi Ohki, Kaya Nagasawa, and Yoshimasa Hama. Various types of nonbridging oxygen hole center in high-purity silica glass. *Journal of Applied Physics*, 68:1212–1217, 1990.

[89] V. A. Radtsig. Reactive intermediates on the surface of solids ($si0_2$ and $ge0_2$) : A review of studies and prospects for their development. *Chemical Physics Reports*, 14:1206–1245, 1995.

[90] Hideo Hosono and Robert A. Weeks. Bleaching of peroxy radical in SiO_2 glass with 5 eV light. *Journal of Non-Crystalline Solids*, 116:289 – 292, 1990.

[91] Yuryo Sakurai and Kaya Nagasawa. Green photoluminescence band in γ-irradiated oxygen-surplus silica glass. *Journal of Applied Physics*, 86:1377–1381, 1999.

[92] Burkhard C. Schmidt, F.M. Holtz, and J.-M. Beny. Incorporation of H_2 in vitreous silica, qualitative and quantitative determination from Raman and infrared spectroscopy. *Journal of non-crystalline solids*, 240:91–103, 1998.

[93] James E. Shelby. Protonic species in vitreous silica. *Journal of Non-Crystalline Solids*, 179:138 – 147, 1994.

[94] Yukihiro Morimoto, Shigenori Nozawa, and Hideo Hosono. Effect of xe_2^* light (7.2 ev) on the infrared and vacuum ultraviolet absorption properties of hydroxyl groups in silica glass. *Physical Review B*, 59:4066–4073, 1999.

[95] Masafumi Mizuguchi, Linards Skuja, Hideo Hosono, and Tohru Ogawa. F-doped and H_2-impregnated synthetic SiO_2 glasses for 157 nm optics. *Journal of Vacuum Science & Technology B : Microelectronics and Nanometer Structures Processing, Measurement, and Phenomena*, 17:3280–3284, 1999.

[96] Yoshiaki Ikuta, Shinya Kikugawa, Masahiro Hirano, and Hideo Hosono. Defect formation and structural alternation in modified SiO_2 glasses by irradiation with F_2 laser or ArF excimer laser. *Journal of Vacuum Science and Technology B : Microelectronics and Nanometer Structures Processing, Measurement, and Phenomena*, 18:2891–2895, 2000.

[97] Zhixing Peng, Pengfei Lu, Baonan Jia, Jie Zhang, Binbin Yan, You Wang, Bin Yang, and Gang-Ding Peng. Conversion mechanisms of peroxy linkage defect in silica optical fiber. *Journal of Non-Crystalline Solids*, 498:103 – 108, 2018.

[98] T. Bakos, S. N. Rashkeev, and S. T. Pantelides. H_2O and O_2 molecules in amorphous SiO_2 : Defect formation and annihilation mechanisms. *Physical Review B*, 69:195206–1–9, 2004.

[99] Tamás Bakos. *Defects in amorphous SiO_2 : Reactions, dynamics and optical properties.* PhD thesis, Vanderbilt University, 2003.

[100] R.H. Doremus. *Diffusion of Reactive Molecules in Solids and Melts.* Wiley, New York, 2002.

[101] D. Di Francesca, S. Agnello, S. Girard, C. Marcandella, P. Paillet, A. Boukenter, Y. Ouerdane, and F. M. Gelardi. Influence of O_2-loading pretreatment on the radiation response of pure and fluorine-doped silica-based optical fibers. *IEEE Transactions on Nuclear Science*, 61:3302–3308, 2014.

[102] H. C. Lu, T. Gustafsson, E. P. Gusev, and E. Garfunkel. An isotopic labeling study of the growth of thin films on Si(100). *Applied Physics Letters*, 67:1742, 1995.

[103] S. Agnello, L. Vaccaro, M. Cannas, and K. Kajihara. Temperature dependance of O_2 singlet photoluminescence in silica nanoparticles. *Journal of Non-Crystaline Solids*, 379:220, 2013.

[104] D. Di Francesca, S. Girard, S. Agnello, C. Marcandella, P. Paillet, A. Boukenter, F. M. Gelardi, and Y. Ouerdane. Near infrared radio-luminescence of O_2 loaded radiation hardened silica optical fibers : A candidate dosimeter for harsh environments. *Applied Physics Letters*, 105:183508–1, 2014.

[105] K. Kajihara, T. Miura, Hayato Kamioka, M. Uramoto A. Aiba, Y. Morimoto, M. Hirano, L. Skuja, and H. Hosono. Diffusion and reactions of interstitial oxygen species in amorphous SiO_2 : A review. *Journal of Non-Crystalline Solids*, 354:224–232, 2008.

[106] Laura Nuccio. *Diffusion of small molecules in amorphous SiO_2 : effects on the properties of the material and on its point defects.* PhD thesis, Universitá degli Studi di Palermo, 2009.

[107] A. Bongiorno and A. Pasquarello. Multiscale modeling of oxygen diffusion through the oxide during silicon oxidation. *Physical Review B*, 70:195312, 2004.

[108] C.C. Tournour and James Shelby. Molecular oxygen diffusion in vitreous silica. *Physics and Chemistry of Glasses*, 46:559–563, 2005.

[109] Francis J. Norton. Permeation of gaseous oxygen through vitreous silica. *Nature*, 191, 1961.

[110] Koichi Kajihara, Taisuke Miura, Hayato Kamioka, Masahiro Hirano, Linards Skuja, and Hideo Hoson. Surface dissolution and diffusion of oxygen mole-

cules in SiO_2 glass. *Journal of the Ceramic Society of Japan*, 112:559–562, 2004.

[111] B. E. Deal and A. S. Grove. General relationship for the thermal oxidation of silicon. *Journal of Applied Physics*, 36:3770–3778, 1965.

[112] K. Tatsumura, T. Shimura, E. Mishima, K. Kawamura, D. Yamasaki, H. Yamamoto, T. Watanabe, M. Umeno, and I. Ohdomari. Reactions and diffusion of atomic and molecular oxygen in the SiO_2 network. *Physical Review B*, 72:045205, 2005.

[113] Diego Di Francesca. *Role of Dopants, Interstitial O_2 and Temperature in the Effects of Irradiation of Silica-based Optical Fibers*. PhD thesis, Université Jean Monnet de Saint-Étienne, 2015.

[114] P. Urquhart. Review of rare earth doped fibre lasers and amplifiers. *IEEE Proceedings J - Optoelectronics*, 135:385–407, 1988.

[115] Sylvain Girard, Marilena Vivona, Arnaud Laurent, Benoît Cadier, Claude Marcandella, Thierry Robin, Emmanuel Pinsard, Aziz Boukenter, and Youcef Ouerdane. Radiation hardening techniques for Er/Yb doped optical fibers and amplifiers for space application. *Optics Express*, 20:8457–8465, 2012.

[116] A. Ladaci, S. Girard, L. Mescia, T. Robin, A. Laurent, B. Cadier, M. Boutillier, Y. Ouerdane, and A. Boukenter. Optimized radiation-hardened erbium doped fiber amplifiers for long space missions. *Journal of Applied Physics*, 121:163104, 2017.

[117] Diego Di Francesca, Simonpietro Agnello, Sylvain Girard, Antonino Alessi, Claude Marcandella, Philippe Paillet, Aziz Boukenter, Franco Mario Gelardi, and Youcef Ouerdane. O_2-loading treatment of Ge-doped silica fibers : A radiation hardening process. *Journal of Lightwave Technology*, 34:2311–2316, 2016.

[118] O. Majérus, L. Cormier, D.R. Neuville, L. Galoisy, and G. Calas. The structure of SiO_2GeO_2 glasses : A spectroscopic study. *Journal of Non-Crystalline Solids*, 354:2004 – 2009, 2008.

[119] Grant S. Henderson, Daniel R. Neuville, Benjamin Cochain, and Laurent Cormier. The structure of GeO_2SiO_2 glasses and melts : A Raman spectroscopy study. *Journal of Non-Crystalline Solids*, 355:468 – 474, 2009.

[120] A. L. Tomashuk, M. Y. Salgansky, P. F. Kashaykin, V. F. Khopin, A. I. Sultangulova, K. N. Nishchev, S. E. Borisovsky, A. N. Guryanov, and E. M. Dianov. Enhanced radiation resistance of silica optical fibers fabricated in high O_2 excess conditions. *Journal of Lightwave Technology*, 32:213–219, 2014.

[121] P. Giannozzi *et al.* QUANTUM ESPRESSO : A modular and open-source software project for quantum simulations of materials. *Journal of Physics : Condensend Matter*, 21:395502, 2009.

[122] L. Martin-Samos and G. Bussi. SaX : An open source package for electronic-structure and optical-properties calculations in the GW approximation. *Computer Physics Communication*, 180:1416–1425, 2009.

[123] E.K.U. Gross, R.M. Dreizler, North Atlantic Treaty Organization. Scientific Affairs Division, NATO Advanced Study Institute on Density Functional Theory, and Organització del Tractat de l'Atlàntic Nord. Scientific Affairs Division. *Density Functional Theory.* B] : [NATO ASI series. Springer, Berlin, 1995.

[124] Kurt *et al.* Lejaeghere. Reproducibility in density functional theory calculations of solids. *Science*, 351:1415, 2016.

[125] M. C. Payne, M. P. Teter, D. C. Allan, T. A. Arias, and J. D. Joannopoulos. Iterative minimization techniques for ab initio total-energy calculations : molecular dynamics and conjugate gradients. *Reviews of Modern Physics*, 64:1045–1097, 1992.

[126] J. P. Perdew and Alex Zunger. Self-interaction correction to density-functional approximations for many-electron systems. *Physical Review B*, 23:5048–5079, 1981.

[127] N.W. Ashcroft and N.D. Mermin. *Solid State Physics.* Saunders College, Philadelphia, 1976.

[128] G. P. Francis and M. C. Payne. Finite basis set corrections to total energy pseudopotential calculations. *Journal of Physics : Condensed Matter*, 2:4395, 1990.

[129] M. van Schilfgaarde, T. Kotami, and S. Faleev. Quasiparticle self-consistent GW theory. *Physical Review Letters*, 96:226402, 2006.

[130] Trygve Helgaker, Poul Jorgensen, and Jeppe Olsen. *Molecular electronic-structure theory.* John Wiley and Sons, Chichester, 2000.

[131] Lars Hedin and Stig Lundqvist. Effects of electron-electron and electron-phonon interactions on the one-electron states of solids. volume 23 of *Solid State Physics*, pages 1 – 181. 1970.

[132] R. W. Godby and R. J. Needs. Metal-insulator transition in Kohn-Sham theory and quasiparticle theory. *Physical Review Letters*, 62:1169–1172, 1989.

[133] Daniel Sheppard, Rye Terrell, and Graeme Henkelman. Optimization methods for finding minimum energy paths. *The Journal of Chemical Physics*, 128:134106, 2008.

[134] Graeme Henkelman, Blas P. Uberuaga, and Hannes Jónsson. A climbing image nudged elastic band method for finding saddle points and minimum energy paths. *The Journal of Chemical Physics*, 113:9901–9904, 2000.

[135] William Humphrey, Andrew Dalke, and Klaus Schulten. VMD – Visual Molecular Dynamics. *Journal of Molecular Graphics*, 14:33–38, 1996.

[136] A. Kokalj. Computer graphics and graphical user interfaces as tools in simulations of matter at the atomic scale. *Computational Materials Science*, 28:155 – 168, 2003.

[137] `https://photonics.ixblue.com`.

[138] L. Martin-Samos, G. Bussi, A. Ruini, E. Molinari, and M. J. Caldas. Unraveling effects of disorder on the electronic structure of SiO_2 from first principles. *Physical Review B*, 81:081202, 2010.

[139] P. W. Anderson. Absence of diffusion in certain random lattices. *Physical Review*, 109:1492–1505, 1958.

[140] Morrel H. Cohen, H. Fritzsche, and S. R. Ovshinsky. Simple band model for amorphous semiconducting alloys. *Physical Review Letters*, 22.

[141] P. W. Anderson. Model for the electronic structure of amorphous semiconductors. *Physical Review Letters*, 34:953–955, 1975.

[142] Sir Nevill Mott. Electrons in glass. *Review of Modern Physics*, 50:203–208, 1978.

[143] David L. Griscom. Self-trapped holes in pure-silica glass : A history of their discovery and characterization and an example of their critical significance to industry. *Journal of Non-Crystalline Solids*, 352:2601 – 2617, 2006.

[144] Nicolaos D. Epiotis, James R. Larson, and Hugh H. Eaton. Common denominators by the MOVB method : The structures of H_20, H_2O_2, and their derivatives. *Croatica Chemica Acta*, 57:1031–1053, 1985.

[145] Z. A. Weinberg, G. W. Rubloff, and E. Bassous. Transmission, photoconductivity, and the experimental band gap of thermally grown SiO_2 films. *Physical Review B*, 19:3107–3117, 1979.

[146] T. Minato and D. P. Chong. Calculation of vertical ionization potentials of hydrogen peroxide by perturbation corrections to Koopmans' theorem. *Canadian Journal of Chemistry*, 61:550–552, 1983.

[147] E. Gartstein, M. Radler, T. O. Mason, and J. B. Cohen. The agglomeration of point defects in transition metal monoxides. *Materials Research Society Proceedings*, 82:65, 1986.

[148] V.V. Voronkov. Grown-in defects in silicon produced by agglomeration of vacancies and self-interstitials. *Journal of Crystal Growth*, 310:1307 – 1314, 2008.

[149] Janez Cerkovnik and Božo Plesničar. Recent advances in the chemistry of hydrogen trioxide (HOOOH). *Chemical Reviews*, 113:7930–7951, 2013.

[150] S. Kohsuke, S. Yoshihiro, and E. Yasuki. The rotational spectrum and structure of HOOOH. *Journal of the American Chemical Society*, 127:14998–14999, 2005.

[151] W. Orellana, A. J. R. Silca, and A. Fazzio. Oxidation at the Si/SiO_2 interface : Influence of the spin degree of freedom. *Physical Review Letters*, 90:016103, 2003.

[152] R. D. Suenram and F. J. Lovas. Dioxirane. its synthesis, microwave spectrum, structure, and dipole moment. *Journal of the American Chemical Society*, 100:5117–5122, 1978.

[153] Imène Reghioua. *Cathodoluminescence Characterization of Point Defects in Silica-Based Materials : Optical Fibers and Nanoparticles*. PhD thesis, Université Jean Monnet de Saint-Étienne, 2018.

[154] Dean Weldor, Tina D. Poulsen, Kurt V. Mikkelsen, and Peter R. Ogilby. Singlet sigma : The other singlet oxygen in solution. *Photochemistry and Photobiology*, 70:369–379, 1999.

[155] Camila M. Mano, Fernanda M. Prado, Júlio Massari, Graziella E. Ronsein, Glaucia R. Martinez, Sayuri Miyamoto, Jean Cadet, Helmut Sies, Marisa H. G. Medeiros, Etelvino J. H. Bechara, and Paolo Di Mascio. Excited singlet molecular O_2 (1Dg) is generated enzymatically from excited carbonyls in the dark. *Scientific Reports*, 4:5938, 2014.

[156] D. B. Min and J. M. Boff. Chemistry and reaction of singlet oxygen in foods. *Comprehensive Reviews in Food Science and Food Safety*, 1:58–72, 2002.

[157] Andrej Hovan, Shubhashis Datta, Sergei G. Kruglik, Daniel Jancura, Pavol Miskovsky, and Gregor Bánó. Phosphorescence kinetics of singlet oxygen produced by photosensitization in spherical nanoparticles. part I. theory. *The Journal of Physical Chemistry B*, 122(20):5147–5153, 2018.

[158] B F Minaev. Electronic mechanisms of activation of molecular oxygen. *Russian Chemical Reviews*, 76:1059–1083, 2007.

[159] P. V. Sushko, S. Mukhopadhyay, A. M. Stoneham, and A. L. Shluger. Oxygen vacancies in amorphous silica : structure and distribution of properties. *Microelectronic Engineering*, 80:292–295, 2005.

[160] S. Girard, J. Kuhnhenn, A. Gusarov, B. Brichard, M. Van Uffelen, Y. Ouerdane, A. Boukenter, and C. Marcandella. Radiation effects on silica-based optical fibers : Recent advances and future challenges. *IEEE Transactions on Nuclear Science*, 60:2015–2036, 2013.

[161] Andrew K. Galwey and Michael E. Brown. Application of the Arrhenius equation to solid state kinetics : Can this be justified ? *Thermochimica Acta*, 386:91 – 98, 2002.

[162] Andrew K. Galwey. Magnitudes of Arrhenius parameters for decomposition reactions of solids. *Thermochimica Acta*, 242:259 – 264, 1994.

[163] F. Messina and M. Cannas. Character of the reaction between molecular hydrogen and a silicon dangling bond in amorphous SiO_2. *The Journal of Physical Chemistry C*, 111:6663–6667, 2007.

[164] A. Alessi, S. Girard, D. Di Francesca, C. Marcandella, P. Paillet, A. Boukenter, and Y. Ouerdane. Radiation induced attenuation kinetics in pure-silica-core optical fibers during successive irradiations. In *2015 15th European Conference on Radiation and Its Effects on Components and Systems (RADECS)*, pages 1–4, 2015.

[165] A. T. Ramsey, W. Tighe, J. Bartolick, and P. D. Morgan. Radiation effects on heated optical fibers. *Review of Scientific Instruments*, 68:632–635, 1997.

[166] W. Tighe, P. Morgan, H. Adler, D. Cylinder, D. Griscom, D. Johnson, D. Palladino, and A. Ramsey. Proposed experiment to investigate use of heated optical fibers for tokamak diagnostics during DT discharges. *Review of Scientific Instruments*, 66:907–909, 1995.

[167] A. Alessi, S. Girard, M. Cannas, S. Agnello, A. Boukenter, and Y. Ouerdane. Influence of drawing conditions on the properties and radiation sensitivities of pure-silica-core optical fibers. *Journal of Lightwave Technology*, 30:1726–1732, 2012.

[168] S. Girard, Y. Ouerdane, B. Vincent, J. Baggio, K. Medjahdi, J. Bisutti, B. Brichard, A. Boukenter, A. Boudrioua, and J.-P. Meunier. Spectroscopic study of γ -ray and pulsed x-ray radiation-induced point defects in pure-silica-core optical fibers. *IEEE Transactions on Nuclear Science*, 54:1136–1142, 2007.

[169] I. Reghioua, S. Girard, M. Raine, A. Alessi, D. Di Francesca, M. Fanetti, L. Martin-Samos, N. Richard, M. Valant, A. Boukenter, and Y. Ouerdane. Cathodoluminescence characterization of point defects in optical fibers. *IEEE Transactions on Nuclear Science*, 64:2318–2324, 2017.